UNIVERSITY OF CALIFORNIA
RIVERSIDE

Directed Synthesis of Asymmetric Au/ZnS Photocatalytic Nanomaterials by M13 Bacteriophage Spheroids

A Dissertation submitted in partial satisfaction
of the requirements for the degree of

Doctor of Philosophy

in

Electrical Engineering

by

Joshua Plank

December 2019

Dissertation Committee:

Dr. Elaine D. Haberer, Chairperson
Dr. Ming Liu
Dr. Yadong Yin

The Dissertation of Joshua Plank is approved:

Committee Chairperson

University of California, Riverside

Acknowledgements

I would first like to thank my advisor Dr. Elaine D. Haberer, because without her guidance and direction I would not have gone far with this research. She gave me the opportunity to study at UCR, and showed me how to critically analyze information, and organize it in a coherent way. Most of all she taught me persistence in research and how to ask better questions when it comes to data, for my own and others.

I would like to thank Tam-Triet, for helping me get started and showing me around, but most of all for keeping things light when the work was hard. There were a lot of late nights and tough problems we worked through together, and I could always rely on Tam to help with the science. And in terms of that I would also like to thank Stephen Hsieh, because without him I would still be lost in the chemistry and nucleation details. Between Tam and Stephen, our discussions helped me through countless roadblocks, where I was missing the underlying science of the issue.

I'd also like to thank my lab mate Joe helping with all the small but essential details, and also showing me some creative solutions when it came to doing the experiments. Also, Zaira Alibay for her constant patience and help writing a good paper. She is a good colleague and friend.

From CFAMM, I would like to thank Michael Pidgeon and especially Mathias Rommelfanger, who taught me the in's and out's of working the TEM, and helped me on dozens of occasions to get good images. They also kept it from ever being boring. Dr.

Bozhilov helped make sense of a lot the microscope images, and how to do their analysis.

To Alireza, we had many fun talks on physics. To my good friend Tyler, thanks for always telling me what I needed to hear, and not just what I wanted. It kept me motivated and pushing for better things. To my parents for being there no matter what, and always having good advice. I couldn't have done it without you. And finally Jenay, who kept me grounded through everything, it kept me sane, and you always gave me a weekend to look forward to. This is dedicated to you, my friends, and family. Thank you.

ABSTRACT OF THE DISSERTATION

Directed Synthesis of Asymmetric Au/ZnS Photocatalytic Nanomaterials by M13 Bacteriophage Spheroids

by

Joshua Plank

Doctor of Philosophy, Graduate Program in Electrical Engineering
University of California, Riverside, December 2019
Dr. Elaine D. Haberer, Chairperson

Recently, the M13 bacteriophage has been developed as a versatile material template, where it has been shown to bind and grow a wide range of materials both organic and inorganic. Also, despite the discovery over 30 years ago of its ability to transform into a range of structures, far removed from its native filament, its other forms have been barely researched for their capabilities in nanostructure assembly. The M13, in all of its forms, is an asymmetric, bifunctional template, meaning it can grow two materials together, in a non-centrosymmetric fashion. Not only is this fairly unique

among virus templates, but is also extremely useful in the creation of catalytic materials. A material's catalytic properties can be augmented or enhanced when combined with other materials.

Semiconductor photocatalysts tend to be enhanced when combined with other semiconductors or metals, which help with light absorption and the charge separation necessary for catalytic reactions. The orientation and assembly of the combined materials can have significant impacts on their functionalities, where growing the materials over the surface of one another can limit their catalytic activity. For these types of particles, reactive surface area is a major contributing factor in performance. Therefore, with Janus-like, asymmetric particles, which expose equal amounts of each material, photocatalytic properties can be expected to be greatly enhanced.

In this study, we investigated the M13's spheroid form in its controlled synthesis of ZnS and then Au, and the photocatalytic activity of these materials. We showed that the spheroid transformation process required modification with the ZnS and Au binding peptides both displayed on the virus. We then demonstrated that the growth of each material was limited to their respective protein group, and could be controlled for its size. When both Au and ZnS were present on the template, the combined particle could be used in the photocatalytic degradation of multiple dyes, and the activity of which was greater than either of materials alone. Further, the addition of Au to ZnS allowed photocatalytic activity under visible light excitation, which is normally impossible for the wide bandgap semiconductor. In the development towards a more efficient photocatalyst nanostructure, hierarchical structures were then assembled, in an effort to create so-called core satellite structures of varying complexity. These structures made use of a Au nanoparticle as the core, with M13 filaments or spheroid decorating its surface, which could be used to synthesize ZnS. This research laid the groundwork for a much more efficient photocatalytic nanostructure.

Table of Contents

Figure List

Table List

Chapter 1. Introduction

1.1 Motivation

With advent of phage display in 1985 by Smith et al,[1] the number of discovered peptides capable of material-specific binding has increased exponentially. When displayed in or on a virus capsid, in combination with viruses diverse array of natural nano-scale morphologies, they become a diverse toolkit of templates for nanoparticle synthesis and molecular recognition. These viral templates can then direct synthesis of multiple materials, simultaneously offering high complexity and control in new architectures that would otherwise be difficult to achieve. Certain viruses, like the filamentous bacteriophage of the *Inoviridae* family, display the ability to undergo drastic morphology transformations,[2] meaning that a single virus could potentially create many unique structures, ranging from nanowires[3] to nanospheres.[4] This family of viruses is also somewhat unique in that their two major capsid protein groups are arranged asymmetrically along the capsid. The ability to assemble asymmetric structures shows high potential in catalytic applications. In this work, we used a virus from this family, the M13, and first looked into its shape changing ability, and how the process was affected by genetically inserted peptides. We then used its spherical form as a template for the sequential synthesis of noble metal Au and semiconductor ZnS nanoparticles in asymmetric nanostructures. Finally we showed that these materials were photocatalytically active under UV and visible light, and capable of degrading a range of aqueous contaminant molecules, thus displaying applicability of the spheroid form of the phage, which has been relatively unused.

1.2 Photocatalytic water remediation

1.2.1 Water-borne contaminants

Without doubt, industrial mass production has massively reduced the necessary work, and therefore costs, of a vast number of products, which in turn has benefitted society by making them more accessible to a greater number of people. However, large factories produce vast amounts of water-borne waste. The waste is typically separated from water via conventional treatment methods like flocculation or filtration before releasing water to the environment through sewer-ways. While most particulates are retained in the facility, aqueous, molecular-scale by-products remain in the effluent. In particular, aromatic molecules such as dyes, phenolic compounds, and antibiotic are too small to be removed by traditional waste-treatment methods and require costly secondary treatments such as ozonation or carbon adsorption.[5] Even then, these molecules end up in environmental waterways.[6] Many dyes can have a variety of mutagenic effects on organisms,[7] and if in high enough concentrations, can affect photosynthetic processes and damage aquatic environments.[8] Similarly, antibiotics entering the environment can have carcinogenic effects[9] as well as facilitate antibiotic resistance.[10] A low cost, environmentally friendly method of water remediation is required, and a solution may lie in solar-driven photocatalysis. In this process, highly reactive radicals created when the photocatalyst absorbs light, react with contaminant molecules, and break them down through reduction-oxidation reactions.

1.2.2 Semiconductor photocatalysis

Photocatalysts absorb sunlight and use the energy to accelerate chemical reactions. With many potential applications, a large body of research focuses on water remediation.[11] Most photocatalysts are aqueous based, wide-bandgap semiconductors,[12] which when excited by sufficiently high energy light, generate electron-hole pairs. If these charges do not recombine, and instead migrate to the surface of the catalyst, they will create highly charged radicals from surrounding water molecules.[13] Of the many possible radicals, the most commonly formed are hydroxyl radicals, simple $\cdot OH$ groups. These are capable of breaking molecular bonds through reduction/oxidation reactions, and thus capable of degrading many types of contaminant molecules, notably oils, dyes, and antibiotics.[14–16] However, since most semiconductor photocatalysts are wide-bandgap, and therefore only absorb UV light, they cannot utilize ~90-95% of the solar spectrum. A method of 'sensitizing' the semiconductor to visible wavelengths of light requires incorporating a metal nanoparticle into the semiconductor structure.[17] A graphical overview of semiconductor photocatalyst process is shown in Figure 1.1.[18]

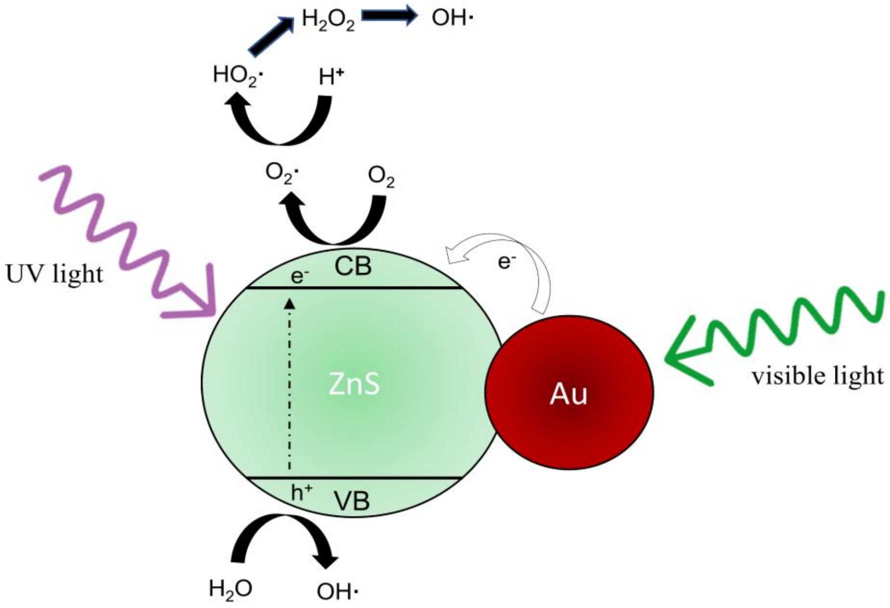

Figure 1.1 *Graphical representation of the photon-initiated series of reduction/oxidation reactions leading to hydroxyl radical formation, which are highly reactive and cause degradation of other molecules present in solution*.

1.2.3 Metal co-catalyst

In general, the role of the metal nanoparticle is many-fold. It can act as a scattering center to help increase the amount of light reaching the semiconductor (Figure 1.2a), enhance light absorption at energies that overlap with the conduction band of the semiconductor (Figure 1.2b), create an electric field in an attached semiconductor (Figure 1.2c), or even generate high energy electrons that can transfer to a neighboring semiconductor (Figure 1.2d). [19] Enhanced light absorption and the generation of high energy electrons (called hot electrons) occur as a result of localized surface plasmon resonance, a coherent oscillation of the electrons in the metal nanoparticle caused by the electric field of an incident photon. Such effects have been shown to depend on the morphology of the metal and semiconductor, and are highly enhanced in asymmetric nanoparticles.[20] Another possible role of the metal is the formation of a Schottky junction at the interface between it and the semiconductor. Given a higher work energy in the semiconductor, electrons flow from the semiconductor to the metal, leaving behind a depletion region, and creating a small electric field in the semiconductor near the interface.[21] This field serves to help separate photogenerated electron-hole pairs, increasing recombination lifetimes, and thereby increasing the likelihood of migrating to the surface.[12] For the plasmonic metal to act as a source of electrons, the resonant electrons must have higher energy than the Schottky barrier. With the correct momentum, they can inject directly into the conduction band states of the semiconductor.

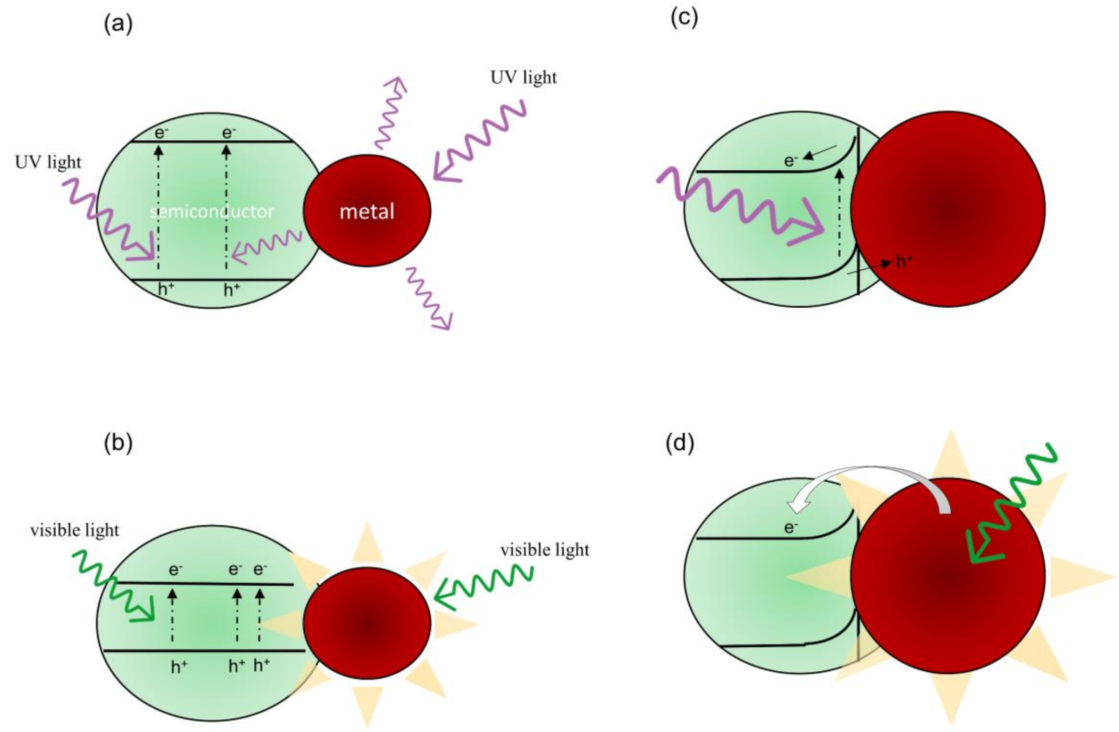

Figure 1.2 *(a) The metal nanoparticle can act as a scattering center, increasing the excitation energy photons reaching the semiconductor particle. (b) Strong electromagnetic field enhancement increases excitation of electron-hole pairs near the interface of the metal and semiconductor particle, but only occurs for areas of energy overlap in each particle. (c) Correct conditions will form a Schottky barrier at the semiconductor-metal interface. Photoexcited charges in the depletion region will be separated by the created electric field. (d) Energetic plasmonic hot electrons can overcome the Schottky barrier and inject directly into the conduction band of the semiconductor.*

1.3 M13 bacteriophage

1.3.1 Phage structure

The M13 belongs to the *Inoviridae* family, all of which are filamentous and non-lytic bacteriophage. Its host is the bacterium *E. coli*. It has a single stranded loop of DNA, containing 6400 base pairs that code for 11 proteins, 5 of which are capsid proteins. The majority of the filament is made up of 2700 copies of p8 protein, arranged helically with five-fold symmetry, around the DNA packaged inside. One end of the filament is capped by 5 p7 and 5 p9 proteins, and the other end is capped by 5 p6 and 5 p3 proteins. A graphical representation of the virus is shown in Figure 1.3.

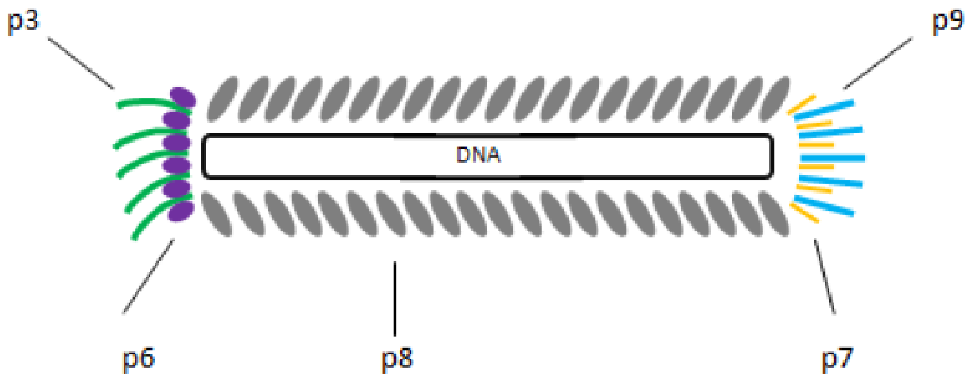

Figure 1.3 *Basic arrangement of M13 capsid proteins around ssDNA packaged inside.*

The p8 major coat protein and p3 minor coat protein have been most frequently used as peptide insertion locations.[22] The p8 proteins are each 50 amino acids long, with alpha-helical secondary structure. They are arranged such that the positive C-termini interact with the inner DNA, the negative N-termini face the environment, and a non-polar region lies in the middle. The p8 are held together via pi-stacking interactions between buried tryptophan and phenylalanine residues within in the non-polar regions. The light absorption and emission properties of these aromatic residues are highly sensitive to environmental changes. A chimera protein drawing is shown in Figure 1.4(a) and their arrangement is shown in 1.4(b). The much larger p3 protein contains 215 amino acids and contains 3 sections. The N-terminal and middle sections interact with the host and initiate infection, while the C-terminal section interacts mostly with the p6. The C-terminal, non-polar regions of the p3 proteins associate with non-polar regions of the p8 proteins via the five buried p6 proteins.[23] To accommodate this interaction, the assembly of the terminal p8 proteins differs slightly from the rest of the capsid.[24] The phage dimensions measure about 880 nm in length and 6 nm in width.

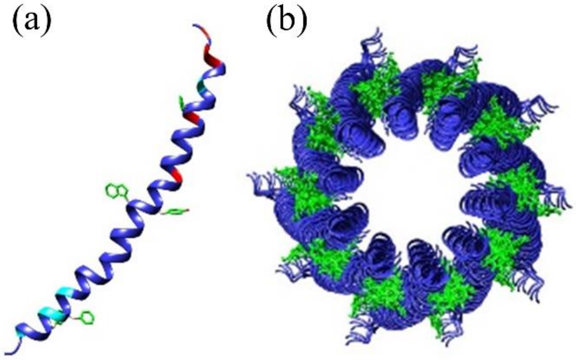

Figure 1.4 *(a) Chimera drawing of p8 protein. Highlighted in green are the two major aromatic amino acids, tryptophan and phenylalanine. (b) View of helical protein arrangement as observed down axis.*

1.3.2 Genetic modification

A large number of material-specific binding peptides have been discovered to date, mostly found through biopanning techniques. To confer specificity for material synthesis or binding to the virus, novel peptides are typically added to the N-termini of the p3 and/or the p8 proteins. This is done by inserting the peptide-coding sequence of double stranded DNA into the proper location of the phage genome. In order to do this, the phage genome must first be made double stranded, which occurs after infection and insertion of single-stranded DNA into the host cytoplasm, by the host enzymes. The bacteria is then lysed and the double stranded viral DNA purified. Location specific restriction enzymes are then used to make cuts in the viral DNA, and the new peptide-coding DNA sequence is ligated into the cut. The new virus genome is then inserted back into the host via electroporation and the natural replication cycle resumes.

There are different restrictions on the allowed size of the peptide in the p3 and p8 proteins. This is largely due to the degree by which the replication cycle is affected. In general, larger peptides are tolerated in the p3, up to about 30 amino acids,[25] and up to 8 amino acids in the p8.[22] However, these numbers can be lower if many of the amino acids of the inserted peptide are too highly charged. For example, in the p8, up to 3 glutamic acid residues can be tolerated, but adding 4 is thought to make the protein too highly charged to package properly at the end of the replication cycle.

1.3.3 Morphological transformation

One of the most notable qualities of the M13 and other Ff class[26] bacteriophage their ability to go through dramatic conformational shifts. This change is unique in that most viruses are relatively fixed in their morphologies. While there are some exceptions, such as the Tobacco Mosaic Virus[27] and Potato Virus X[28], none go through the massive change in aspect ratio as seen with M13. First shown by Griffith et al.[2] in 1981, it was thought to be a part of the infection process following p3 interaction with host *E. coli*, which pulls the virus into contact with its membrane and leads to insertion of viral DNA.[29] The experiments were done by mixing chloroform, an organic solvent, with a solution of aqueous based phage, where the chloroform-water interface was thought to mimic the host membrane.[2] This process led to the formation of small spheroids that were 10's of nanometers in size. The 880 nm long filament contracts into a 50 nm spheroid through a telescoping effect with the p8 proteins sliding past one another. If the temperature is lowered during the process, an intermediate form (termed i-form) is observed,[29] a rod that measures about 150 nm in length and 20 nm in width, it was then found that at least up until this point, the p3 and p8 capsid proteins and their relative arrangements were retained.[30] Example electron micrographs of the three virus forms are shown in Figure 1.5. During this process, about two-thirds of the viral DNA is extruded from a pore located at the p3 tip of the virus.[2] It has been shown that genetic modifications can affect this process, with some encouraging the transformation[31] and some stopping it altogether.[32] The spheroid and i-form preserve the asymmetric orientation of the p3 and p8 from the filament.

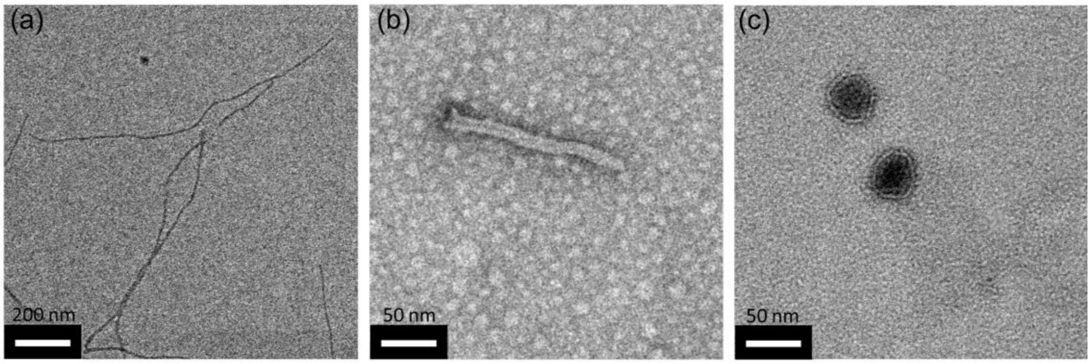

***Figure 1.5** (a) Transmission electron micrograph of (a) filamentous, (b) intermediate, and (c) spheroidal form of the M13 bacteriophage.*

1.3.4 Directed material synthesis and binding

The arrangement of M13 bacteriophage structural proteins within its capsid creates a promising, readily modifiable template for non-centrosymmetric nanomaterials. Some notable examples using both proteins in unique functions include work by Avery et al.[33] in which the p3/p8 were used to synthesize Fe_3O_4/Rh, and work by Huang et al.[34] in which the p3/p8 were used to bind CdSe/Au nanoparticles. There are also various examples in which two different peptides were displayed on the p8, in mosaic type patterns, such as work by Nam et al.[35] or Mao et al.[36] which enable patchwork synthesis of two dissimilar materials along the filament. Examples among other viral templates such as TMV[37] or P22[38] display bi-functionality, but each are centrosymmetric due to their native structures.

1.4 ZnS and Au

The two materials used in this work were ZnS and Au. ZnS is a wide bandgap semiconductor, and Au is a noble metal. The ZnS bandgap depends on its crystal structure, of which it has two possibilities, zinc-blende or wurtzite, while Au is face-centered cubic. Bulk ZnS has a bandgap as small as 3.67 eV, but particles near the Bohr radius have displayed bandgaps as large as 4.9 eV.[39] Both materials have many applications but ZnS in particular is known for photocatalytic activity,[40,41] due to its conduction/valence band positions, and Au is a well known catalyst material due to its resistance to reduction or oxidation.[42] These conduction and valence band positions dictate the electron and hole energies, respectively, leading to high reduction/oxidation energies.

1.4.1 Background in photocatalysis

The two materials used in this work have been used in various photocatalytic applications. Despite its rather large bandgap, ZnS is an extremely attractive material for photocatalysis. It is an abundant, non-toxic material, and shows high resistance to oxidative corrosion.[43] It is also direct bandgap, meaning no phonon is required to bring an electron to the conduction band, as is the case for the main photocatalysis research workhorse, TiO_2. This alone increases its photoefficiency many-fold since single photons can directly excite electron-hole pairs. As mentioned previously, the positions of its conduction and valence bands are ideal for photocatalysis. The holes in the valence band have high oxidative potential, and electrons in the conduction band have high reduction potential, evidence of which is best seen with examples where ZnS was used in the production of H_2 from H_2O[44] or CH_4 from CO_2.[45] Another consequence is that sacrificial electron or hole donors are not required during photocatalysis, a typical drawback for many materials such as CdS or TiO_2, which can only drive one of the half reactions in the above reactions.

Under UV illumination, ZnS rapidly produces electron-hole pairs, which also due to the positions of the levels, have high recombination lifetimes.[46] Many efforts have been made to increase its visible light activity, usually focused on doping with transition-metal ions,[47,48] but some success has also been found by engineering S-vacancy states.[49] More recently, more research has gone into ZnS heterostructures, where another semiconductor like ZnO[50] or noble metal like Au[51] or Ag[52] are grown or bound to the ZnS surface, then subsequently applying the hybrid material in photocatalysis. Au on the other hand, does not show much photocatalytic capability on its own, so is typically paired with a semiconductor as a co-catalyst, in order to increase its activity. As a corrosion-resistant noble metal, yet also a transition metal, it is known to be an efficient catalyst material none-the-less.[53] In any case, the photocatalytic activity of the two materials together is greater than either alone. In multiple reports, small (~5 nm) Au nanoparticles (AuNP) are combined with much larger ZnS particles. Work by Chen et al. showed that these Au/ZnS particles could quickly degrade thionine dye, and that they greatly outperformed Au/TiO_2 nanoparticles.[54] Other worked has used these to degrade many dyes,[51,55] split water for H_2 production,[44] and oxidize CO.[52] The work by Choi et al.[52] showed that the photocatalytic activity was dependent on the crystal structure of the ZnS, where hexagonal ZnS outperformed cubic ZnS when paired with Au.

1.4.2 Material interface- Schottky or Ohmic?

When ZnS and Au are brought into contact, theoretical Schottky barrier calculations indicate that when Fermi level equilibrium is established, electron energy levels are higher in ZnS, and therefore will flow into Au, creating an Ohmic junction.[21] This is calculated by the difference in work function energies, which help dictate the Fermi energy at the interface. An Ohmic junction does not create the electric field that would normally help in separating photo-generated electron-hole pairs, so is considered resistive. However, ZnS has been shown experimentally to have a substantially high concentration of surface states, on the order of 10^{16} states/cm^3,[56] which introduce many mid-gap energy levels that effectively ‘pin’ the Fermi energy at the surface. This serves to create a Schottky barrier at the Au/ZnS interface with an energy barrier height entirely dependent on the difference of bandgap and surface state energies. I-V measurements of Au/ZnS junctions have measured a Schottky barrier as high as 2.2 eV.[57] Photocurrent measurements of Au/ZnS core-shell particles showed that Au was necessary to produce current, which is likely only possible by plasmon-induced hot electron injection, but no further effort in this work was done to quantify the Schottky barrier.[51] Unfortunately, the Schottky barrier is often quickly attributed to increased photocatalytic activity between Au and ZnS in the literature, without any further analysis of the heterojunction. In any event, whether the underlying mechanism is fully understood or not, Au/ZnS heteroparticles display enhanced photocatalytic capabilities over the individual consituentseither of their components alone. It should be noted that much smaller barrier heights are expected for nano-scale particles, such as those in this work, where it has been shown that the rate of tunneling processes become higher, which effectively reduces the energy barrier.[58]

1.5 Scope of Work

In this work, we genetically insert a ZnS-binding peptide into the p3 of a phage with a Au-binding peptide already on its p8 protein. During development of the process for shape change conversion, significant changes to secondary structure and spheroid morphology were observed when compared to spheroids prepared with only the Au-binding insert. This required development of a slightly modified transformation procedure. Next, the dually-modified spheroids were used to synthesize ZnS and Au in an asymmetric orientation. To optimize the materials for photocatalytic applications, the processes for ZnS and Au growth were developed in an effort to produce larger particles.

This was essential, since photocatalytic efficiency is heavily dependent on material surface area. Once accomplished, the new ZnS/Au particles were used to photocatalytically degrade dyes in solution. To increase the amount of ZnS, the main catalytic component, the p8 protein was instead explored as a site for directed synthesis. In this case and the p3 was used to bind Au. This required slight modifications to the synthesis procedures but would potentially provide improved photocatalytic capabilities. Finite difference time domain simulations predicted that the ZnS-bound AuNP's would have size-proportional electric field penetration depths into ZnS, indicating that larger particles may have benefits to visible light driven photocatalysis.

In Chapter 2, the process and results of inserting the ZnS-binding peptide into the p3 protein are discussed in terms of the genetic modification. The spheroid conversion process of this doubly modified phage is compared to the singly modified Au-binding phage and the WT, and the differences in secondary structures of the spheroids are discussed. A low temperature process is developed for the Au/ZnS-binding phage, which decreased the spheroid solution polydispersity and rate of agglomeration. These more time-stable spheroids were able to synthesize ZnS nanoparticles on their p3 proteins, and AuNP on their p8 proteins in an asymmetric manner, which is beneficial to photocatalytic applications. These materials were characterized for their crystal structure, elemental composition, and morphology.

In Chapter 3, the development of the ZnS and Au synthesis procedures to produce larger particles is shown. The particles originally grown were too small to be useful in catalytic applications. The new materials were characterized for optical absorption/emission, crystal structure, and morphology, and it was found that while the particle sizes increased, the mix of crystal structures occurred as it did with the smaller particles. The Au/ZnS particles were washed then used for the photocatalytic degradation of methylene blue (MB) and erioglaucine (EG) dyes under ultraviolet (UV) and visible wavelengths of light. EG was used to control for the dye-sensitization reaction.

In the next chapter, a different virus was used to direct synthesis of ZnS and Au. A reduction method was used to access the Cysteine amino acids in the p3 in order to bind Au nanoparticles. An assay was used to calculate the number of available Sulfur bonds. With reduced p3's, the number of bound phage to each Au nanoparticle could be controlled by the concentration of bovine serum albumin as a capping agent. This allowed the contruction of hierarchical structures of increasing complexity. Then the p8 was targeted for ZnS synthesis. The peptide in the p8 of this phage contained 3 glutamate residues, termed E3, which electrostatically bind to metal ions in solution. The material synthesized with this phage was characterized for its morphology and light absorption, and is expected to perform as an effective photocatalyst.

In this dissertation, we demonstrated that the asymmetric layout of the protein groups of the M13 bacteriophage spheroid could assemble Janus-like hetero-particles made up of two different materials. We then used the combined properties of ZnS and Au in UV and visible light photocatalysis, which would not be possible with either material alone, which was applied in the degradation of various aqueous contaminants. Future work could be done on characterizing changes in charge lifetime when Au is in contact with

ZnS, as well as on work with hydrogen generation without a sacrificial electron or hole donor.

Chapter 2. Bi-functional phage: peptide insertion, spheroid transformation, and directed material synthesis

2.1 Introduction

Asymmetric, dual-component nanoparticles have recently gained attention in fields ranging from biomedical[59] to solar energy[60] due to their intrinsic bifunctionality and directionality.[61] These types of hetero-nanoparticles typically consist of two dissimilar materials displayed on opposing surface regions.[4, 5] This architecture has the distinct advantage of spatially separating different surface functionalities,[64–66] enabling novel or enhanced performance via dissimilar yet synergistic material properties,[67–69] and generating nontrivial building blocks for self-assembly of complex nanostructures.[70–74]

While a number of methods for manufacturing two-sided or “Janus”-like particles have been explored,[75–78] process complexity and scalability challenges remain. For these, Nature may pose a solution. Biomolecules such as proteins and lipids possess both asymmetric functionality and unparalleled specificity.[79–81] When assembled into viral capsids, these bio-components become powerful, monodisperse scaffolds for nanomaterials.[82–84] Specifically, bacteriophage and plant viruses, which are compatible with rapid, large-scale production, have been the focus of much research.[37,85–92] Yet, asymmetric, dual-component nanoparticle assembly has been largely overlooked.

This is mostly due to the fact that the majority of viruses, including the ones mainly used in material templating, lack any natural asymmetry. This is likely linked to the self-assembly approach to virus formation. When the subunits are identical, the lowest energy configuration tends to produces a centrosymmetric icosahedron.[93] With the notable exception of the rod-like Tobacco Mosaic Virus, most, like the Cowpea Mosaic Virus, P22 bacteriophage, or pathogenic Adenovirus, are all icosahedral. The unique structure of the filamentous bacteriophage, including the M13, likely arises from its unique mode of assembly. Not only is the process non-lytic, it seems to require DNA as well as the cytoplasmic membrane of its host.[94] Once the DNA has been ‘packaged’, the filament is capped with a different set of capsid proteins, which separate the virus from the membrane, yet also provides the basis for asymmetric, dissimilar material synthesis. As discussed in Chapter 1, this asymmetry has been shown to be preserved during transformation to its spheroid form, but previous research has only implemented the p8 coat proteins for synthesis after transformation.

Despite its potential as a template for asymmetric Janus-like nanoparticles, the bacteriophage spheroid was never explored as a material template. This chapter examines the conversion of wild-type, Au(p8)-binding, and Au/ZnS (p8/p3)-binding M13 filaments into spheroids, then uses the unique asymmetric structural protein arrangement within the bifunctional viral scaffold to direct synthesis of metal/semiconductor non-centrosymmetric hybrid nanomaterials. The genetic modification process is briefly summarized. A series of vortex/rest cycles in the presence of chloroform was used to alter the geometry of the phage. A schematic of this process is shown in Figure 2.3a. Particular attention was given to the effect of the p3 peptide fusion and temperature on transformation. The chloroform-initiated transformation process was characterized via circular dichroism, fluorescence spectroscopy, and transmission electron microscopy. Surprisingly, the ZnS-binding peptide fusion strongly influenced the transformation process. Earlier reports employing the ZnS-binding peptide looked only at the filamentous form of the M13. The motif caused Au/ZnS-binding spheroids to be larger in size, display a greater loss of molar ellipticity, and experience more quenching of intrinsic fluorescence than Au-binding spheroids used in previous work without a ZnS-binding peptide. A size and helicity comparison was made to these earlier results which used only the Au-binding spheroid with a p8 modification. A comparison of Au/ZnS-binding phage transformed at room temperature and those initially interacted with chloroform at 0°C revealed that the low temperature process produced monodisperse spheroids that were less susceptible to agglomeration over time. These robust, bifunctional spheroidal templates were used in the site-specific growth of hybrid metal/semiconductor nanostructures, via sequential synthesis of ZnS on p3 and Au on p8, and a schematic is shown of this process in Figure 2.3b. The retained functionality of both minor and major coat fusion peptides for materials synthesis is noteworthy, as this is the first successful application using the p3 of the spheroidal form. The unique, asymmetric placement of the p3 and p8 proteins within the M13 spheroid presents a rare opportunity for viral-templated production of hybrid, non-centrosymmetric assemblies. Such nanostructures have potential to critically enhance performance in a range of sensing, catalysis, in-vivo imaging, and drug delivery applications.[61,95]

2.2 Experimental

2.2.1 ZnS-binding peptide insertion in p3 protein

A looped, 9-mer, Cysteine-restricted peptide, of sequence CNNPMHQNC, was chosen from the literature that was shown to bind and synthesize ZnS nanoparticles.[36] Following a New England Biolabs protocol, EagI and Acc65I restriction enzymes were chosen for p3 N-terminal digestion sites. The peptide sequence, along with a -GGGS linker for increased flexibility, was back-translated to DNA that was then purchased from Integrated DNA Technologies in a single stranded state. Once received, the DNA was first converted to its double stranded form with DNA polymerase, then digested with EagI and Acc65I to produce 'hanging ends'. The DNA sequence was purified by running through a polyacrylamide gel for separation, stained with ethidium bromide, and cut out and separated from the gel with the QIAGEN purification kit. Simultaneously, phage dsDNA vector was prepared. M13 DNA already containing a Au-binding insert in the N-terminal region of its p8 protein was used for the following process. First, *E. coli* was infected with phage for 15 minutes, then mixed with chloramphenicol to arrest the assembly process. This led to build up of circular phage dsDNA within the host by preventing phage protein pV from accumulating and converting dsDNA to ssDNA for packaging. *E. coli* was then lysed, phage dsDNA removed, then digested with restriction enzymes to produce identical ‘hanging ends’ as with new sequence. The vector was then purified by running through agarose gel and separating from uncut DNA and removed ends. The ZnS-binding coding sequence was then ligated into the vector dsDNA with DNA ligase, and finally electroporated into electrocompetent E. coli by quickly shocking solutions at 1.8 kV for 2-4 ms. Solutions were then amplified and counted through titer plates. Recombinant plaques were picked and checked for presence of new ZnS-binding peptide, and retained Au-binding peptide, through DNA sequencing.

2.2.2 Spheroid transformation

A method based off the originally published procedure was used to transform phage. Filamentous M13 phage were converted to spheroids using a modified chloroform treatment process.[40, 41, 44] Phage solutions were suspended in 100 μL of tris-buffered saline (TBS, 50 mM Tris–HCl, 150 mM NaCl, pH 7.5) at a concentration of 10^8 pfu/μL to which an equal volume of amylene-stabilized chloroform (99.8%, ACROS Organics) was added. The mixture was vortexed at room temperature at high power for one vortex/rest (2 s/13 s) cycle followed by up to seven additional vortex/rest cycles at low power. After mixing, approximately 85 μL of chloroform was withdrawn with a pipette. The remaining chloroform was removed by gently flowing air over the sample. Phage solutions were immediately cooled at 4°C and prepared for subsequent characterization. To elucidate the effect of transformation temperature on Au/ZnS-binding spheroids, some transformations were performed in which the first three vortex/rest cycles were held at 0°C. This approach, adapted from previous reports,[41] was intended to yield i-forms which were converted to spheroids in subsequent cycles. Equal volumes (100 μL) of filamentous M13 phage and chloroform were chilled at 0°C for 20 s, combined, then vortexed at 0°C. Following the third vortex/rest cycle, samples were quickly warmed in a 37°C water bath for 20 s. Additional vortex/rest cycles were completed at room temperature. Hereafter, this transformation procedure will be described as low temperature (LT). To assess spheroid stability against agglomeration, templates formed using 5 cycles vortex/rest cycles were stored at 4°C in TBS buffer. Stability was evaluated by measuring the areal density of spheroids and agglomerates with transmission electron microscopy (TEM) as a function of storage time. Measurements were taken on three independent samples and averaged. To elucidate the effect of the new p3 peptide on the spheroid transformation process, the room temperature transformation (RT) was compared to the Au-binding phage without the p3 insert, and a wild type phage (WT) with no modifications.

2.2.3 Circular dichroism and fluorescence measurements

Changes in the secondary structure of the p8 protein were monitored after each vortex/rest cycle from 0 to 8 using a circular dichroism (CD) spectrometer (Jasco J-815). Room temperature CD scans were taken from 200-250 nm with the following parameters: 50 nm/min scan speed, 1 nm band width, 4 s response time, and 12 scan accumulation. Measurements were taken on three independent samples and averaged.

Cycle-by-cycle analysis of changes in the local tryptophan environment was completed with a spectrofluorometer (Quanta Master 400). Room temperature fluorescence scans were taken from 270-400 nm with the following parameters: 5 nm slit widths, 1 s integration time, 1 nm step size, and 255 nm excitation source. Measurements were taken on three independent samples and averaged.

2.2.4 Material synthesis

Using adapted versions of previously reported procedures, ZnS[85] and Au[34] were synthesized sequentially on spheroidal Au/ZnS-binding phage. S-form templates were produced using the LT chloroform treatment procedure and 5 vortex/rest cycles. The p3 minor coat protein was targeted for ZnS synthesis. A 10 μM solution of zinc chloride ($ZnCl_2$, Sigma Aldrich) was prepared with viral templates at a concentration of 10^8 pfu/μL in TBS. The solution was stored at 4°C for 3 h, then an equal volume of 10 μM sodium sulfide (Na_2S, Sigma Aldrich) was added dropwise in 10 μL volumes at room temperature over the course of an hour. The entire solution was incubated at room temperature for an additional 6 h. Residual ZnS precursors were removed via centrifugal filtration (Amicon Ultra-0.5, 3 kDa) and synthesis products were resuspended in TBS. The p8 major coat protein was targeted for Au synthesis. A 100 μL volume of 5×10^7 pfu/μL phage was mixed with sodium borohydride ($NaBH_4$, Sigma Aldrich) to achieve a 1 μM solution. Subsequently, 2.5 μL of chloroauric acid ($HAuCl_4$, Sigma Aldrich) was added for a final concentration of 150 μM. Reducing agent was added first to mitigate undesirable interactions between $HAuCl_4$ and ZnS. Samples were immediately prepared for TEM and spectroscopic measurements. For comparison, Au/ZnS-binding filaments and wild-type viral templates (without ZnS- and Au-binding peptide inserts) were also used for ZnS and Au synthesis.

2.2.5 Material morphology, size, and crystal structure characterization, zeta potential, and dynamic light scattering

Transmission electron microscopy (TEM, Tecnai T12 or S/TEM Titan Themis 300) was used to study viral template geometry and size, as well as the morphology, size, site-specific growth, and overall viral template coverage of ZnS and Au synthesis products. Electron diffraction (ED) and high resolution TEM (HRTEM) were used to determine the crystal structure of the synthesized materials. Elemental analysis of the synthesis products was completed using energy dispersive spectroscopy (EDS).

To prepare TEM samples for imaging and diffraction, a 5 μL volume of solution was added to a formvar/carbon-coated copper grid (Ted Pella, Inc), incubated 5 minutes, and washed twice with deionized water. Viral template samples without ZnS or Au were stained with 2% uranyl acetate for 30 s, then wicked dry. To concentrate synthesis products and remove precursors, ED and EDS samples were pelleted three times at 14,000 rpm for 15 min and resuspended in deionized water, then 20 µL of concentrated product was dropcasted onto a SiN grid (Electron Microscopy Sciences).

Image processing and analysis were completed with ImageJ software. A minimum magnification of 11,000x was used to determine template size and differentiate among templates (spheroids, i-forms, and filaments). An ellipse was fit to each template to compute spheroid size, and major and minor axes were measured and averaged. The long and short axes of i-forms and filaments were measured directly. Template aspect ratio was used to distinguish spheroids (< 3), intermediate forms (3 - 25), and filaments (> 25). Low aspect ratio particles (< 3) larger than 150 nm were classified as agglomerates. Areal densities of viral templates were evaluated in 10 randomly selected grid locations for three different samples and averaged. The size of ZnS and Au synthesis products was determined by averaging long and short particle axes. The particle sizes were correlated with Brus equation prediction for quantum confinement effects.

Zeta potential and dynamic light scattering (DLS) measurements were taken with a Zetasizer ZS90. For each analysis, three measurements were taken of three samples, with 25 scans each, then averaged. Zeta potential measurements were done in Malvern 1070 folded capillary cells, and DLS measurements were done indisposable UV-transparent microvolume cuvettes (Sarstedt, Fisher Scientific).

2.3 Results and Discussion

2.3.1 Genetic modification for Au/ZnS-binding phage

2.3.1.1 ZnS-binding coding sequence and vector purification

Using polyacrylamide gel electrophoresis, the digested sequence coding for the ZnS-binding peptide was purified from undigested and cut ends of DNA. In this process, a voltage is applied to the gel, which moves the charged DNA down ‘lanes’ corresponding to a respective well. The smaller the DNA oligonucleotide, the less drag it experiences in the gel matrix, and the further it will travel down the gel. A ladder is used for reference to measure the length of the resulting separated DNA fragments. The results of polyacrylamide gel electrophoresis can be seen in Figure 2.1a. Reading from left to right, lane number five contains the undigested DNA oligonucleotide used as a control, and lane ten contains the low molecular weight ladder, the corresponding values of which are shown in 2.1b. All other lanes contain the DNA that has been digested by both EagI and Acc65I enzymes. In each of these lanes, there are four visible bands. The uppermost band corresponds to the undigested DNA, near the 75 base pair (bp) mark. The next band down contains the single digested DNA, near 60 bp, of which there are actually two overlapping fragments with lengths too similar to distinguish. The third band down has been digested by both enzymes, corresponds to ~55 bp, and was removed for purification. The fourth band down contains the small end fragments that have been cut from the original oligonucleotide.

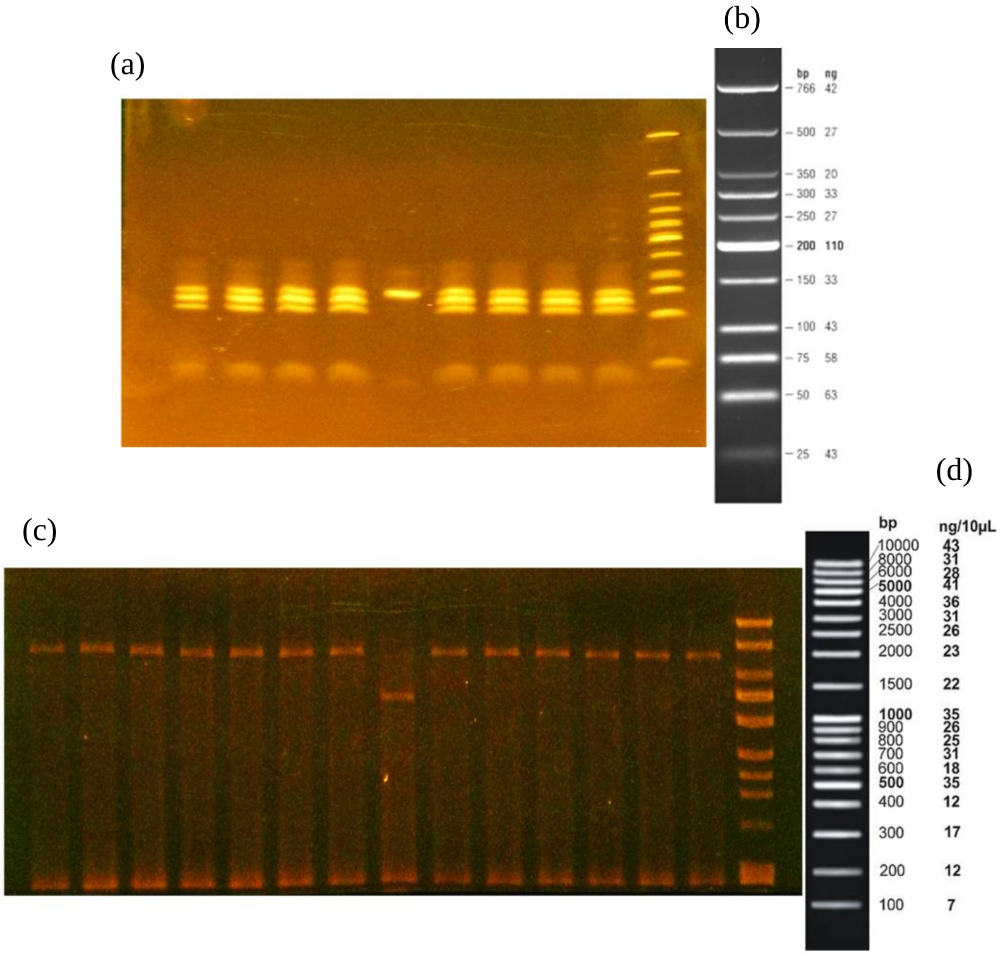

Figure 2.1 *(a) Polyacrylamide gel electrophoresis shows successful digestion of ZnS oligonucleotide with (b) associated ladder. (c) Agarose gel electrophoresis shows successful digestion of Au-binding phage recombinant form DNA with (d) associated ladder.*

After isolating the phage circular dsDNA from E. coli, it was digested with the same enzymes and also purified through gel electrophoresis. However, this complete phage DNA, called recombinant form DNA (RF DNA), was 7237 bp in length, so required agarose gel electrophoresis, which is more capable of dealing with larger DNA fragments. The results of the electrophoresis are shown in Figure 2.1c, with the ladder values shown in Figure 2.1d. Reading from left to right, lane number eight contains the control, the undigested RFDNA, and lane fifteen contains the ladder. All other lanes contain digested RFDNA. In this case, undigested RFDNA is in a highly compact, 'supercoiled' form, and moves much more quickly than the digested RFDNA, which becomes unwound and experiences high drag while migrating through the gel matrix. For this reason, undigested RFDNA appears as a 5 kbp fragment and digested DNA appears as a ~7.5 kbp fragment in reference to the DNA. This fragment was collected for ligation.

2.3.1.2 Ligation, electroporation, and DNA sequencing

The digested and purified oligonucleotide encoding the ZnS-binding peptide and M13 RFDNA were mixed and ligated together, which makes the complete strand again circular, and still dsDNA. This ligated DNA was then mixed with electrocompetent *E. coli*, shocked, and then amplified. A negative control containing non-ligated DNA and a positive control containing undigested WT DNA were also electroporated. Since non-ligated DNA is still cut, it can't be translated, and therefore shouldn't be amplified. Efficiency of this electroporation process was calculated by counting the number of plaque forming units (pfu) on each titer plate and dividing by the mass of DNA that was used in electroporation. This is shown in Figure 2.2. No plaques were observed for the non-ligated RFDNA, which indicated that this DNA was fully digested and not able to be translated within the host. Both the ligated RFDNA and WT DNA showed plaques, however, the efficiency was much lower for the new recombinant DNA, which indicated that the process could be improved. This is due to many factors, but likely arises from the high difference in digestion rates between the two restriction enzymes, non-ideal ligation conditions, and lower amplification rate of phage with two genetic modifications.

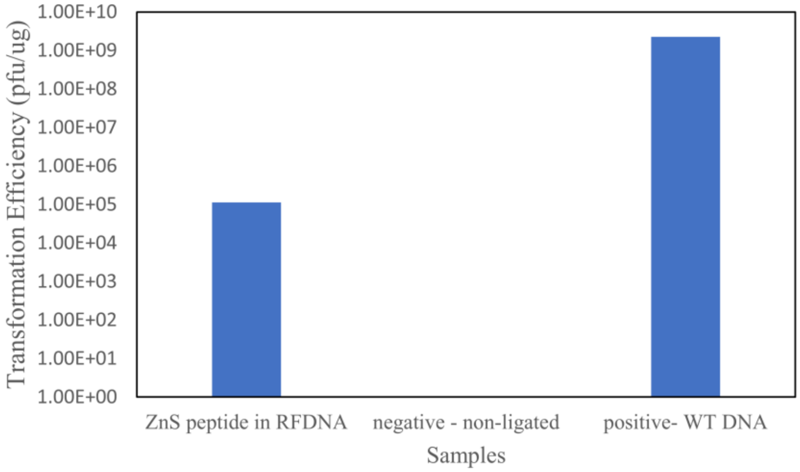

Figure 2.2 *Electroporation transformation efficiency of newly ligated Au/ZnS RFDNA compared to controls.*

2.3.2 Effects of peptide inserts on transformation

2.3.2.1 Morphology

An overview of the simple, chloroform-based process used to transform bifunctional M13 filaments into spheroidal templates for non-centrosymmetric, inorganic nanostructures is shown in Figure 2.3a. The geometric change of the Au/ZnS-binding phage was initially examined at room temperature using electron microscopy, CD, and intrinsic fluorescence. To evaluate the effect of the p3 peptide insert on bifunctional template conversion, these data were compared to those of an Au-binding phage without a minor coat protein fusion.

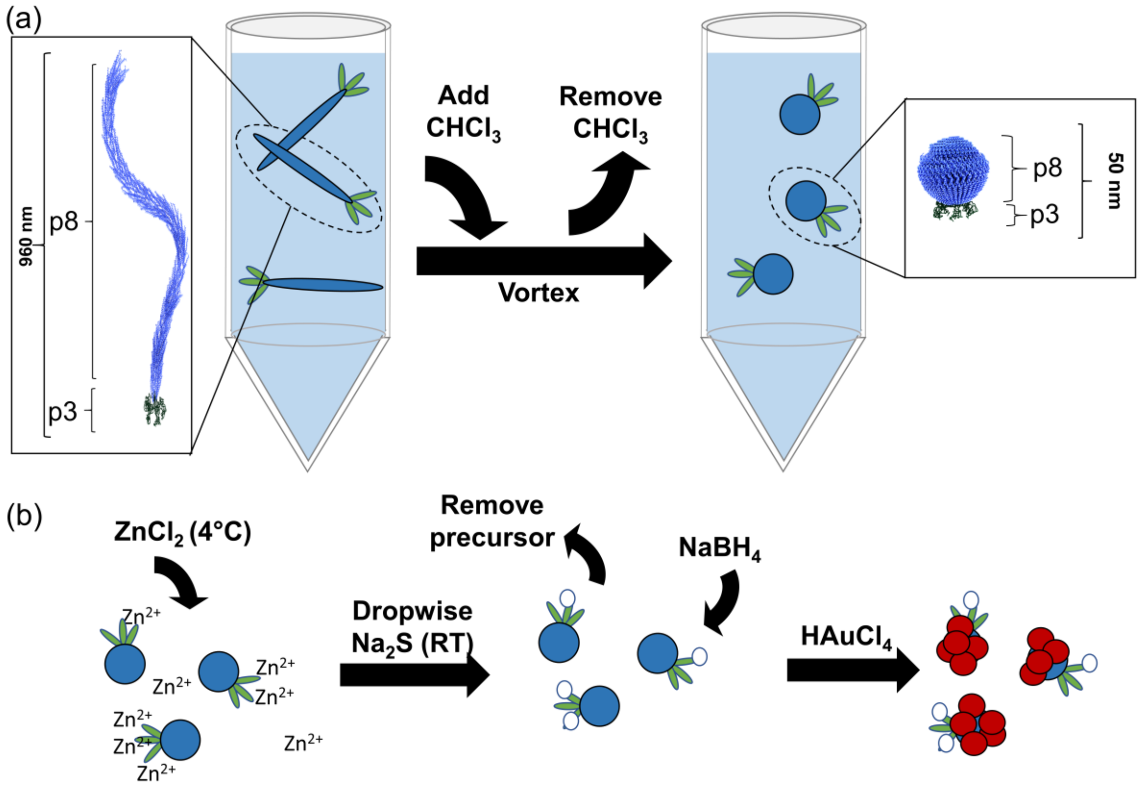

Figure 2.3 *Scheme for synthesis of hybrid non-centrosymmetric nanoparticles using bifunctional bacteriophage nanospheroids. (a) Shape transformation of M13 bacteriophage. To convert the filamentous viruses to spheroids, solutions were mixed with chloroform and briefly, but repeatedly vortexed, pausing between cycles. During this process, the nearly micron long filamentous capsid gradually contracted into a spheroid 10's of nanometers in size. The positional asymmetry of the p3 minor and p8 major coat proteins found within the filamentous form was preserved within the spheroidal form. As a result, these proteins were employed in directed synthesis of non-centrosymmetric nanomaterials. (b) To synthesize Au/ZnS nanostructures, ZnCl2 was incubated at 4°C with bifunctional Au/ZnS-binding spheroids to bind Zn ions, and then Na2S was added dropwise at room temperature (RT). After an additional incubation step, ZnS nanoparticles were formed on the p3, and remaining precursors were removed via centrifuge filtration. Subsequently, to form Au nanoparticles on the p8, NaBH4 was then added, followed by HAuCl4.*

The morphology of the Au/ZnS-binding phage was analyzed after each vortex/rest cycle. Representative TEM images depicting changes in template morphology and corresponding viral template areal densities are shown in Figure 2.4 and Figure 2.5, respectively. Initially, the transformation proceeded inhomogeneously, producing a mixture of filaments, intermediate forms (i-forms), and spheroids (s-forms). With each vortex/rest cycle, the number of filaments and i-forms decreased as the number of spheroids increased.

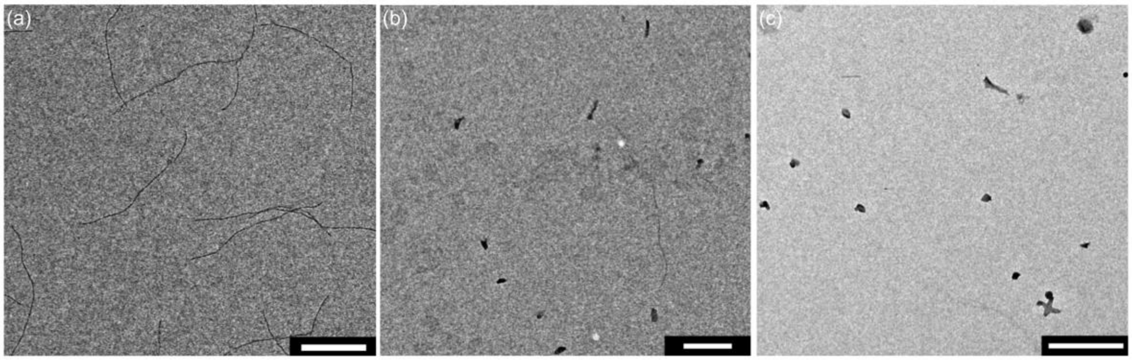

Figure 2.4. *Low magnification transmission electron microscopy (TEM) images of Au/ZnS-binding phage after (a) 0 cycles, (b) 3 cycles, and (c) 5 cycles of room temperature chloroform treatment. The distribution of template geometries is shown for each condition. Samples were stained with 2% uranyl acetate. Scale bar: 500 nm.*

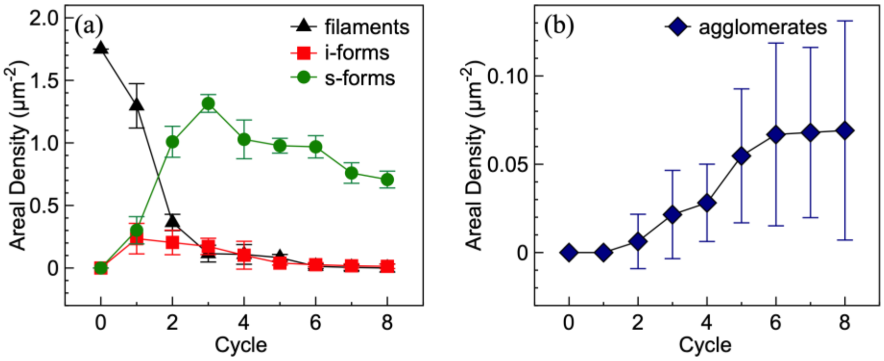

Figure 2.5. *Areal density of (a) Au/ZnS-binding M13 templates and (b) template agglomerates for vortex/rest cycles 0 through 8 using the room temperature transformation process. Prior to chloroform treatment (after 0 vortex/rest cycles), only filaments were observed. After two cycles, spheroids were the prevailing morphology, and after three cycles, although some filaments were still present, the highest concentration of spheroids was measured. Following five cycles, no filaments were found, but the number of spheroids decreased slightly. This decline in spheroids was likely due to agglomeration caused by exposed hydrophobic p8 residue interactions. For each data point, a minimum of 100 particles were counted over 3 different samples. Mean and standard deviation are reported over the three independent samples.*

In addition to the observed shape modification, it was noted that s-form size increased on average from 54 to 68 nm within the first 3 vortex/rest cycles, and continued to slowly expand to 85 nm by cycle 8 (Figure 2.6). A similar gradual progression in transformation and spheroid enlargement was observed in Au-binding phage without a p3 peptide, albeit with a slightly different relationship to vortex/rest cycle.[4] Because no filaments were found after 5 vortex/rest cycles and a relatively high yield of spheroids was achieved, these templates were selected for further study. As illustrated in Figure 2.7a and further supported by Figure 2.8, these Au/ZnS-binding spheroids displayed the rounded, slightly deflated morphology that is characteristic of filamentous Ff class spheroids.[2,4,29,96] The size distribution and average size (77 ± 21 nm) of these spheroids is shown in Figure 2.7b. Dynamic light scattering analysis was also done for these spheroids, and found a hydrodynamic diameter of 134±56 nm, and zeta potential of 17.7±1.5 mV. Interestingly, Au/ZnS-binding spheroid size was appreciably larger than that reported for Au-binding spheroids at the same cycle number (Figure 2.6), indicating a clear effect of the added p3 insertion on spheroid formation.[4]

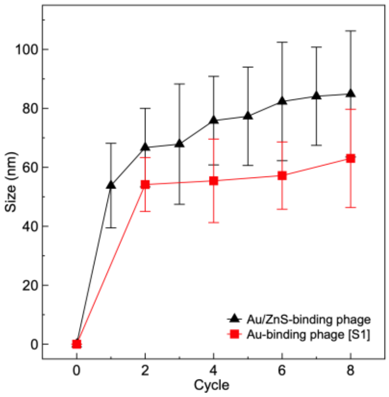

Figure 2.6. *Au/ZnS-binding spheroid size, as measured by TEM,plotted as a function of cycle number for room temperature transformation method. Mean and standard deviation are reported for measurements taken on three independent samples. For comparison, cycle-by-cycle Au-binding spheroid size for room temperature transformation have been included from the literature [S1]. For each data point, a minimum of 100 particles were measured over 3 different samples. Mean and standard deviation are reported over the three independent samples.*

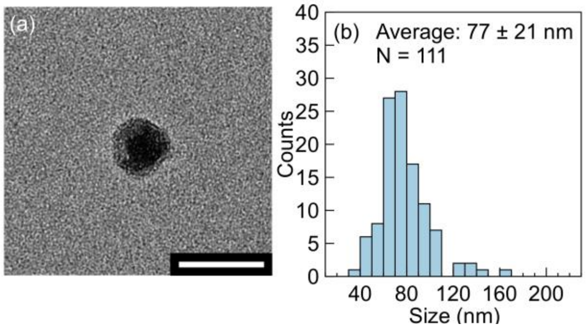

Figure 2.7. *Au/ZnS-binding spheroid (a) morphology and (b) size distribution following 5 vortex/rest cycles with chloroform at room temperature. Samples were stained with 2% uranyl acetate. Scale bar: 100 nm*

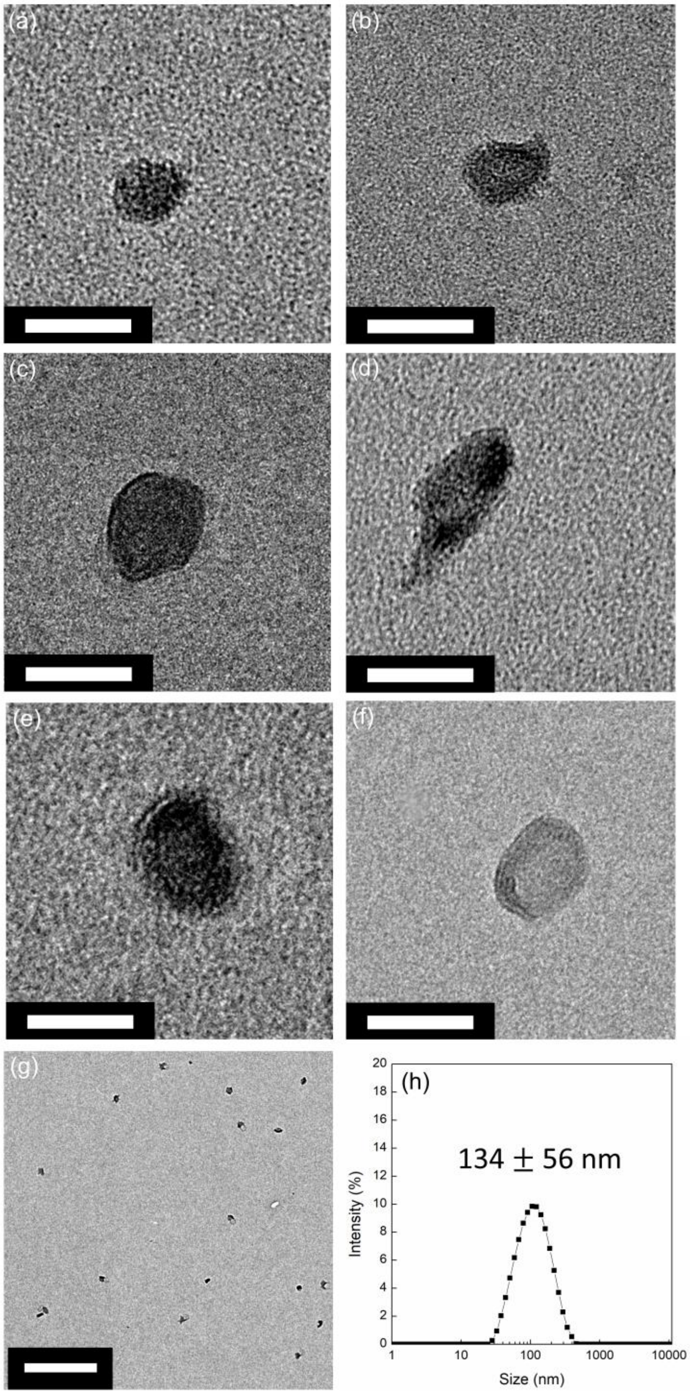

Figure 2.8. *Several Au/ZnS-binding spheroids produced at room temperature with 5 vortex/rest cycles. Samples were stained with 2% uranyl acetate. Scale bar: (a-f) 100 nm, (g) wide field image scale bar: 500 nm. (h) Analysis of hydrodynamic diameter of spheroids using dynamic light scattering. The zeta potential of these particles was measured in the same buffer, and an average value of 17.7 ± 1.5 mV was found.*

2.3.2.2 Secondary structure

Using CD, and fluorescence, effects of the Au and Au/ZnS-binding peptides on secondary structure through the transformation process were measured against each other and WT phage. CD spectroscopy was used to correlate template morphology with changes in M13 viral protein conformation during the transformation process. Cycle-by-cycle spectra of the Au/ZnS-binding phage are shown in Figure 2.9a. The spectrum was dominated by a negative peak in molar ellipticity at 222 nm which decreased in magnitude with each successive vortex/rest cycle. Because 85% of the M13 viral capsid mass is attributed to the helical p8 major coat protein, modifications to its structure are the main contributors to CD.[52, 53] The amino acid sequence of the Au-binding M13 p8 coat protein and its secondary structure are included in Figure 2.9b.[99–101] The 222 nm peak which represents the combined absorption of the p8 α-helix and the chromophore coupling of W26 and F42/F45 residues on neighboring p8 proteins is shown in Figure 2.9c as a function of cycle number.[53] A decrease in 222 nm peak magnitude with chloroform treatment has been attributed to a reduction of π-stacking interactions, followed by a loss of up to 30% of the α-helical secondary structure of the p8 protein.[98] This reduction in helicity is similar to that which occurs during E. coli membrane insertion in which two shorter helices are formed: one amphipathic and one hydrophobic connected by a short hinge region with a handful of flexible residues remaining at either end.[48, 57] In these studies, as described in Figure 2.9c, a dramatic decrease in the 222 nm peak magnitude was observed during the first two cycles, followed by a modest decrease in subsequent cycles. The most significant changes in secondary structure were concurrent with the vortex/rest cycles in which the majority of filaments were converted to spheroids, whereas lesser changes were associated with the transformation of remaining filaments and the gradual expansion of existing s-forms.

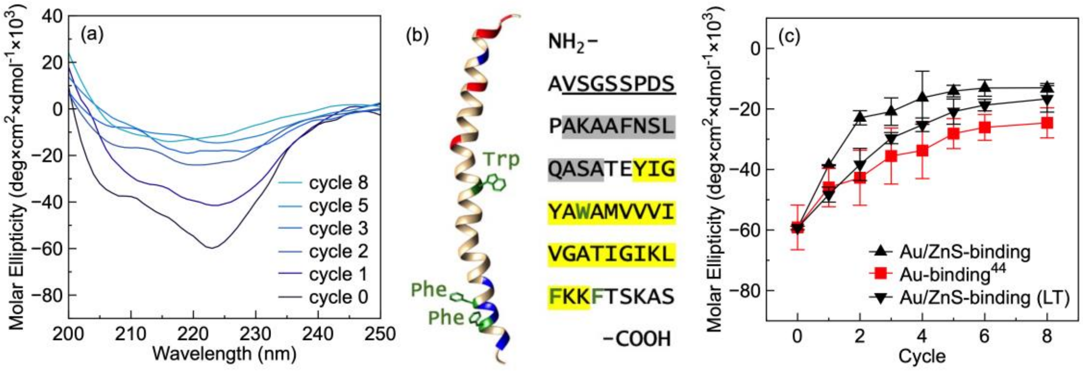

Figure 2.9 *(a) Circular dichroism (CD) spectra of Au/ZnS-binding phage exposed to an increasing number of vortex/rest cycles at room temperature. Spectra were smoothed using a 5 point Savitsky-Golay filter. (b) The secondary structure of the p8 coat protein and corresponding amino acid sequence. The Au-binding peptide sequence is underlined. Grey and yellow highlighted text show amphipathic and hydrophobic helical regions, respectively.*[56] *Within the molecular model, negative, positive, and aromatic residues are indicated in red, blue, and green, respectively. Molecular visualization was performed using Protein Data Bank*[99] *record 2C0W*[100] *and UCSF Chimera.*[56] *(c) Molar ellipticity as a function of cycle number at 222 nm for both the Au/ZnS-binding and Au-binding phage.*[44] *Transformation of the Au/ZnS-binding phage was studied using both room temperature and low temperature (LT) procedures.*

Using fluorescence spectroscopy, the same cycle-by-cycle approach was applied to further study changes within the viral capsid during transformation. Intrinsic tryptophan fluorescence is a strong indicator of the local protein environment such that modifications manifest as wavelength shifts and/or emission quenching. Figure 2.10a presents the emission spectra of the Au/ZnS-binding phage. Fluorescence was primarily dictated by the tryptophan residue, W26, located within hydrophobic region of the p8 protein.[98] As shown in Figure 2.10b and 2.10c, over 8 vortex/rest cycles, the peak wavelength decreased only 10 nm (from 320 to 310 nm), while the peak intensity was reduced by nearly 80%. This relatively small blue shift paired with significant emission quenching indicated a minimal difference in the polarity of the tryptophan environment, but considerable loss of aromatic residue coupling within the viral capsid.[49, 53, 54] After 2 vortex/rest cycles, the point at which the majority of the templates were transformed into spheroids, a 4.5 nm average blue shift was measured. This peak shift is similar to previous reports of spheroid formation in the fd virus, another Ff class phage.[26] The continued decline in wavelength with increasing cycle number was attributed to additional, small changes in the tryptophan environment as neighboring p8 interactions were altered and the spheroidal template grew in size (Figure 2.6). The rate of emission quenching as a function of cycle number varied. The slope of relative intensity versus cycle number was highest between cycles 0 and 2, corresponding to the substantial morphology and intramolecular environment changes in the transition from filament to s-form; slightly reduced between cycles 2 and 4, as residual filaments were converted and spheroids were enlarged; increased again between cycles 4 and 6, reflecting an increase in agglomerate formation (Figure 2.5); and lowest between cycles 6 and 8, where the changes in morphology, agglomeration, and secondary structure were relatively small.

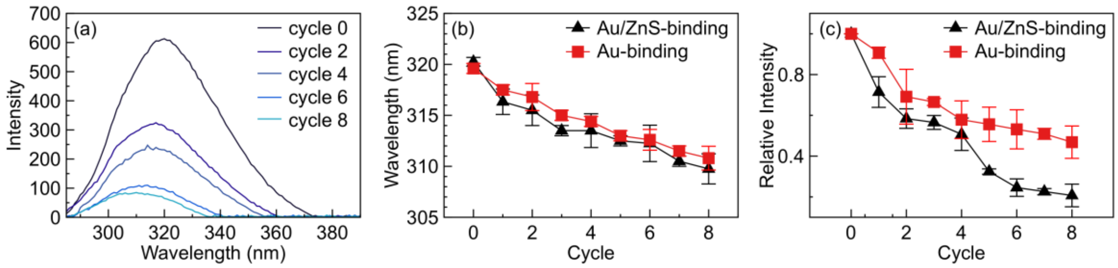

Figure 2.10 *(a) Representative fluorescence spectra of Au/ZnS-binding M13 bacteriophage chloroform treated at room temperature, as well as (b) peak wavelength and (c) relative peak intensity for each vortex/rest cycle. For comparison, the peak wavelength and relative intensity of Au-binding phage without a pIII peptide insert are also shown.*

To evaluate the effect of the p3 peptide insert on template conversion, the cycle-by-cycle CD and intrinsic fluorescence of the Au/ZnS-binding phage were compared to those of an Au-binding phage without a p3 peptide fusion. As shown in Figure 2.9c, Au/ZnS-binding phage molar ellipticity is plotted with values for Au-binding phage from the literature.[4] After 8 vortex/rest cycles, the Au-binding phage retained on average 20% more molar ellipticity at 222 nm, and thus experienced less overall change in secondary structure than the Au/ZnS-binding phage. This observation was reinforced by fluorescence measurements, as demonstrated in Figure 2.10b – 2.10c. While the blue shift was similar for the two phage clones, the Au/ZnS-binding phage exhibited appreciably more quenching (~30%) between 4 and 8 cycles than the Au-binding phage, indicating a greater change in the intramolecular environment. This finding is consistent with the notably larger size of the Au/ZnS-binding spheroids (Figure 2.6) as compared to that reported for Au-binding spheroids.[4]

Contradictions exist within the literature regarding the dependence of transformation on the minor coat protein. Marvin et al. observed that p3 mutations made phage less resistant to organic solvents causing them to be easily converted to intermediate forms, but few details were discussed.[31] In contrast, other researchers have reported that transformation was not affected by the p3, but purely dependent on the arrangement of the major coat protein.[2,29,30] In those studies, filamentous phage were subjected to subtilisin digestion or French pressure cell shearing to remove part or all of the p3 protein. Subsequent analysis focused primarily on the presence of converted structures without more rigorous characterization of morphology, size, or agglomeration, therefore subtle differences in transformation could have been overlooked.

While the exact mechanism for observed differences in chloroform transformation remains unclear, we propose two potential explanations for our findings. First, mutations near the N-terminus may cause partial unfolding of the p3 protein,[103] exposing its otherwise buried hydrophobic region and promoting chloroform interaction.[60, 61] Since the p3 and p6 work cooperatively to cap the proximal end of the M13 virus and maintain the integrity of the assembled major coat protein, increased interaction of the p3 with chloroform may hasten transformation.[38, 62, 63] Alternatively, the p3 may dictate the arrangement of the major coat proteins within the viral capsid, thus a mutation to the p3 could modify neighboring p8 protein interactions, allowing increased chloroform access and altering the conversion process.[24]

2.3.2.3 Comparison to Wild Type (WT)

These secondary structure changes were also characterized for the WT phage, as a first check toward the effects of any peptide insertion. Complete analysis would require a phage containing only the ZnS-binding peptide in the p3, so this analysis is only preliminary. The CD data for WT transformation over 8 cycles is shown Figure 2.11a and shows a less dramatic loss of helicity than for Au-binding phage, and a much less dramatic shift than for Au/ZnS-binding phage. This follows the trend seen in the comparison between the two modified phage, in which fewer genetic modifications lead to a slower shift to the spheroid form. The fluorescence shift and quenching are shown in Figure 2.11b and 2.11c, and correlate with this assumption. While the overall blue shift is similar to that of the two chimeric phage, the degree of quenching is much lower by cycle 8.

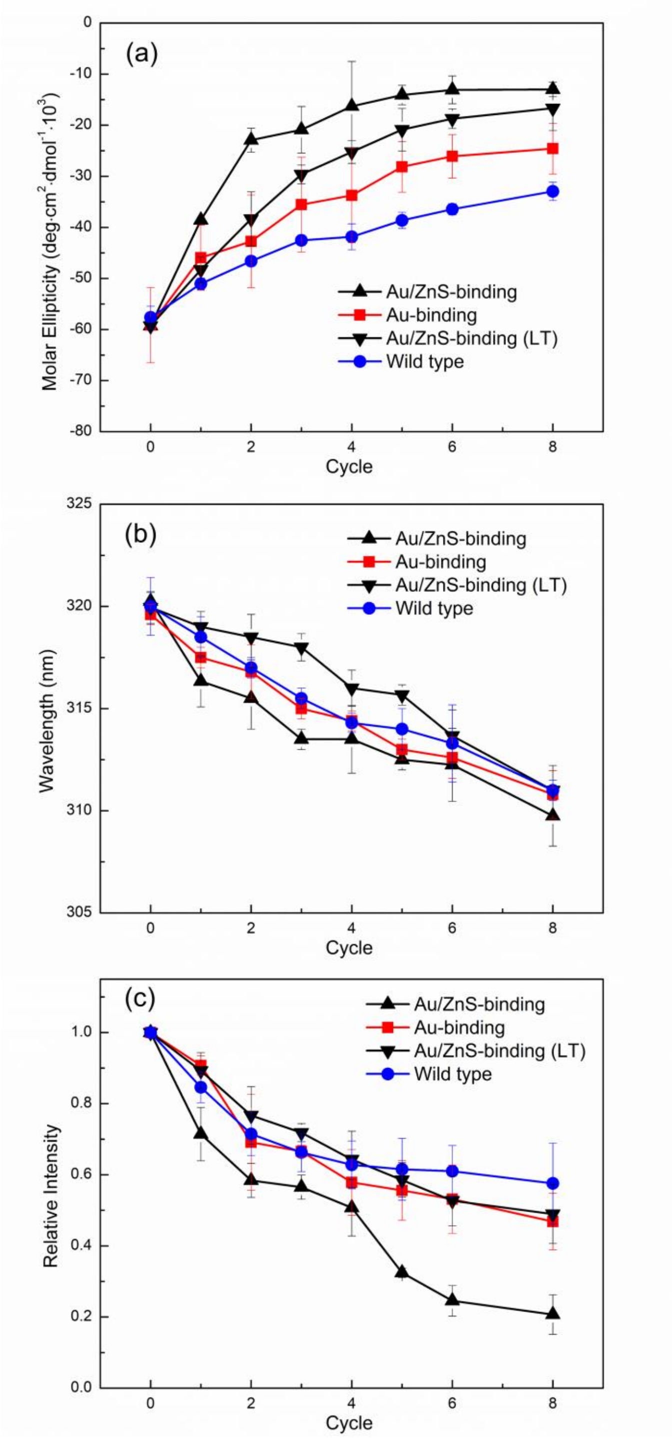

Figure 2.11 *Cycle by cycle analysis of secondary structure of wild type M13. (a) Shift in fluorescence peak wavelength and (b) quenching of relative fluorescence to filamentous form. (c) Magnitude of 222 nm peak measured with circular dichroism spectroscopy.*

2.3.2.4 Low temperature transformation and stability

A transformation process,[26,29] in which bifunctional spheroids were formed from i-forms rather than directly from filaments, was also studied in an effort to better understand the effect of the stepwise shape transition on template properties. Here, the conversion scheme was similar to that shown in Figure 2.3; however, the first 3 cycles of the transformation process occurred at 0°C, followed by additional room temperature cycles. Au/ZnS-binding M13 capsid morphologies after 3 and 5 vortex/rest cycles are shown in Figures 2.12a and 2.12b, while associated viral template areal densities are plotted in Figure 2.13. Similar to the room temperature procedure, initial vortex/rest cycles produced a blend of filaments, i-forms, and spheroids. Because of the reduced temperature, rather than spheroids, i-forms were the prevailing template structure in early cycles. These i-forms, approximately 140 nm in length, contracted during subsequent room temperature cycles until only s-forms remained (Figure 2.13).

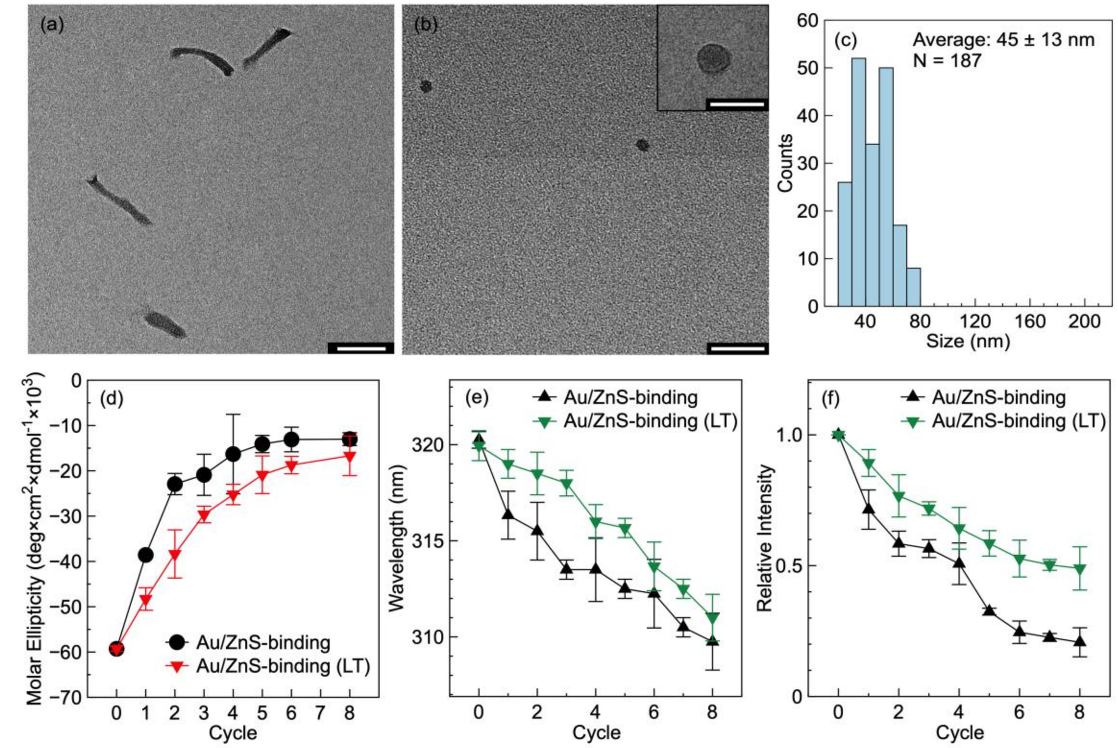

Figure 2.12. *TEM images of Au/ZnS- binding phage after (a) 3 cycles and (b) 5 cycles; scale bar: 100 nm. Inset: High magnification TEM images of individual M13 templates; scale bar: 50 nm. Samples were stained with 2% uranyl acetate. (c) A histogram of spheroid sizes produced using 5 cycles of the LT transformation process. (d) Molar ellipticity as a function of cycle number at 222 nm as prepared by room temperature and low temperature (LT) transformation methods. The first three vortex/rest cycles were held at 0°C for LT transformation. Fluorescence (e) peak shift and (f) quenching by room temperature and LT transformation methods. Mean and standard deviation are reported for measurements taken on three independent samples.*

For comparison to room temperature transformation, the spheroid size distribution and average size (45 ± 13 nm) were evaluated after 5 vortex/rest cycles, and are found in Figure 2.12c. In addition, several examples of LT spheroid morphology found after 5 cycles are shown in Figure 2.14. Notably, spheroids produced from i-forms using the LT procedure were about 32 nm smaller and more uniform in geometry than those created directly from filaments. Dynamic light scattering analysis was also done for these spheroids, which found a hydrodynamic diameter of 88±25 nm, which was a substantially smaller standard deviation than the room temperature prepared spheroids.

The zeta potential of the particles was found to be 21.2±1.2 mV, significantly more electronegative than the room temperature prepared spheroids. In addition, unlike spheroids produced at room temperature, a minimal increase in spheroid size was observed up to cycle 6 (Figure 2.15).

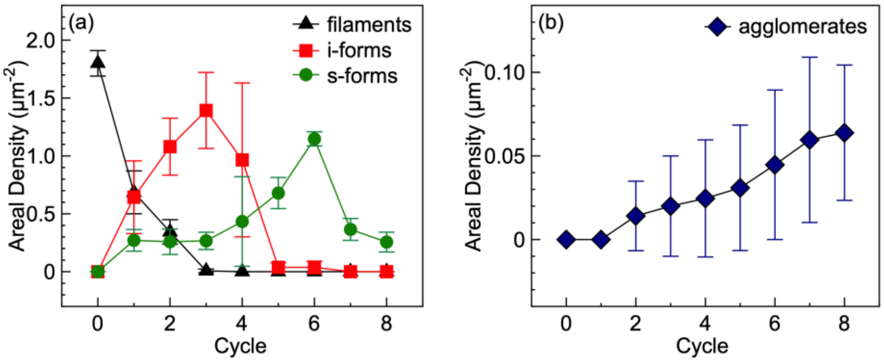

Figure 2.13 *Areal density of (a) Au/ZnS-binding M13 templates and (b) template agglomerates for vortex/rest cycles 0 through 8 using the LT transformation process.*

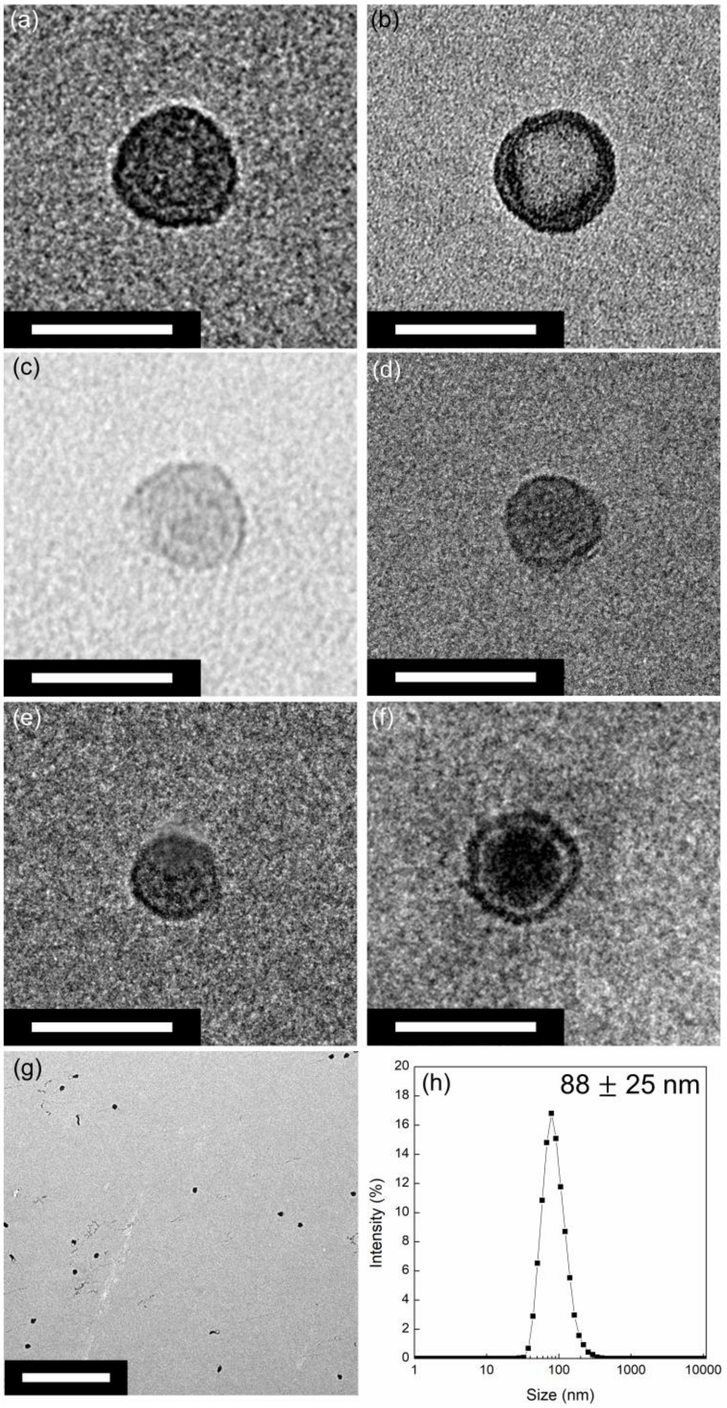

Figure 2.14. *Several Au/ZnS-binding spheroids produced with 5 vortex/rest cycles of the LT transformation procedure. Samples were stained with 2% uranyl acetate. Scale bar: (a-f) 50 nm, (g) wide field image scale bar: 500 nm. (h) Analysis of hydrodynamic diameter of low temperature produced spheroids using dynamic light scattering. The zeta potential of these particles was measured in the same buffer, and an average value of 21.2 ± 1.2 mV was found.*

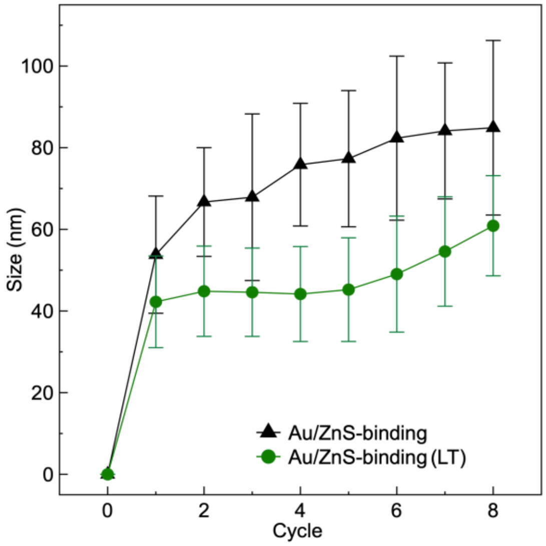

Figure 2.15. *Spheroid size, as measured by TEM, as a function of vortex cycle number as prepared by room temperature and low temperature (LT) methods. The first three vortex/rest cycles were held at 0°C for LT transformation. For each data point, a minimum of 100 particles were measured over 3 different samples. Mean and standard deviation are reported over the three independent samples.*

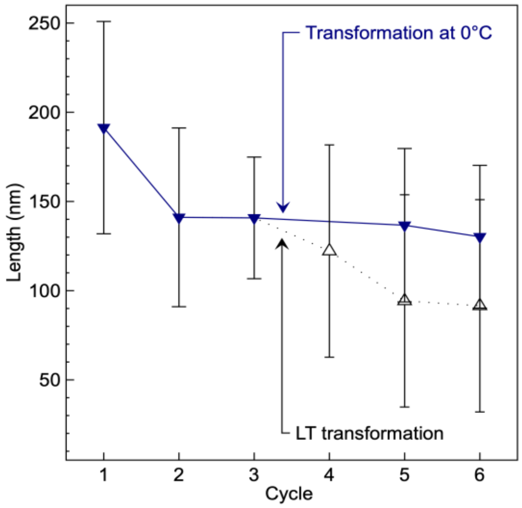

Figure 2.16 *Average length of Au/ZnS-binding i-forms measured as a function of vortex/rest cycle number. Results of two transformation processes are shown: the LT process in which the initial 3 cycles are held at 0°C then brought to 25°C for the remaining cycles and a process in which all cycles are held at 0°C.*

The reduction in size and lack of spheroid expansion for the LT procedure are consistent with cycle-by-cycle CD data (Figure 2.12d) which revealed a lower overall loss in 222 nm molar ellipticity as compared to the room temperature transformation process. Similarly, fluorescence quenching (Figure 2.12e) and peak shift (Figure 2.12f) were more gradual and showed less change overall than room temperature-produced spheroids. The significant quenching seen in cycles 4 through 8 for the room temperature process was not see in the LT procedure, which correlates with the significant difference in spheroid sizes at those cycles. This difference is similar to that seen when comparing Au-binding and Au/ZnS-binding spheroids. The cooled cycles appear to have trapped the capsid in the transition between filament and spheroid structures.[41, 42] As evidence, in Figure 2.16, if all vortex/rest cycles were held at 0°C, i-form contraction halted and i-form length remained constant. These results are in agreement with previous studies, which showed that if the chloroform/water interaction occurs at low temperatures, the telescoping effect can be halted, producing asymmetric rod-like i-forms with a slight flare near the p3 end.[29,30,108] The temperature-induced pause in transformation reduced the assortment of template geometries and avoided further deterioration of p8-p8 interactions in subsequent vortex/rest cycles, ultimately focusing template geometry and increasing spheroid monodispersity. Uniform template dimensions are essential for the synthesis of asymmetric nanostructures with a narrow size distribution. If temperatures of the final cycles were increased, spheroid sizes were comparable to original room temperature-produced spheroids (data not shown), indicating that the controlled temperature of the final cycles were essential in controlling the final size of the spheroids.

Spheroid stability was dependent on transformation temperature. As shown in Figure 2.17 when stored in TBS buffer at 4°C, the areal density of spheroid templates generated using the room temperature procedure decreased rapidly with time as the agglomerate density increased. Within 10 hours of spheroid formation, only 16% of the initial spheroid density remained, whereas the agglomerate density nearly quadrupled. These findings are consistent with the observations of Stopar et al. that M13 spheroids produced at room temperature were not stable for long times.[109] In contrast, spheroids created using the LT process were much less susceptible to agglomeration, retaining as much as 80% of initial areal density over the same time period. The compact structure of these smaller, more monodisperse spheroids may limit solvent exposure of hydrophobic residues within the p3 or p8 proteins (particularly those that terminate the phage body) which can reduce agglomeration. Au/ZnS-binding spheroids produced via the LT approach with 5 vortex/rest cycles were selected for further study.

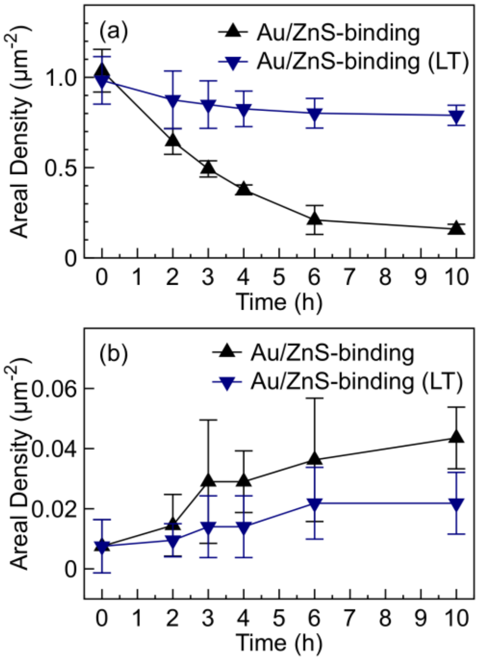

Figure 2.17 *Areal density of Au/ZnS-binding (a) spheroids and (b) agglomerates observed with TEM as a function of storage time. Spheroids produced with both room temperature and LT conversion processes were explored. Viral templates were stored in TBS buffer at 4°C following transformation.*

2.3.3 Synthesized materials on filament and spheroidal M13

2.3.3.1 p3 directed ZnS synthesis

To demonstrate the utility of the M13 spheroid as a bi-functional template, transformed Au/ZnS-binding phage were used to sequentially synthesize ZnS on the p3 minor coat protein and Au on the p8 major coat protein. Following ZnS synthesis, Au/ZnS-binding spheroids and related synthesis products were examined with TEM. Spheroids remained largely intact, growing slightly in size to 48 ± 14 nm (Figure 2.18), while template agglomeration increased by a factor of 3. The larger number of agglomerates was attributed to non-specific, electrostatic screening of the spheroid surface charge by Zn ions. As evidence of Zn ion interaction, viral templates did not require staining post synthesis. As shown in Figure 2.19a, nanoparticles 5.1 ± 1.4 nm in size with an average aspect ratio of 1.23 were synthesized on approximately 72% of the non-agglomerated Au/ZnS-binding spheroids.

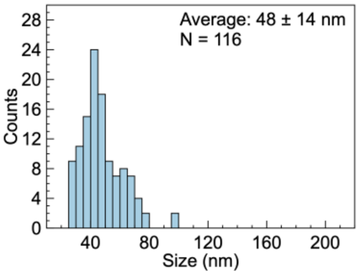

Figure 2.18 *Histogram of Au/ZnS-binding spheroid size distribution after ZnS synthesis.*

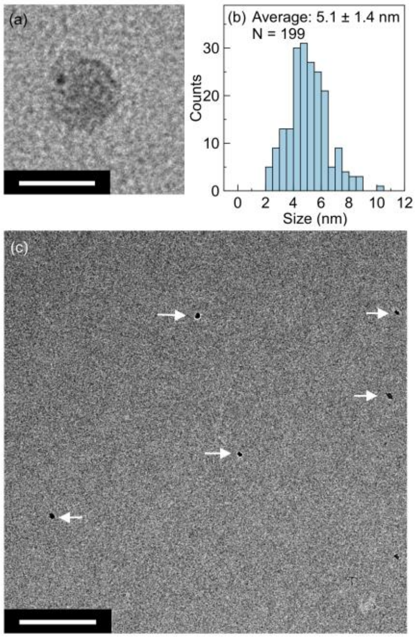

Figure 2.19. *(a) Representative TEM image of ZnS nanoparticle synthesized on a Au/ZnS-binding spheroid; scale bar: 50 nm. (b) Histogram of spheroid-templated ZnS nanoparticle size distribution. (c) Low magnification TEM image of spheroids following ZnS synthesis. Spheroids are indicated by white arrows; scale bar: 500 nm. Samples were not stained prior to imaging.*

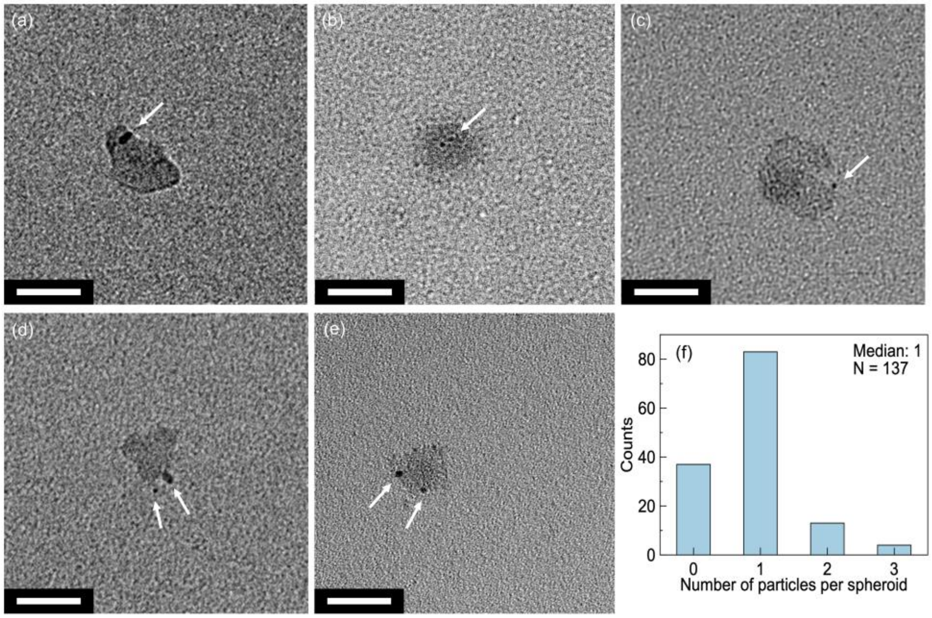

Figure 2.20. *TEM images of spheroids on which (a-c) one or (d, e) two ZnS particles have been synthesized. Samples were not stained; scale bar: 50 nm. (f) Histogram of the number of ZnS nanoparticles synthesized per spheroid.*

While a single particle was observed on most spheroids, a few templates displayed up to 2 or 3 particles (Figure 2.20). The rather small number of particles synthesized per spheroid was consistent with selective p3 growth. Lattice fringes from an individual nanoparticle, consistent with both ZnS zinc-blende (111) and wurtzite (002) interplanar distances, can be seen in Figure 2.21a. An electron diffraction pattern and associated TEM image of concentrated synthesis products are shown in Figure 2.21b. As described in Table 2.1, measured d-spacings were indexed to interplanar spacings of both hexagonal and cubic ZnS structures, indicating that a mixture of the two polytypes was synthesized. Given that previous reports of ZnS synthesis directed by the same peptide

(CNNPMHQNC) produced only wurtzite ZnS on both M13 and P22 viruses,[27, 35] the presence of the cubic form of ZnS was unexpected. Yet, notably, polycrystalline sphalerite was used during the selection of the ZnS-binding peptide,[87] therefore the synthesis of zinc-blende under altered growth conditions was reasonable.

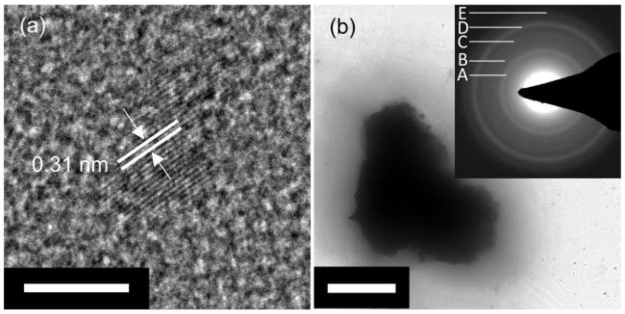

Figure 2.21 *(a) HRTEM image of spheroid-templated ZnS nanoparticle. Lattice fringes corresponding to ZnS zinc-blende (111) and wurtzite (002) are denoted; scale bar: 5 nm. (b) TEM image of concentrated spheroid-templated ZnS synthesis products; scale bar: 500 nm. In set: Selected area electron diffraction pattern of crystalline ZnS material indexed to crystallographic planes in Table S1.*

Table 2.1 Measured d-spacing and corresponding crystal planes for materials synthesized on Au/ZnS-binding M13 spheroids.

Label	Measured d-spacing (Å)	ZnS, zinc-blende	ZnS, wurtzite	Au, face-centered cubic
ZnS				
A	3.15	(111)	(002)	
B	2.72	(200)		
C	2.27		(102)	
D	1.93	(220)	(110)	
E	1.70	(311)	(200)	
Au/ZnS				
A	3.29		(100)	
B	2.74	(200)		
C	2.34			(111)
D	2.05			(200)
E	1.66	(311)	(200)	
F	1.41	(400)	(104)	(220)

For direct comparison, ZnS was also synthesized under the same conditions using filamentous Au/ZnS-binding phage and wild-type phage (filaments and spheroids), as well as without a phage template. Interestingly, the template shape did not largely affect the particles per template, average nanoparticle size, or aspect ratio of the inorganic material on the p3 minor coat protein (Figure 2.22 and Table 2.2). This finding differs somewhat from that associated with synthesis of inorganic material on the p8 major coat protein.[4] While chloroform treatment triggers a significant change in p8 packing density and impacts ion adsorption, a similar effect does not appear to occur for the p3. No ZnS growth was observed on wild-type spheroids or filaments. Large, highly amorphous particles were created without a viral template (Figure 2.23).

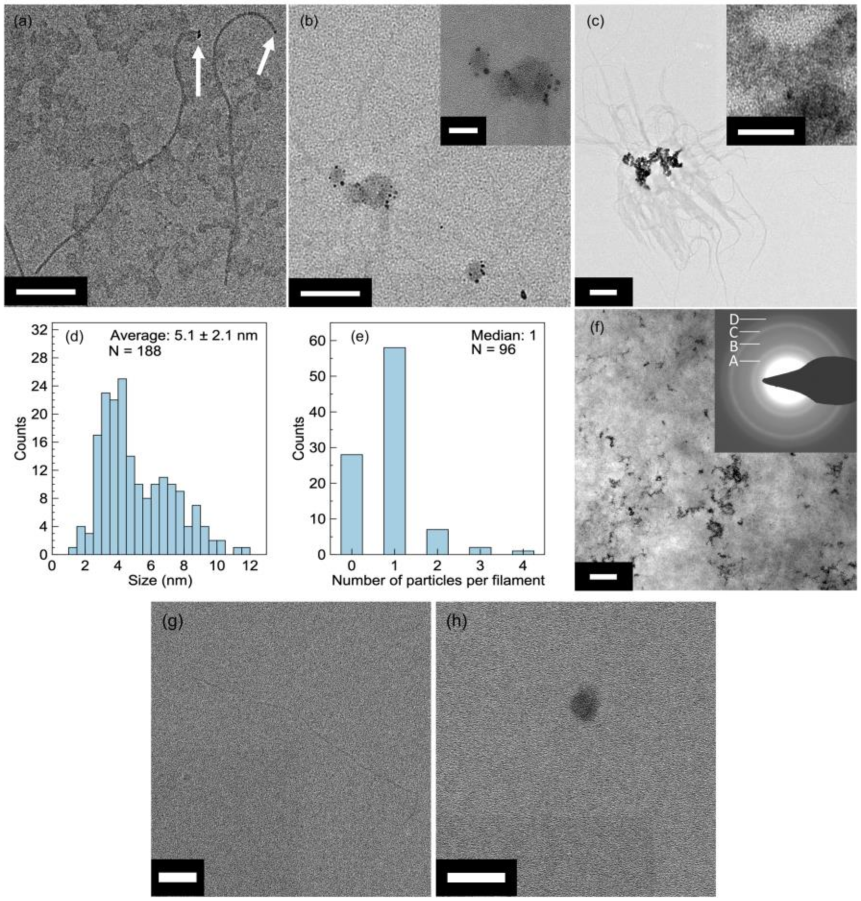

Figure 2.22. *TEM images of ZnS synthesis products on (a) individual phage and (b-c) micelle-like structures formed by Au/ZnS-binding filaments; scale bar: 200 nm. Insets: High magnification images of ZnS nanoparticle clusters; scale bar: 10 nm. Histograms of (d) the filament-templated ZnS particle size distribution and (e) the number of ZnS particles synthesized per Au/ZnS-binding filament. (f) TEM image of concentrated filament-templated ZnS synthesis products; scale bar: 200 nm. Inset: Selected area electron diffraction pattern of crystalline ZnS material indexed to crystallographic planes in Table S2. Under the selected synthesis conditions, Au/ZnS-binding filaments tended to surround groups of ZnS particles in micelle-like structures. Nonetheless, many individual filamentous phage were still visible for analysis. In these individual templates, ZnS particles were located almost exclusively at one end of the virus, providing qualitative evidence of p3 site-specific growth. The template shape did not largely affect the particles per template, average nanoparticle size, or aspect ratio of the inorganic material on the p3 minor coat protein. No ZnS growth was observed on wild-type (g) filaments or (h) spheroids; scale bar: 100 nm.*

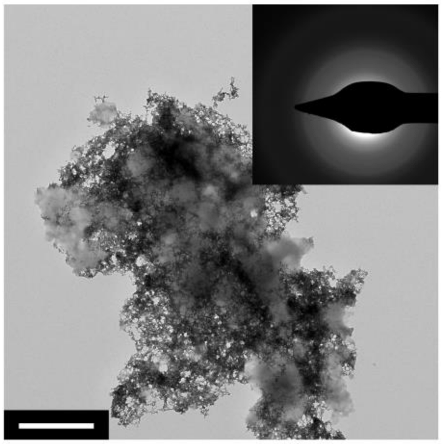

Figure 2.23 *TEM image of ZnS synthesized without a viral template; scale bar: 1 µm. Inset: Electron diffraction pattern of ZnS material.*

Table 2.2 *Measured d-spacing and corresponding crystal planes for ZnS synthesized on Au/ZnS-binding M13 filaments.*

Label	Measured d-spacing (Å)	ZnS, zinc-blende	ZnS, wurtzite
	ZnS		
A	3.33		(100)
B	2.65	(200)	
C	1.92	(220)	(110)
D	1.66	(311)	(200)

Au was subsequently synthesized on the same spheroidal templates, targeting the p8 protein of the Au/ZnS-binding spheroids. As revealed in Figure 2.24, a median of thirteen nanoparticles, 7.9 ± 1.5 nm in size, and occasionally fused together were templated on the surface of the spheroids. The spatial homogeneity of the nanoparticles on the spheroidal template was consistent with p8-directed synthesis.

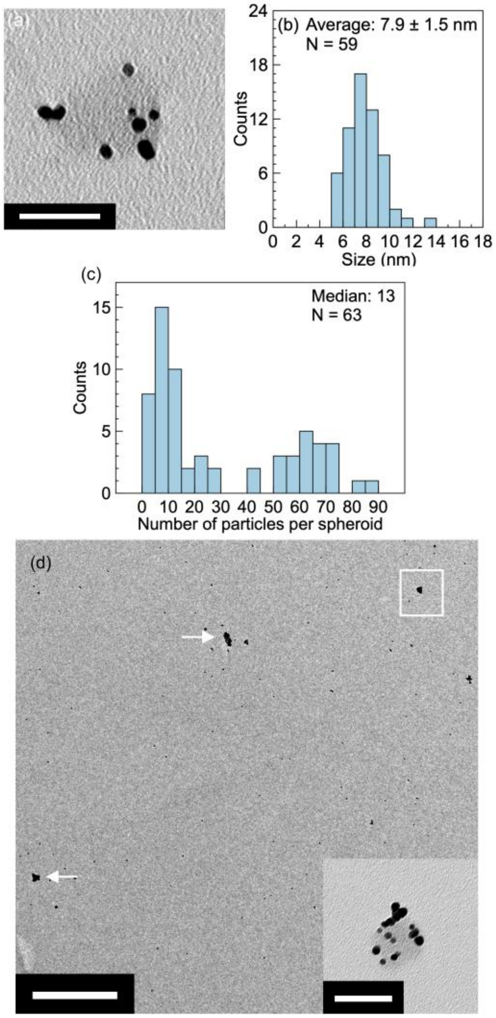

Figure 2.24 *(a) Representative TEM image of Au/ZnS-binding spheroid after sequential ZnS and Au synthesis; scale bar: 50 nm. Samples were not stained prior to imaging. (b) Histogram of Au nanoparticle size distribution on Au/ZnS-binding spheroids. (c) Histogram of Au nanoparticles synthesized per spheroid. (d) Wide field TEM of spheroids following ZnS then Au synthesis, arrows indicate spheroids with synthesized Au, and inset shows spheroid in box; scale bar: 500 nm, inset scale bar: 50 nm.*

As portrayed in Figure 2.25a, the EDS spectrum of the synthesis products confirmed the presence of Au, Zn, and S. Lattice fringes from one of many discrete nanoparticles on the spheroid surface revealed an interplanar spacing of 0.23 nm which is consistent with Au (111), as shown in Figure 2.25b. Measured d-spacings, shown in Figure 2.25c and Table 2.1, were indexed to interplanar distances of both ZnS and Au, further corroborating the presence of both materials on the bi-functional spheroidal templates.

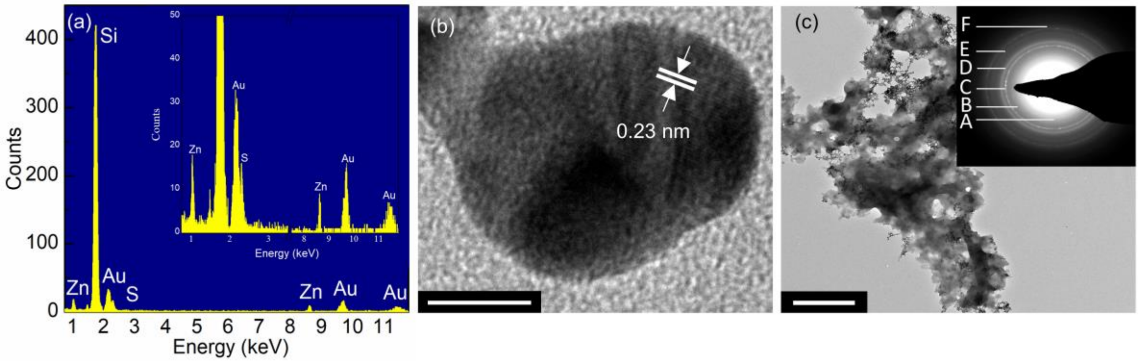

Figure 2.25 (a) EDS spectrum of Au/ZnS-binding bifunctional spheroid synthesis products. Inset: EDS spectrum with scaled y-axis to emphasize elemental Zn and S peaks. (b) HRTEM image of spheroid-templated Au nanoparticles synthesized after ZnS nanoparticle formation; scale bar: 5 nm. (c) Low magnification TEM image of concentrated synthesis products; scale bar: 1 μm. Inset: Electron diffraction pattern of Au/ZnS synthesis products. Measured lattice spacings are shown in Table S1. Synthesis products were concentrated with centrifugation prior to EDS and ED to enhance signal.

For comparison, Au was synthesized under the same conditions with Au/ZnS-binding filaments (Figure 2.26), wild-type phage (filaments and spheroids), and without a template using the same conditions. In all cases, nanoparticles were smaller in size and fewer in number than those templated by Au/ZnS-binding spheroids. These results show that the Au/ZnS-binding spheroids produced through low temperatures are capable of acting as templates for sequential synthesis of two inorganic materials. Furthermore, this evidence suggests ZnS growth is selectively guided by the p3 protein, and Au growth by the p8 protein, which leads to the asymmetric assembly of these materials on spheroids. To see if any structural changes occurred to the phage protein during ZnS and Au synthesis, CD measurements were taken following each procedure, shown Figure 2.27.

No significant differences were observed in the 222 nm peak after 10 hours, ZnS synthesis, or Au synthesis.

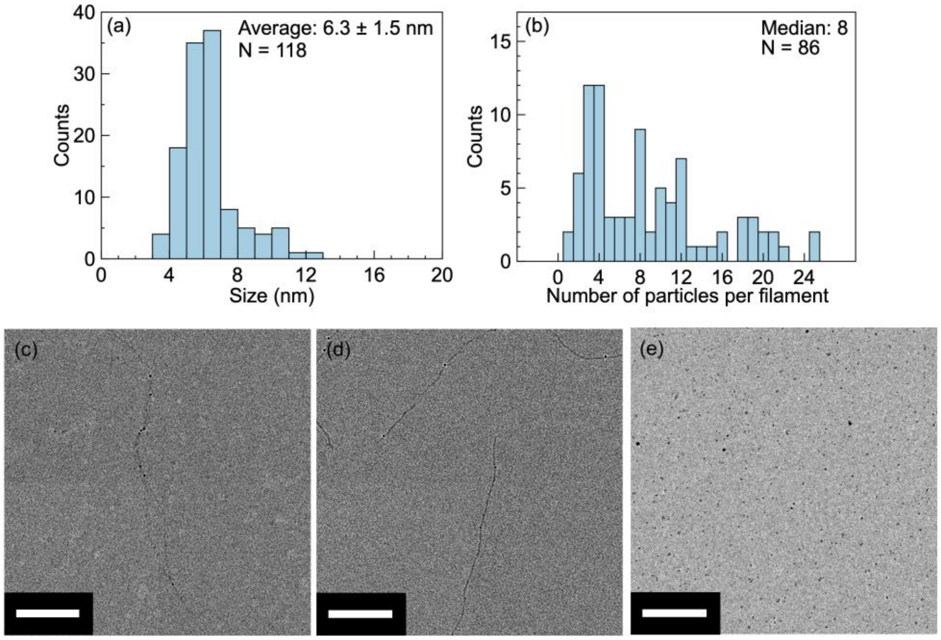

Figure 2.26 *Histograms of (a) the filament-templated Au nanoparticle size distribution and (b) the number of Au nanoparticles synthesized per Au/ZnS-binding filament. (c, d) TEM images of individual Au/ZnS-binding filaments following sequential ZnS and Au synthesis. Several agglomerates were also observed after synthesis. (e) Au nanoparticles synthesized without a template. Au nanoparticles synthesized without a template had an average size of 6.0 nm, whereas little to no growth was observed on wild-type spheroids and filaments. In all cases, nanoparticles were smaller in size and fewer in number than those templated by Au/ZnS-binding spheroids. Scale bar (c,d): 250 nm, scale bar (e): 100 nm.*

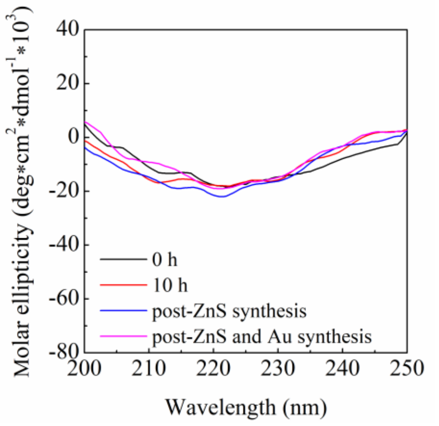

Figure 2.27 *Circular dichroism (CD) spectra of Au/ZnS-binding spheroids produced with the LT process following inorganic material synthesis. For comparison, measurements were also made on spheroids prior to synthesis (0 h) and after incubation in TBS at room temperature to mimic synthesis times (10 h). Spectra were smoothed using a 5 point Savitsky-Golay filter.*

2.4 Conclusion

In summary, we have investigated the distinct progression of a M13 Au/ZnS (p8/p3)-binding bacteriophage from filament to spheroid and demonstrated its potential as a scaffold for non-centrosymmetric Au/ZnS nanostructure synthesis. The incorporation of the ZnS-binding motif within the p3 affected transformation, producing larger spheroids with greater loss of secondary structure than reported for Au-binding phage without a p3 peptide fusion. More work is needed to fully describe the relationship between the p3 modification and the chloroform-guided transformation process. Nonetheless, these observations have interesting implications for the versatility of the spherical template and suggest the potential to adjust spheroid size through p3 peptide motif design. The use of low temperature (0°C) vortex/rest cycles to produce i-forms that were subsequently converted to spheroids created more monodisperse and agglomeration resistant Au/ZnS-binding spheroids. These bifunctional spheroidal templates were used to direct sequential, site-specific synthesis of ZnS on the p3 and Au on the p8, generating non-centrosymmetric hybrid metal/semiconductor nanostructures. The ability to assemble two dissimilar and asymmetrically positioned materials on the M13 spheroid is an important achievement towards hetero-junction formation that significantly expands the utility and potential applications of this viral template.

Chapter 3. Heterojunction formation and photocatalytic dye degradation

3.1 Introduction

Recently, water pollution has been an on-going issue worldwide. A major contributor to this problem is the textile industry, as dye-containing waste-water is often released from factories into the environment.[110] Many dyes are known to be carcinogenic to humans and animals,[7,111] yet are not easily removed from water in typical waste treatment facilities,[6,112] requiring new methods of elimination. Many dyes are also 'bleached' by single reduction or oxidation steps, making them good indicators for redox processes with simple absorption measurements. As a result, much research has gone into the activity of solar light driven catalysts as measured through dye degradation.[11] In particular, wide-bandgap semiconductor photocatalysts show potential in this application, as they have ideal band positions for the reduction and oxidation reactions necessary to degrade most dyes.[12] However, the most efficient photocatalysts tend to be UV absorbing, so it would be beneficial to absorb visible light wavelengths, where the solar spectrum illumination is much stronger. Through the property of localized surface plasmon resonance (LSPR), some metal nanoparticles are able to absorb visible light wavelengths, making them an attractive addition to semiconductor particles. [17]

In the case of ZnS, negligible light longer than ~350 nm is absorbed, but Au nanoparticles are able to absorb across the majority of the visible spectrum due to their LSPR.[113] Still, direct plasmonic-enhanced absorption is unlikely since there is little overlap in energy levels.[114–116] However, visible light photocatalysis is still possible through the higher energy resonant electrons in Au, termed hot electrons, when they can overcome the Schottky barrier between Au and ZnS.[114,115] Due the Fermi level pinning effect, a substantial fraction of Au's resonant electrons will have a higher energy than the Schottky barrier, allowing substantial charge separation under visible light. Further, the configuration of the particles has shown to have significant impact on this process. Compared to centrosymmetric particles, in an asymmetric, Janus-like configuration, the plasmonic effects are greatly enhanced at the interface.[117] In addition, this orientation of the two particles serves to maximize their environmentally exposed surface areas, making it ideal for photocatalytic reactions. Unfortunately, at the nanoscale, there are limited methodologies for synthesizing asymmetric particles,[73,75] and each show challenges in scalability. However, the M13 provides a solution to this as a material template, as they offer simplicity in production[88] can be easily modified to direct synthesis and configuration of many materials.[3,4,34,85,118]

Within the scope of viruses that are often used in material templating, there are few examples of bi-functionality,[37,38,119] and there a fewer still of those able to orient the material in an asymmetric manner.[80,120,121] Also, the examples of asymmetry are independent of the examples of bi-functionality. The major reason for this is that the vast majority of viruses used as material templates are centrosymmetric in structure. However, the M13 bacteriophage can address these issues simultaneously,[34,122] and act as a template for Janus-like nanoparticles. The virus' capsid structure contains multiple surface protein groups, mainly the p3 and p8 proteins, which can be independently modified to recognize unique inorganic materials. Along with this, these proteins groups are natively arranged in an asymmetric fashion.[25] While it is normally in a micron-long filamentous form, it is easily converted into a sub-100 nm spheroid[2] which preserves the protein asymmetry in a compact manner.[30,122] While the M13 has been used for its bi-functionality as a template, its filamentous form does not provide close contact for the two materials. In this regard, its spheroidal form is ideal in directing synthesis of the two materials in such a way as to create a heterojunction, an essential step in producing a Schottky barrier between a metal and semiconductor.

This following chapter examines the M13 spheroid as a template for heterojunction synthesis between ZnS and Au nanoparticles. The Au and ZnS-binding template was used , however, synthesis conditions were modified to yield larger ZnS particles and increased Au growth. These asymmetric particles were then used for the photocatalytic degradation of aqueous dyes. The Au was added for its plasmonic properties, which allowed visible light-driven photocatalysis, which ZnS is normally transparent to. The heterojunction interface was then restricted, which showed that a high interfacial area was essential for charge transfer between the materials. This work marks one of the first applications of the M13 spheroid, and one of the first virus templates to be used in photocatalysis. Its showcases the potential of the spheroidal form in facile, inexpensive nano-heteroparticle synthesis, and an essential first step in its applicability.

3.2 Experimental

3.2.1 M13 bacteriophage clone preparation and chloroform transformation

A Au/ZnS-binding M13 bacteriophage spheroid was used to assemble asymmetric spherical particles. This phage displayed Au-binding (VSGSSPDS) and constrained ZnS-binding (CNNPMHQNC) peptides on its p8 and p3 proteins, respectively, which was first converted to spheroid form.[122] Spherical transformation was performed by preparing a 100 μL solution of phage ($1 * 10^8$ pfu/μL) in pH 7.5 tris-buffered saline (TBS, 50 mM tris-HCl, 100 mM NaCl, Fisher Scientific) and 100 μL chloroform (amylene stabilized chloroform, ACROS Organics) solutions on ice for 20 s to chill. The solutions were combined, then vortexed five times in on/off cycles of 2 s/13 s, the first cycle at high power, and the following four at low power. During the cycles, the first three were held at 0°C. The solution was placed in a 37°C water bath for 20 s, then finally vortexed at room temperature for the last two cycles. After vortexing, 90 μL of chloroform was pipetted out, and any remaining was evaporated via gently blowing with lab air flow for about 20 s. Spheroids were immediately used in material synthesis or photocatalysis.

3.2.2 ZnS and Au synthesis

Following transformation, ZnS[123,124] and then Au were synthesized to create a nanoparticle heterojunction. Synthesis procedures for ZnS and Au were adapted from previously reported methods, and the ZnS process was modified to yield larger particles.[4,34,85,122,124] To synthesize ZnS on the p3 protein, a 50 μM solution of zinc chloride ($ZnCl_2$, Sigma Aldrich) was prepared in 100 μL of tris-buffered saline with freshly made spherical phage ($1*10^8$ pfu/μL). The solution was stored at 4°C for 3 h. An equal volume of 10 μM sodium sulfide (Na_2S, Sigma Aldrich) was prepared in deionized water. Both solutions were placed on ice, following which, the Na_2S solution was added dropwise in 10 μL increments to the $ZnCl_2$ and phage solution over the course of an hour. The entire solution was then incubated at room temperature for an additional 6 h to produce ZnS particles on the p3 protein.[85] Residual ZnS precursors were removed via centrifugal filtration (Amicon Ultra-0.5, 3 kDa, Millipore) and synthesis products were resuspended in TBS. Following ZnS synthesis, the p8 of the spheroid was targeted for Au synthesis.[122,125]. To form a herojunction, Au was then grown. A 200 μL volume of phage ($5*10^7$ pfu/μL) with ZnS was mixed with sodium borohydride ($NaBH_4$, Sigma Aldrich) to achieve a 6 μM solution. Subsequently, 2.5 μL of chloroauric acid ($HAuCl_4$, Sigma Aldrich) was added for a final concentration of 150 μM, and incubated for 5 min.[34]

To prepare samples for characterization and photocatalysis, any remaining synthesis precursor was removed. To remove the precursor, products were centrifuged down, and supernatant was replaced with fresh water. To reduce agglomeration during the process, citrate and Tween-20 were added to phage/ZnS/Au solutions prior to centrifugation to achieve concentrations of 10 μM and 0.1 vol%, respectively. Solutions were centrifuged at 400 rcf for 30 min, the supernatant removed, and then replaced with fresh deionized H_2O. They were then vortexed, and finally sonicated for 30 min to fully resuspend in solution. Samples were immediately prepared for TEM, spectroscopic measurements, or photocatalytic measurements.

To observe effects of interfacial contact area on charge transfer between ZnS and Au, Au nanoparticles (AuNP) were bound to phage rather than through synthesis. Small, 5 nm Au nanoparticles (Ted Pella, Inc.) were bound to spheroids in a ratio of 110:1 particles per virus. This ratio was chosen in order to achieve complete coverage of the virus. The solutions was incubated for 10 min. They were then centrifuged for 30 min at 400 rcf to remove unbound particles, and resuspended in 300 μL of fresh deionized water.

As controls, ZnS and Au were also synthesized alone on templates using identical process to above. Synthesis procedures were repeated without template in order to observe phage's effect on growth.

3.2.3 Material characterization

Morphology of ZnS and Au synthesis products was studied using transmission electron microscopy (TEM, Tecnai T12 or S/TEM Titan Themis 300, FEI). Crystal structure of materials was determined using electron diffraction (ED) and high resolution TEM (HRTEM). Elemental analysis of the synthesis products was completed using energy dispersive spectroscopy (EDS).

Samples were prepared for TEM by placing a 5 μL volume of solution on a formvar/carbon-coated copper grid (Ted Pella, Inc), incubating for 5 min, and washing twice with deionized water. To concentrate synthesis products and remove precursors for ED and EDS, Au and ZnS-containing samples were concentrated via centrifugation by pelleting at 14,000 rcf for 15 min, and washing with deionized water. Centrifugation and washing steps were repeated two more times. For ZnS and Au containing samples, a volume of 20 µL of the concentrated product was dropcast onto a SiN grid (Electron Microscopy Sciences). Formvar-free SiN grids were used to limit Carbon deposition during scanning for elemental analysis. ImageJ[126] was used to measure synthesis product size and aspect ratio, using only 11,000x magnification TEM images for analysis. ZnS and Au synthesis products typically were not symmetric in shape, so size was determined by averaging long and short particle axes, and aspect ratio was determined by dividing the two. For all measurements, a sample size of at least 150 was used for each.

In order to determine what excitation sources to use for photocatalysis, characterize plasmon absorption in Au and bandgap in ZnS, optical absorbance of spheroidal template and inorganic materials was measured from 220 to 950 nm using a UV-Vis spectrophotometer (Evolution 60, Thermo Scientific). Measurements were taken on three independent samples and averaged. All samples were measured in solution using a 100 µL, 1 cm pathlength quartz crystal cuvette (Starna), using deionized water as a baseline correction.

To detect photoactive states in ZnS, and characterize effects of Au on those states, material photoluminescence was measured via spectrofluorometer (Quanta Master 400, Horiba). Room temperature luminescence scans were taken from 270-400 nm with the following parameters: 5 nm slit widths, 1 s integration time, 1 nm step size, and 255 nm excitation source. Measurements were taken on three independent samples and averaged.

All measurements were done in aqueous solution using a quartz crystal micro-cuvette with 40 µL loading volume.

3.2.4 Measurement of photocatalytic activity

To determine the effectiveness of the materials as photocatalysts, their combined effects together, and to see if Au could enable visible light activity with ZnS, experiments were performed under UV and visible light with methylene blue dye indicator. To prepare material for each experiment, three separate but identical synthesis solutions were prepared as described above, combined, centrifuged, and resuspended in 300 µL of deionized water. A UV light was used to excite bandgap transitions in ZnS and a green LED was used to excite plasmon resonance in Au.

To measure activity when ZnS was illuminated with greater-than-bandgap light excitation, first a UV light source was used. Freshly prepared 300 µL solution of spheroid-templated ZnS and/or Au catalyst was prepared with 10 µM of methylene blue (MB, Sigma Aldrich) and left in the dark for one hour to allow solutions to come to adsorption equilibrium.[127] Solution was transferred to UV-transparent polystyrene cuvettes which were placed 1 cm from light source. A UV lamp (Ushio America, Inc) with an isolated 254 nm band was used for excitation, with an average power reaching the sample at 1 cm of 8 µW/cm^2.

To excite plasmonic resonance in Au, a 520 nm LED (Digi-Key) was used as a light source, with 15 mW/cm^2 reaching the sample at 1 cm. To indicate progress of photocatalysis, methylene blue dye was used, in identical conditions as those described above. As a dye-sensitization control, erioglaucine (EG, Fisher Scientific) was used in place of methylene blue, which has an opposite charge in solution, reducing electrostatic binding with catalyst.

Solutions were gently vortexed at 20 min intervals to reduce settling. Temperature was also monitored and recorded every 20 min. Solutions were kept at room temperature (23 ± 2ºC) via air flow supplied by chilled lab air. To measure photocatalytic activity, 50 μL was removed from the solution at regular intervals, centrifuged at 14,000 rpm for 5 min to remove residual catalyst, and measured with UV-Vis. For MB, absorption peak at 665 nm was recorded, and for EG, absorption peak at 625 nm was recorded. Total illumination time was six hours. For each dye, an absorption vs. concentration curve was recorded, to allow concentration versus time plotting. Assuming Langmuir-Hinshelwood first-order kinetics, the natural log of the concentration was plotted against time, which gave the rate constant using the following equation

$$k = {}^{-\ln\left({}^{C}/_{C_0}\right)}\Big/_{t} \qquad (1)$$

For all data sets, measurements were done in triplicate and averaged. As controls, ZnS and Au materials were also synthesized without spheroids and then used in photocatalysis applications, under UV or visible light.

3.3 Results and Discussion

3.3.1 Material synthesis and characterization

The M13 spheroid was used as an asymmetric template for the synthesis of Janus-like, photocatalytic materials. Two protein groups, the p3 and p8, of the phage capsid were modified to display at their N-termini; a ZnS-binding peptide[85] and Au-binding peptide,[34] respectively. In order to utilize the asymmetric orientation of the two protein groups, the spheroidal form of the virus was used to bring the two into close proximity and provide a Janus-like geometry of the template. ZnS and Au were then sequentially synthesized on the template and a schematic of the process is shown in Figure 3.1.

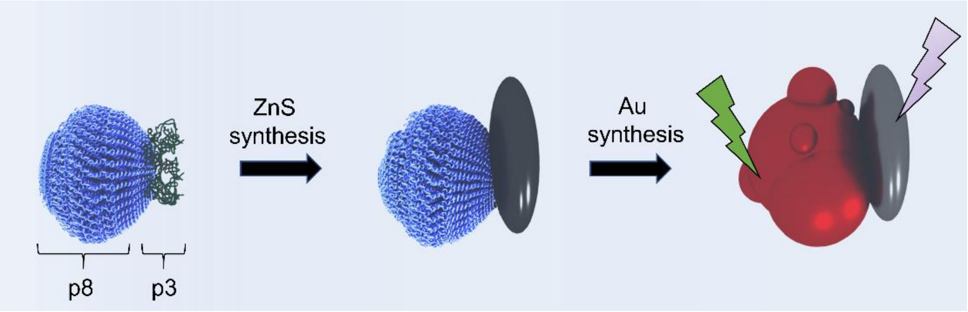

Figure 3.1 *Schematic illustration of ZnS/Au heterojunction assembly on spheroidal M13 template that was then used in either UV or green light driven photocatalysis*

First, materials were synthesized sequentially on the template, with ZnS preceding Au. Using previously adapted conditions,[87,122] 5 nm ZnS were grown. For application in photocatalysis, larger particles are ideal as they have more surface area for reactions to take place. Previous research has shown that changing Zn:S precursor ratio to have a significant impact on particle size,[123,124,128] so this was explored, and results are shown in

Figure 3.2. The data was also compared to results from lower concentrations (5 µM) of both precursors, which yielded smaller particles of about 2 nm in size. It was found that using high Zn:S ratio, 50 µM Zn to 10 µM S, yielded 27 nm particles, while high S:Zn ratio led to very large agglomerates. If 50 µM of Zn and S were used, heavy agglomeration also occurred. The agglomeration from S-rich and high Zn+S solutions is thought to be caused at least partially by charge screening,[123] as well as non-specific growth.[122] The synthesis in Zn-rich solutions indicated that the growth is Zn-limited,[123] but likely leads to a high number of S-vacancies.[124,128]

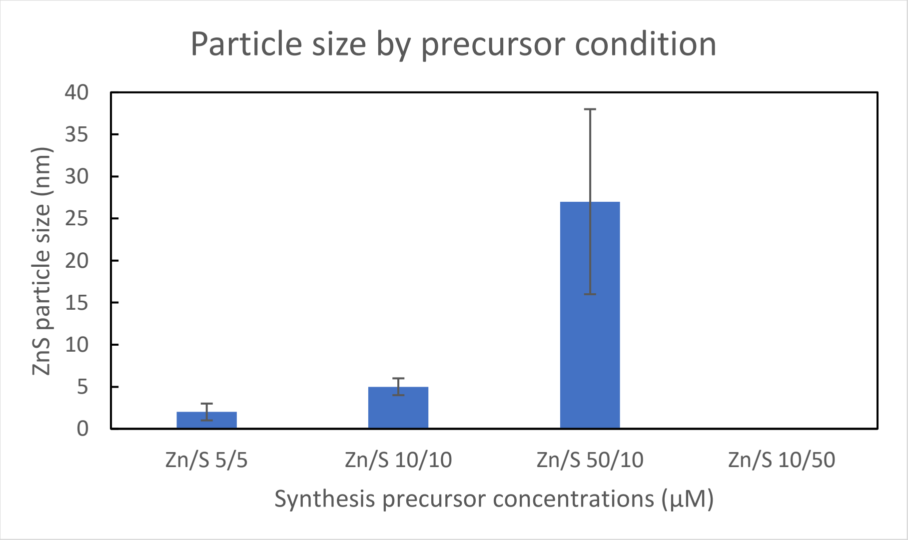

Figure 3.2 *Measured particle size as a function of precursor concentrations. S-rich conditions led to extremely large agglomerates.*

The large ZnS particles given by Zn-rich conditions were selected for further analysis. Figure 3.3a shows TEM of a spheroid with synthesized ZnS particle. Further examples are provided in Figure 3.4a – 3.4c. These particles ranged from spherical to ellipsoidal, with an average aspect ratio of 1.3. Particles had an average size of 27 ± 11 nm. A histogram of the observed particle sizes is provided in Figure 3.4d and shows a wide distribution range. The size distribution was bi-modal in nature, with one peak at ~20 nm and a second, smaller peak at ~40 nm. This was likely due to multiple particles nucleating simultaneously on separate p3 peptides of the same spheroid and then becoming fused together. Spheroid template diameters were observed to expand slightly after synthesis, from 45 ± 13 nm to an average diameter of 70 ± 19 nm, similar to what was seen in previous reports.[122] Following ZnS, Au was then synthesized on the spheroids, and can be seen in Figure 3.3b. Further examples are provided in Figure 3.5a – 3.5c. In general, nearly full coverage of the spheroid template with Au was observed. Particles grew in a dense manner, with rounded morphologies. Following material growth, spheroids with ZnS/Au had an average size of 85 ± 19 nm. This implied a coating of about 15 nm of Au material on the spheroid.

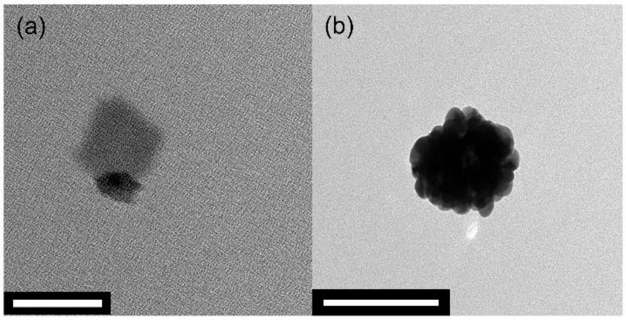

Figure 3.3 *TEM images of (a) ZnS and (b) Au/ZnS nanoparticles synthesized on Au/ZnS-binding spheroid. Samples were not stained. Scale bar: 100 nm*

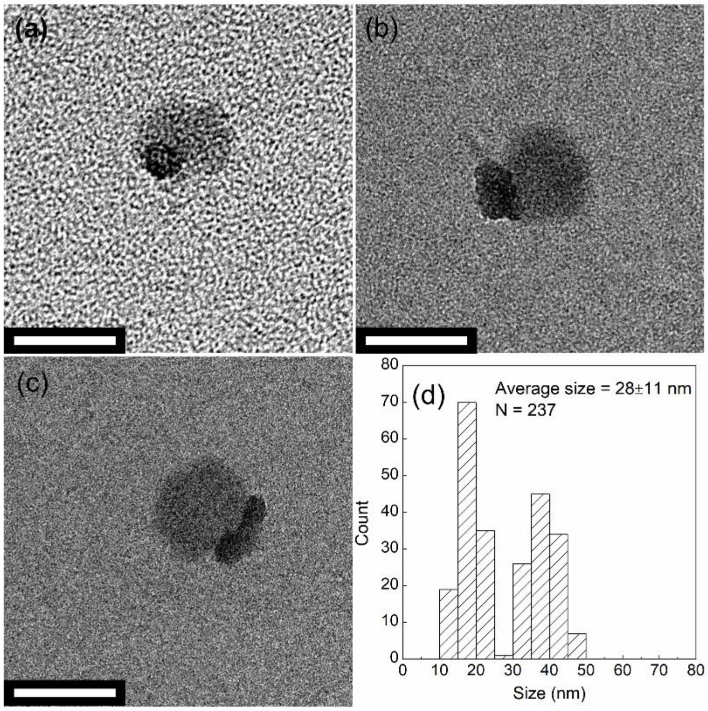

Figure 3.4 *(a - c) TEM images of ZnS synthesis products formed in the presence of Au/ZnS-binding spheroids Synthesized particles were slightly asymmetric with an average aspect ratio of 1.33. (d) Histogram of size distribution of spheroid templated ZnS particles. Of the observed spheroids, 98% displayed synthesized particles, and of those, only 3% had two separate, unfused particles. While uncommon,*[122] *it has been shown to occur that multiple p3 proteins on a single template may initiate nucleation of ZnS.*[85] *Samples were not stained. Scale: 100 nm*

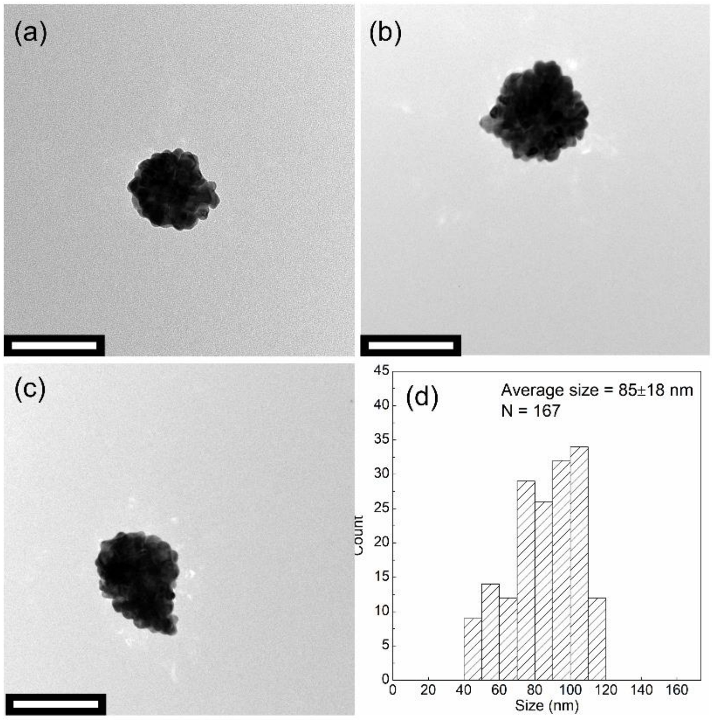

Figure 3.5 *(a -c) TEM images of Au/ZnS nano-heteroparticles formed in the presence of Au/ZnS-binding spheroids (d) Covered particles displayed somewhat asymmetric growth with an average aspect ratio of 1.25. Histogram of spheroid particle size after Au/ZnS synthesis. Scale Bar: 100 nm*

Crystal structure of each of the material combinations was characterized with ED. Due to the low mass of material in a single particle, solutions of particles were concentrated via centrifugation into large agglomerates for analysis. TEMs of the concentrated ZnS and ZnS/Au material is shown in Figure 3.6a and 3.6b, respectively. Diffraction patterns for ZnS and ZnS/Au are shown in Figure 3.6c and Figure 3.6d, respectively. For ZnS, a mixture of zinc-blende and wurtzite crystal phases was observed, identical to previous reports of ZnS synthesized on the peptide.[122] For the ZnS/Au sample, the pattern for ZnS was observed, as well as multiple lattice spacings attributable to face-centered cubic Au. Table 3.1 shows the measured d-spacings for each sample, along with their attributed crystal plane.

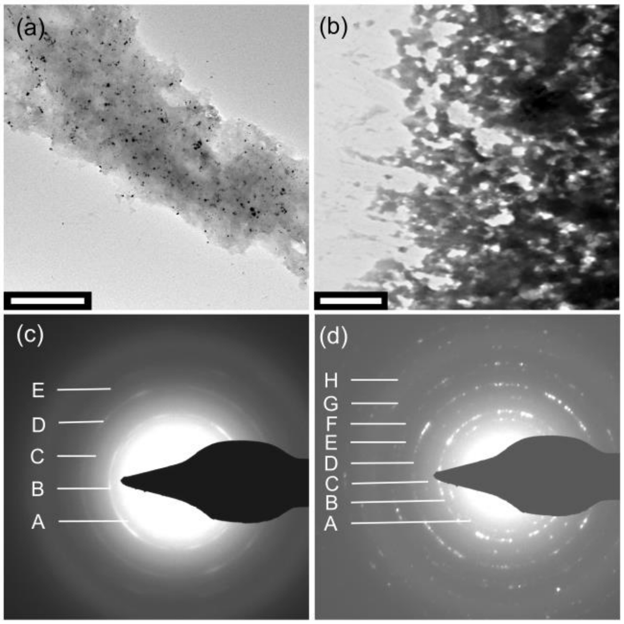

Figure 3.6 *TEM image of concentrated (a) ZnS and (b) Au/ZnS material synthesized on spheroids. Corresponding selected area electron diffraction of (c) ZnS and (d) ZnS/Au. Measured lattice spacings are labeled for reference in Table 3.1. Scale bar: 500 nm*

Table 3.1 *Measured d-spacings from Figure 3.6 along with their nearest matching crystal plane*

Measured d-spacing (Å)		Zinc-blende ZnS	Wurtzite ZnS	Cubic Au
ZnS				
A	3.13	(111)	(002)	
B	2.91		(101)	
C	2.24		(102)	
D	1.94	(220)	(110)	
E	1.59	(222)	(201)	
Au/ZnS				
A	3.30		(100)	
B	2.73	(200)		
C	2.34			(111)
D	2.05			(200)
E	1.95	(220)	(110)	
F	1.66	(311)	(200)	
G	1.60	(222)	(201)	
H	1.39	(400)	(104)	(220)

To restrict the interface between Au and ZnS, 5 nm AuNPs were bound to spheroids following ZnS synthesis in place of synthesizing Au. This was done to reduce the interfacial area between the ZnS and Au, thereby reducing the charge transfer efficiency between the two materials and helping to elucidate the effects of the heterojunction on the photocatalytic process. A TEM image of spheroids with ZnS and AuNP is shown in Figure 3.7, which had an average number of 29 ± 20 particles bound on each spheroid.

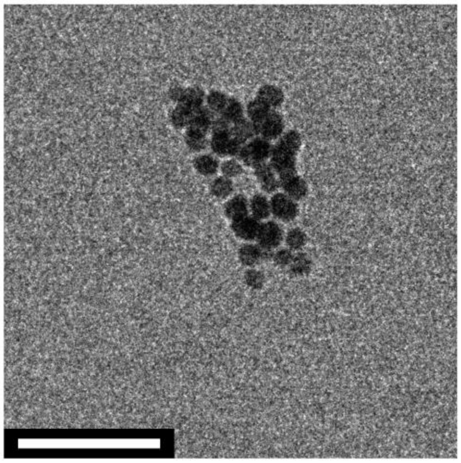

Figure 3.7 *TEM image of Au/ZnS-binding spheroid after ZnS synthesis and binding 5 nm Au nanoparticles. Scale: 25 nm*

UV-Visible light absorption and photoluminescence (PL) spectroscopy were used to characterize the optical properties of ZnS and ZnS synthesized on the spheroid. Absorption from the viral template showed a small peak at 261 nm. This is slightly shifted from typical absorption at 269 nm, and is due to the higher Rayleigh scattering of the spheroid over filamentous form of the phage.[4] The ZnS absorbed at 253 nm, with a steep decrease and no absorption with increasing wavelengths, and is shown in Figure 3.8a. This short wavelength was likely due to band edge transitions that were significantly blue-shifted by quantum confinement effects.[39,129] Size estimations by Brus equation[130] correlate with ~1.5-4 nm particles,[39] much smaller than the particles measured through TEM observations. This is indicative of the highly polycrystalline nature of the ZnS material. Synthesized Au absorbed over a broad range of UV and visible wavelengths. In the visible to near-IR, the Au showed absorption at wavelengths ranging from 520 to beyond 950 nm. This is similar to previous reports and arises due to the polycrystalline, uneven structure of the Au.[131,132] Strong UV light extinction by Au is due to the absorption by d-band transitions of the metal,[133] Rayleigh scattering from nanoparticles,[134,135] and absorption from the ZnS.

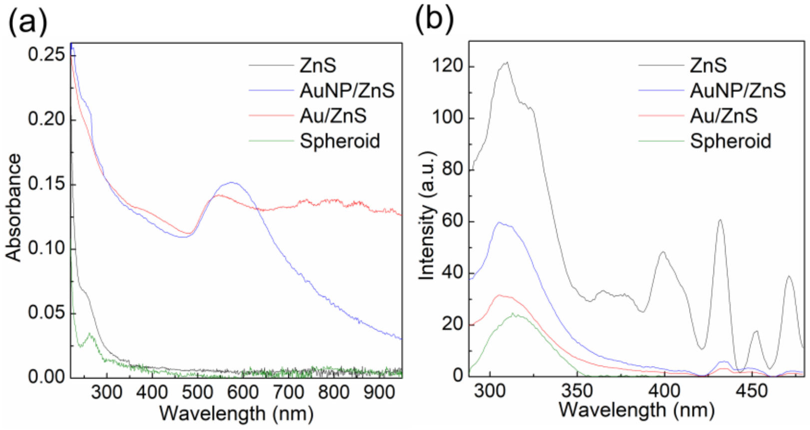

Figure 3.8 *(a) Absorbance and (b) photoluminescence spectra of spheroid as well as ZnS, ZnS/Au, and ZnS/AuNP on spheroid template.*

In contrast, the bound AuNPs had a plasmon peak centered at 571 nm. This showed a distinct red-shift from that of pure AuNP's, which have an absorption peak near 520 nm. The shift was likely due to the higher index of the bound phage and ZnS, as well as strong interparticle coupling.[4,132,134,136] The addition of Au led to a high absorption of visible light, which was not observed by ZnS alone.

Photoluminescence of the materials is shown in Figure 3.8b. ZnS synthesized on the spheroid showed a large peak at 305 nm, due to band edge transitions, and at 314 nm attributable to the virus template. Four longer wavelength peaks at 400, 433, 455, and 492 nm were also observed, and can be attributed to a combination of surface and defect states.[54,56,137] Photoluminescence was seen to be reduced with the addition of AuNPs, which is likely due to a combination of Rayleigh scattering, absorption by d-band transitions in Au, and some quenching of the surface, defect, and conduction band states.[54,138,139] ZnS photoluminescence was further lowered in the presence of synthesized Au than bound Au, possibly indicating stronger quenching effects arising from higher contact between ZnS and Au.[54] Au growth may also increase scattering, and therefore decrease light absorption by ZnS.

3.3.2 Photocatalysis

The photocatalytic capability of the ZnS/Au nanoparticles were initially investigated under UV illumination. Each material was investigated individually and together to determine if Au could enhance ZnS photocatalysis. Photocatalytic activity was studied via degradation of Methylene blue (MB) dye.

Methylene blue breakdown, using each material synthesized on spheroids, is shown in Figure 3.9. A UV source of 254 nm was used in order to excite bandgap-energy electrons for photocatalysis, and its spectra is shown in Figure 3.10. The activity of spheroids, light source, as well as ZnS, Au, and Au/ZnS synthesized without the template, were done as controls and are shown in Figure 3.11. An average of 5% of dye signal was lost in the one hour before illumination, due to adsorption. Overall, spheroid-synthesized and bound Au displayed comparable photocatalytic activity to the light source alone, or rather, degradation by photolysis from UV light, indicating minimal activity from the metal. ZnS synthesized on the spheroid degraded 82% of the dye, while 97% was degraded when synthesized ZnS/Au by spheroids. Photographs of MB solutions with Au/ZnS on spheroids compared with pure dye solution, before and after UV illumination, are shown in Figure 3.12a and Figure 3.12b, respectively. This increase in activity in comparison over individual ZnS cannot be attributed to isolated Au material. Instead, this indicates a significant enhancement by the combined ZnS/Au material. Interestingly, AuNP paired with ZnS via binding to spheroids also showed higher activity than with ZnS alone. More efficient degradation with synthesized material suggests higher contact area with ZnS, thus more efficient charge transfer.[17,140,141] This is further reinforced by the negligible degradation results from synthesized Au alone.

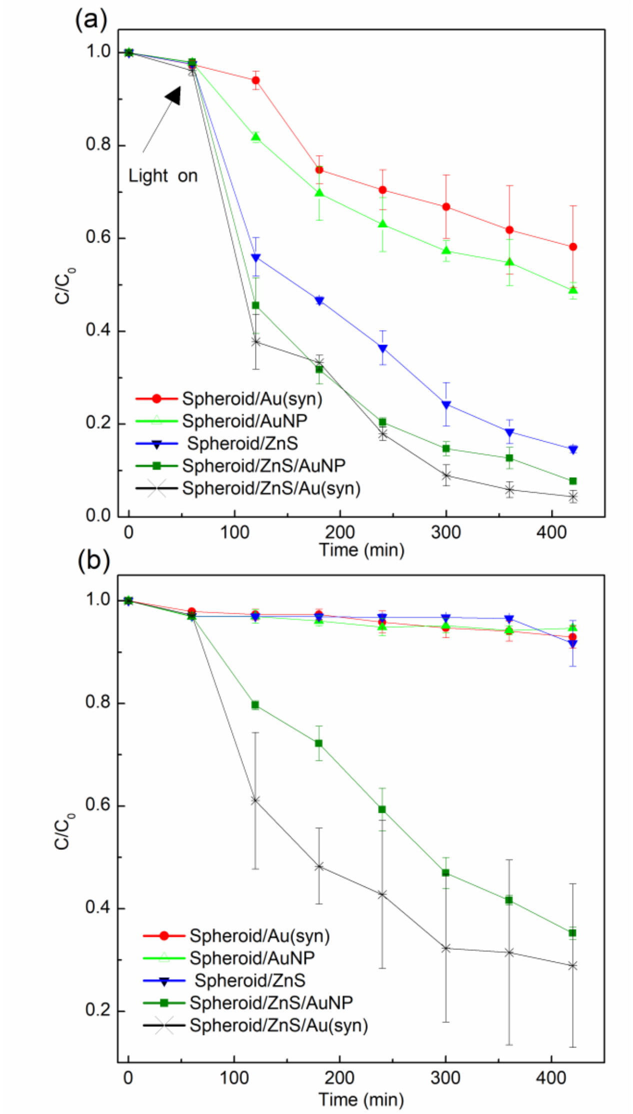

Figure 3.9 *Methylene blue concentration degradation by photocatalysis over six hours using (a) UV and (b) green light with spheroid-templated ZnS and Au/ZnS materials. Light source was switched on at 60 minutes.*

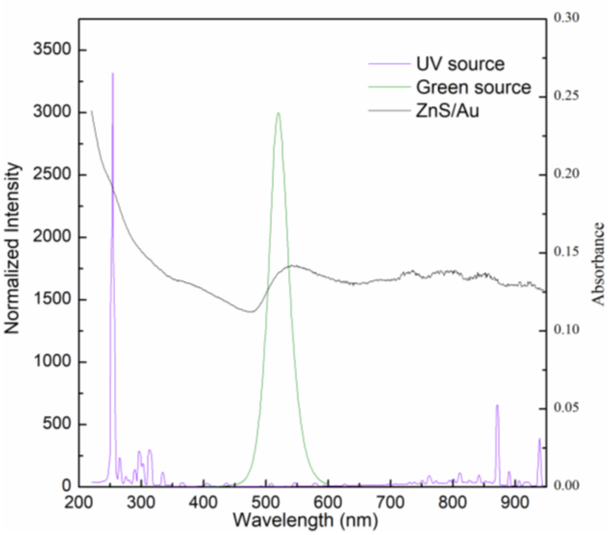

Figure 3.10 *Emission spectra of UV and green LED light sources used in photocatalysis experiments. Absorption of spheroid templated ZnS/Au is overlaid for comparison.*

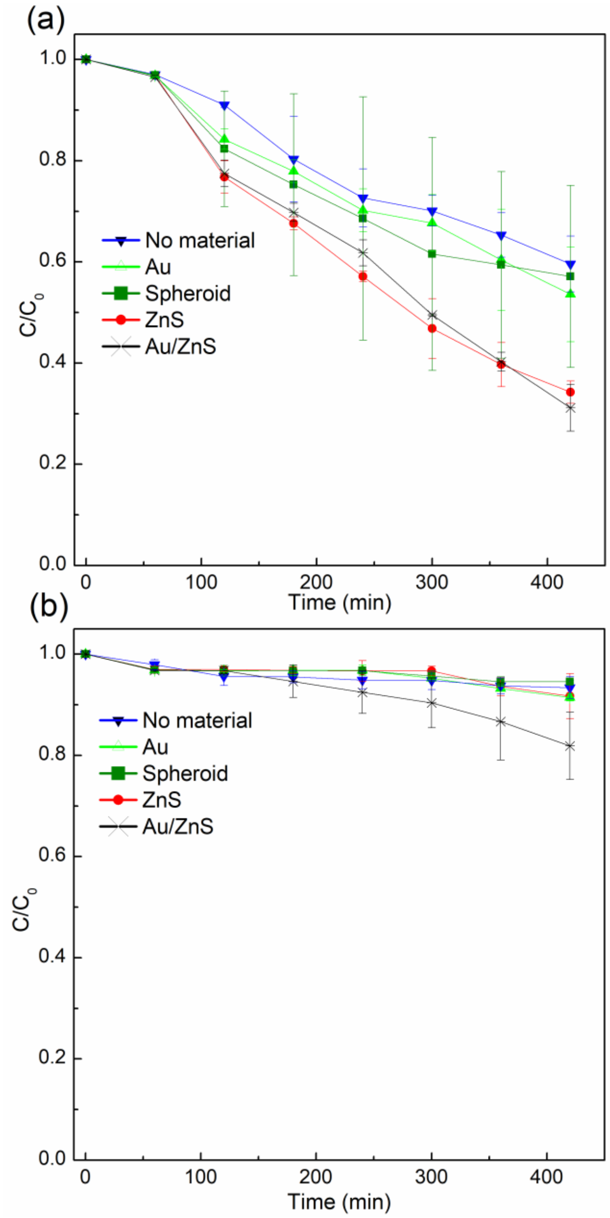

Figure 3.11 *Methylene blue degradation by spheroid template, synthesized Au without template, ZnS without template, Au/ZnS without template, and without any materials under (a) UV and (b) green light. All samples showed some degradation under UV, but relatively no activity under green light. For each sample, light source was turned on at 60 minutes. ZnS and ZnS/Au synthesized without templates did not show as much activity as the material with templates. Similarly, non-templated ZnS degraded substantially lower amount of dye than templated ZnS under UV. This may be due to higher crystallinity of the material grown on the template. No dye was degraded with any material alone with green light illumination. However, some activity was observed with ZnS/Au synthesized sequentially without spheroids under green light, suggesting contact between ZnS and Au, likely due to some heterogeneous nucleation. These controls communicated the overall contribution of the template on assembly, and its impact on the materials' photocatalytic activity. This suggests that the spheroid template is essential in growing material, as well as bringing them into contact for a good interface.*

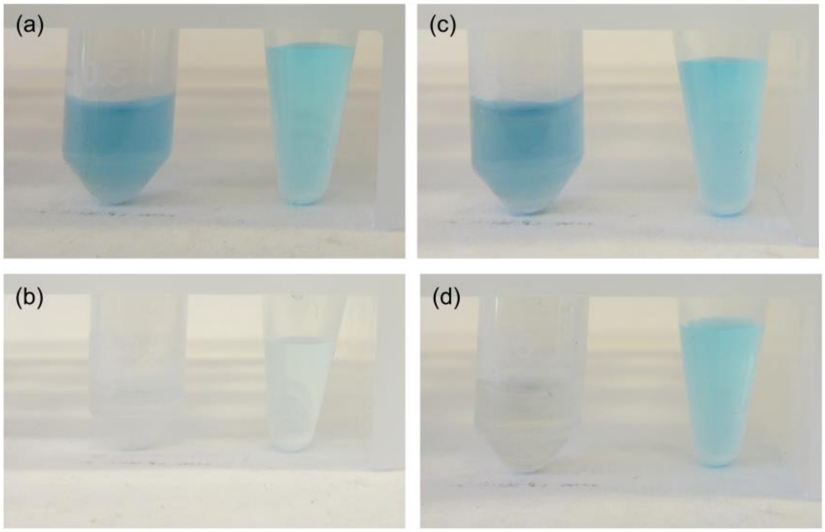

Figure 3.12 *Photographs of MB solutions before (top row) and after (bottom row) six hour light exposure. Samples done with UV (left column) and green light (right column) exposure. In each image, left tubes contain dye with ZnS/Au synthesized on spheroids while right tubes contain only dye. In the presence of catalyst, most of MB was degraded. Without catalyst, dye was still significantly degraded by UV light, but largely unaffected by green light exposure.*

To further investigate the Au and ZnS interaction, green light was used as an excitation source. This was done to show whether Au plasmon resonance could sensitize ZnS to visible light, an otherwise UV-absorbing material. For this purpose, a 520 nm light source was used as an excitation source. Methylene blue degradation results for materials synthesized on the spheroid are shown in Figure 3.9, and the emission spectrum of the green light source is shown in Figure 3.10. Activity by all materials synthesized without the spheroid, as well as spheroid and light source alone, are in shown in Figure 3.11.

As with UV experiments, an average of 4% of dye was lost in the 60 minutes prior to light illumination in all samples. Illumination of pure dye solution did not lead to observable dye degradation, indicating that zeroth order photolysis reactions could be neglected. Interestingly, samples with only ZnS or Au synthesized on the spheroid did not measurably degrade any dye under green light. Photocatalytic activity was not expected for ZnS alone, as it shows negligible absorption at wavelengths near 520 nm. Nor was it expected from Au, as plasmonic resonance on its own has not been shown to appreciably degrade dye, since free charges are not created.[142,143] However, ZnS/Au synthesized on spheroids did show photocatalytic activity, and an average of 72% of dye was degraded over six hours. Since Au alone did not show any dye degradation, this was strong evidence of charge separation by hot electron injection from Au to ZnS when plasmon resonance was excited.[116,144]

Photographs of MB solutions with ZnS/Au on spheroids and without material are shown before illumination in Figure 3.12c and after in Figure 3.12d.When compared to ZnS/AuNP on spheroids, which degraded an average of 67% of the dye, a trend was seen with UV and green illumination results that indicated higher activity of ZnS with synthesized Au over bound AuNP. The green light illumination data, like the UV results, suggested that the larger material interface allowed more efficient charge separation and thus longer lifetimes, a major factor in photocatalytic reactions. But in both cases, the assembly of Au and ZnS together using the spheroid template, was successful in the generation of visible light photocatalytic degradation of dye.

Photocatalytic rates for all samples were calculated assuming Langmuir-Hinshelwood kinetics. Rates for spheroid-templated samples under UV and green light illumination are shown in Figure 3.13. The rates for all controls are shown in Figure 3.14.

Under UV, spheroid templated ZnS/Au had the highest average k-rate of $8.5 \cdot 10^{-3}$ min^{-1}, which was larger than the sum of its constituent ZnS ($5.1 \cdot 10^{-3}$ min^{-1}) and Au ($1.5 \cdot 10^{-3}$ min^{-1}) materials, and gave an enhancement factor of 1.66. The observed enhancement factor helps to show that Au and ZnS are both accessible to the dye solution, as it is expected that rates would decrease if Au had grown over ZnS surfaces, thereby blocking photoexcited charges from reaching the environment.[44] It also suggests the presence of a Schottky barrier at the interface rather than an Ohmic junction, as the electric field produced by the Schottky barrier helps separate the electron-hole pairs near the material interface.[19,145] A proposed schematic is shown in Figure 3.15. The spheroid templated ZnS with bound AuNP had an average k-rate of $7.1 \cdot 10^{-3}$ min^{-1}, giving an enhancement factor of 1.39. The enhancement factor is lower for the bound AuNP when compared with the synthesized Au. This difference in enhancements provided further evidence of increased charge transfer efficiency with synthesized Au, thanks to the increase in interfacial area. This correlated with observations seen in photoluminescence measurements. The difference in photoluminescence between bound and synthesized Au is consistent with the proposed mechanism, since photoexcited electrons will be more likely to lose energy via non-radiative emission in Au before recombining with holes left in ZnS.[146,147]

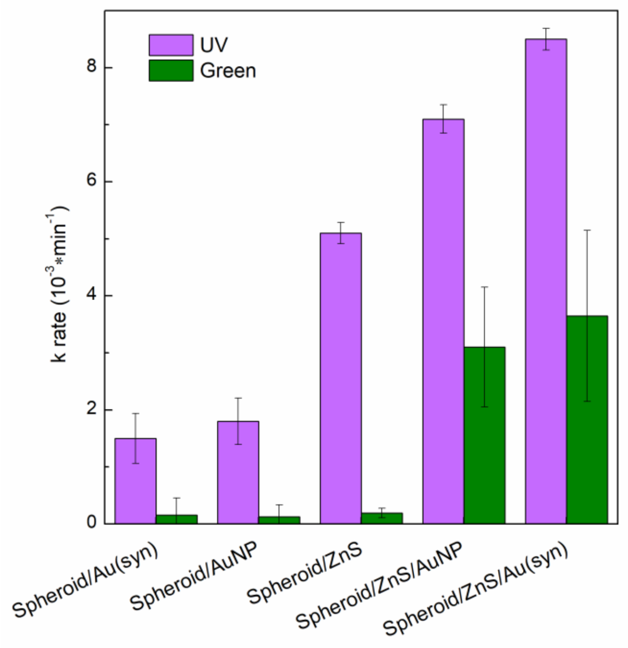

Figure 3.13 *Calculated photocatalytic rates assuming Langmuir-Hinshelwood kinetics for spheroid templated ZnS, Au, AuNP, AuNP/ZnS and Au/ZnS under UV and green light illumination.*

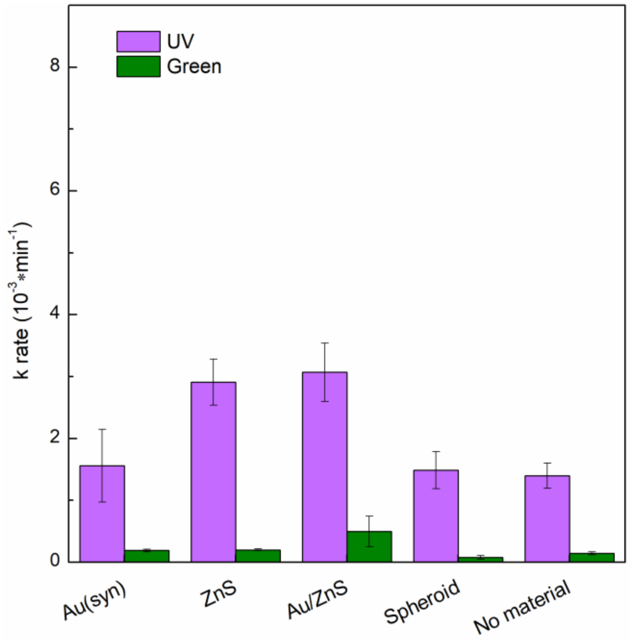

Figure 3.14 *Photocatalytic rates of spheroid template, synthesized Au without template, ZnS without template, Au/ZnS without template, and without any materials used as controls under UV and green light. Under UV illumination, methylene blue (MB) degradation with no material occurred by photolysis, and had a similar rate to spheroids and non-templated Au. Non-templated ZnS showed a somewhat higher rate, but this was not improved by synthesized Au, indicating that the spheroid template is required to assemble the materials together. Under green light, MB did not photolyse, and was only degraded marginally with the non-templated Au/ZnS sample.*

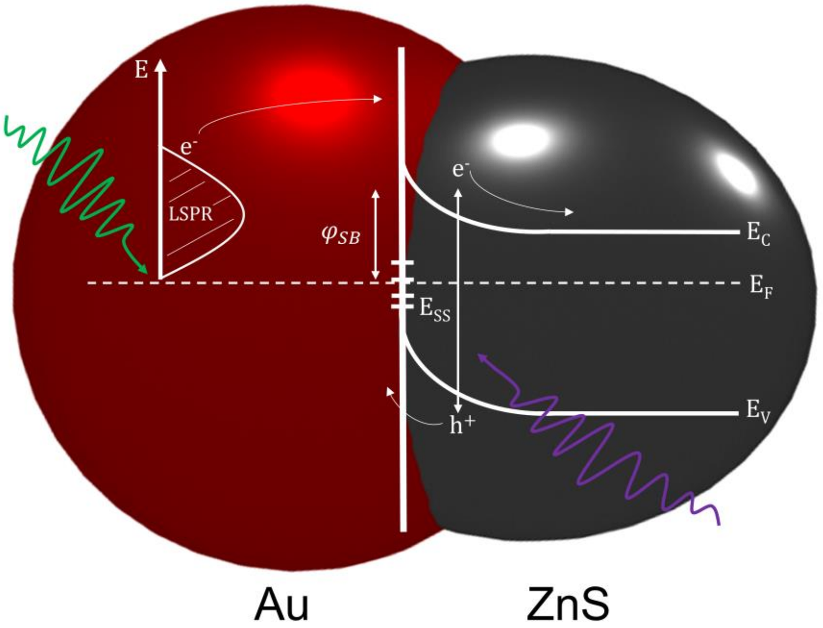

Figure 3.15 *Schematic representation of the two excitation processes occurring in ZnS/Au nanoparticles. Likely, Fermi level pinning in ZnS allows the generation of a Schottky barrier to occur at the surface. In this case, the Schottky may be calculated with the equation* $\varphi_{SB} = E_G - E_{SS}$ *as it no longer depends strongly on the work function of the metal. UV light absorbed by the ZnS excites electrons into the conduction band which are able to transfer to the Au nanoparticle. Alternatively, green light absorbed by the Au excites plasmonic electrons, some of which are high enough energy to be injected into ZnS.*

The proposed mechanisms were further reinforced by the dye degradation rates under green light, which were significant only for samples containing both Au and ZnS. The average rate of spheroid-templated ZnS/Au was marginally higher than ZnS/AuNP. For ZnS/Au and ZnS/AuNP, k-rates were 3.65 and $3.1\cdot10^{-3}$ min^{-1}, respectively, which are proportional with their rates from UV photocatalysis. Hot electrons excited with 520 nm light will have energy ~2.4 eV above the Fermi level in Au. It was shown experimentally that the maximum energy of the ZnS and Au Schottky barrier was 2.2 eV.[57] However, ZnS has a high concentration of surface states, and Fermi level pinning likely plays a role.[57,148,149] In this case, the barrier height can be estimated by the equation[150]

$$\varphi_{SB} = E_G - E_{SS} \qquad (2)$$

Using a value of 4.06 eV[130] for ZnS E_G (bandgap) and 2.88 eV[56] for E_{SS} (surface state) gives a barrier energy of 1.30 eV, meaning that a significant fraction of plasmonic electrons would have sufficiently high energy to overcome the barrier.[71,151]

To further elucidate the effect of the ZnS particle size on photocatalytic activity, the k-rate was measured for each of the particles shown in Figure 3.2. Rates are shown in Figure 3.16. A general correlation between particle size and photocatalytic rate was observed for the ZnS particles under UV illumination. An exception is with the large >1 μm agglomerates grown in S-rich conditions. It is likely that the reactive surface area becomes restricted by the small numbers of agglomerates. As many of the small particles are bound up within the volume of the agglomerate, they are not available for photocatalysis as they don’t have access to the environment.

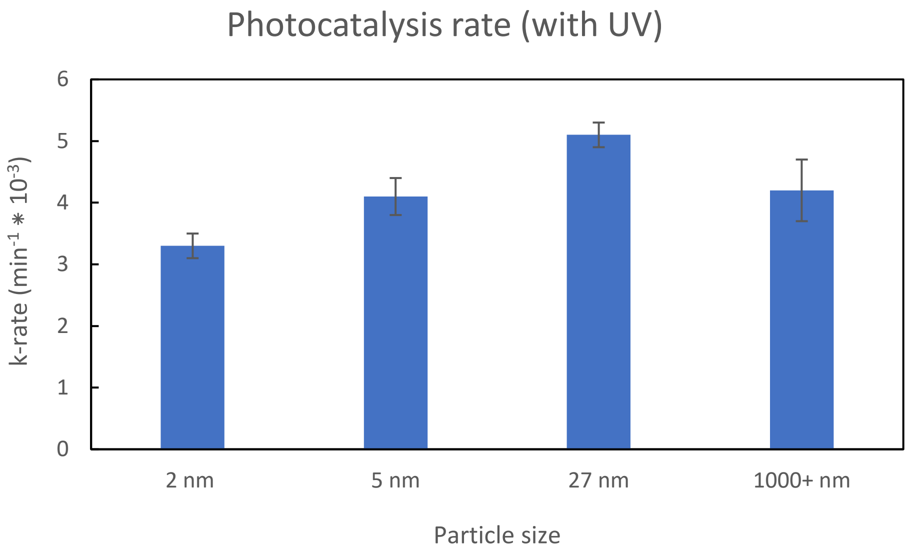

Figure 3.16 *Photocatalytic k-rates measured with different ZnS particle sizes under UV illumination..*

An additional control was used, in order to check for methylene blue degradation via dye sensitization. A different dye, erioglaucine, was used as it is electrostatically repelled from ZnS, and does not absorb at 520 nm, which will mitigate direct charge transfer from dye to catalyst. This data is show in Figure 3.17. This dye was chosen for its minimal absorption at 520 nm and negative charge at pH 7.5,[152] electrostatically repelling it from negatively charged ZnS/Au.[153] For dye sensitization to occur, dye must be photoexcited, and also have physical contact with a material which can accept the excited electron. EG dye was successfully degraded, which showed that dye sensitization may be ruled out. These results show that the M13 spheroid template is capable of directing synthesis of a Au/ZnS heterostructure with UV and visible light photocatalytic activity. Further, it shows that the charge separation capabilities of the Schottky junction have a dependence on the interfacial contact between the two materials, and these capabilities are improved with synthesized materials over bound ones.

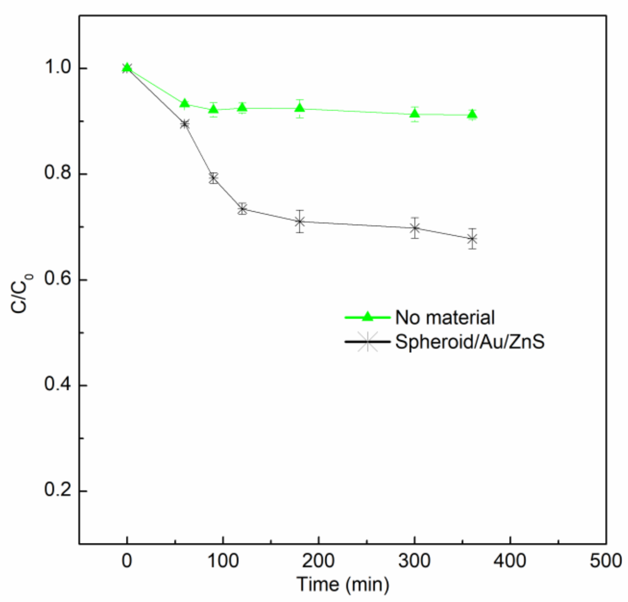

Figure 3.18 *Concentration of negatively charged erioglaucine (EG) dye over six hours under green light illumination. Compared solutions with spheroid/ZnS/Au photocatalyst and solution containing only dye. Light source was switched on 60 minutes. Negatively charged dye was chosen to mitigate electrostatic attraction with Au/ZnS material, both of which have a negative charge at pH 7.5. EG also absorbs minimal at 520 nm, so will not be in an excited state. Solution containing only dye did not show any measurable degradation, whereas 23% reduction in dye occurred with illumination in the presence of Au/ZnS on spheroids. Since direct contact between dye and catalyst was mitigated in this experiment, and dye is not absorbing, the dye sensitization reaction can be ruled out.*

3.4 Conclusion

In summary, we investigated the Au/ZnS heterojunction produced by the bi-functional M13 spheroid. This work expanded on previous studies by increasing the size and density of synthesized materials but preserving the asymmetric orientation and applying the nanoparticles in photocatalytic dye degradation. When Au was added to ZnS, its photocatalytic capabilities were significantly enhanced. Under UV, dye degradation occurred at a much higher rate than when either material was alone. Under green light, photocatalysis only occurred when Au was added to ZnS. Here, no evidence of dye degradation was observed by the materials alone. This provided strong evidence that a Schottky barrier occurred at the ZnS/Au interface, which helped to separate the electron/hole pairs. It is also possible that hot electrons, excited by localized surface plasmons in Au, were be injected into ZnS. Further work is needed on improving on the size of the ZnS nanoaprticles, as it is suspected that photocatalytic activity is limited by the particle size. Making use of the efficient catalyst ZnS under visible light is an important achievement in photocatalysis, and implementing M13 in catalytic nanoparticle solutions marks a turning point in their applications.

Chapter 4. Exchanging protein targets for material synthesis for increased ZnS coverage and Au binding

4.1 Introduction

Semiconductor photocatalysts absorb sunlight and use the energy to accelerate chemical reactions. With many potential applications, a large body of research focuses on water remediation.[11] Many of the more effective semiconductor photocatalysts are UV-absorbing semiconductors,[12] but require addition components, such as a metal nanoparticle, to 'sensitize' the semiconductor to visible light. While orientation, morphology, and size of the two materials has been shown to have significant effects on the photocatalytic efficiency, reactive surface area is also a major factor. When assembling semiconductor/metal materials on a spheroid, the material surface area can be limited by the available area for synthesis on the protein coat. By assembling multiple spheroids into one structure, hierarchical nanostructures can be created. These would allow control of exposed material surface area, as well as light absorption characteristics, therefore granting adaptability to different photocatalytic conditions.[95]

In assembling these complex structures, the same issues are seen as with the assembly of asymmetric Janus particles. Common methods of assembly like block copolymers lack specificity.[73] And epitaxial growth methods often suffer from low yields.[154] These methods rely on either basic heterogeneous nucleation or targeted growth at liquid-liquid interfaces, both of which are limited to lattice matching of materials.[155] Phase interfacial growth further limits the number of new particles to those that can fit at the interface. Scaling up for commercial photocatalytic applications using these methods will be challenging.

A simple, yet versatile method of assembling these structures lies in the M13. Due to its native bifunctionality, it can be made to assemble two-part subunits. One commonly used genetic variant of the M13 displays on the N-terminus of its p8 protein three negatively charged glutamate residues, usually called E3 phage. This high negative charge allows electrostatic interactions with a wide variety of metal ions, including Pd,[156] Au,[34] Cu,[157] and Zn.[158] Previous work by Belcheret al, even used the phage to nucleate and grow ZnS over the main body of the virus for sulfide battery cathodes.[158] To make the phage bifunctional, it can be chemically functionalized for an affinity to Au. Separate work focused on the p3 protein has shown that it can be chemically modified to bind Au particles, without any genetic modifications.[118] This process relies on chemical reduction of the disulfide bonds found between pairs of cysteine residues in the minor coat proteins. All told, there are eight within the p3, and one each in the p7, p9, and p6, giving 55 in each phage, since there are 5 copies of each minor coat protein. When reduced, the S-bonds are freed up to bind AuNP through strong Au-S bonds. This work also showed that by controlling mixing ratios of phage and AuNP, ratios of bound phage:AuNP could also be controlled. Work by Montalvan-Sorrosa et al. successfully reduced the p3 using a simple sodium borohydride approach in tris-buffered saline, showing that the method could work in different buffers and with different reducing agents.

In the following chapter, the E3 phage without a genetic modification to the p3, was treated with a reducing agent to free the 8 native Cysteine bonds in each of its p3 proteins. Using Ellman's reagent, the efficiency of the reduction process was calculated by the concentration of free Cysteine residues. The reduced filaments were then interacted with AuNP that had varied concentrations of BSA capping agent to achieve increasing ratios of bound phage per AuNP. These assemblies were interacted with chloroform, producing spheroid/AuNP structures. While keeping the concentration of phage and AuNP constant, the different particle assemblies were characterized via TEM for numbers of phage per AuNP. E3 spheroids were also shown to synthesize ZnS across most of the surface of the p8 coat. The material was characterized for its optical bandgap with UV-vis absorption, and its morphology with TEM. By using a moderately sized Au nanoparticle, the p3 of this E3 phage can be used as the binding site and Au/ZnS asymmetric particles can be formed with the E3's spheroid form. Through control of spheroid-to-AuNP ratios, increasing numbers of spheroids can be bound around the Au 'core', to create increasingly complex hierarchical nanostructures. By first binding spheroids and AuNPs, then growing ZnS and illuminating with above-bandgap light, the AuNP can be used as electron 'sink', allowing the ZnS to act as a light capturing satellite. With sufficiently separated electron-hole pairs, potentially large increases in the photocatalytic efficiency can be attained over what was shown previously.[95] Whave shown that by increasing the size of the ZnS particle, enhancements can be made to the photocatalytic activity, presumably due to the increased surface area for reactions to take place. However, further increases to the ZnS material were limited by the small number of nucleation sites that were located at the M13’s 5 p3 proteins. Since the phage contains 2700 p8 proteins, that protein makes a much more attractive target for ZnS growth. These particles show potential in creating higher complexity structures, with changing numbers of ‘satellite’ spheroids to AuNP ‘cores’. When combined, these Au/ZnS materials have great potential as wide spectrum photocatalysts with the addition of a semiconductor material, and could easily be applied in the degradation of many antibiotics.

4.2 Experimental details

4.2.1 Au nanoparticle binding

Phage were chemically treated to free S-bonds for Au nanoparticle (AuNP) binding. A 100 μL filamentous EEE-phage (E3, 10^8 pfu/μL) in tris-buffered saline (TBS, 50 mM Tris–HCl, 150 mM NaCl, pH 7.5) was mixed with 1 μL of 500 mM sodium borohydride ($NaBH_4$, Fisher Scientific) and incubated for 30 minutes at 37°C in order to reduce and break the disulfide bonds between each of the three pairs of cysteine residues in each p3 protein.[159] Then, 400 μL of deionized water was added to dilute and deactivate the reducing agent, and the entire solution was centrifuged at 5k rcf for 15 minutes through an Amicon Ultra 3kDa molecular weight cutoff filter (Sigma Aldrich), until 50 μL remained, to remove remaining $NaBH_4$. This process was repeated once, then the sample was resuspended in 100 μL of deionized water. Separately, an equal volume of citrate-coated, 50 nm gold nanoparticles ($5.4*10^6$ NP/µL, Ted Pella, Inc) were interacted with 0, 1, 5, 10, 12, 20, or 50 µg/mL BSA for 30 min, for stabilization in TBS solutions. The AuNP and filament solutions were combined and allowed to incubate for 6 h at 37°C for binding. Following binding, 100 µL of phage/AuNP solution was used for transformation.

4.2.2 M13 spheroid preparation

Filamentous phage, either bound to AuNP or in preparation for ZnS synthesis, were converted to spheroid form. The E3 phage that was used displayed a negatively charged, triple glutamate peptide on its p8 at the N-terminus. Either following binding or prior to ZnS synthesis, the filamentous phage was treated with chloroform to transform to spheroid.[2,4] In either case, 100 µL phage solutions (10^8 pfu/µL) in TBS, and 100 µL of amylene-stabilized chloroform (99.8%, ACROS Organics) was prepared. Phage and chloroform solutions were chilled at 0°C for 20 s, combined, then vortexed at 0°C. The mixture was vortexed at high power for one vortex/rest cycle, followed by two additional vortex/rest cycles at low power. Following the third vortex/rest cycle, samples were quickly warmed in a 37°C water bath for 20 s. Two additional vortex/rest cycles were completed at room temperature, both at low power. After mixing, approximately 85 µL of chloroform was withdrawn with a pipette. The remaining chloroform was removed by gently flowing air over the sample. Templates were stored at 4°C until use.

4.2.3 ZnS synthesis

Spheroids were then used in the synthesis of ZnS as part of the preparation of a ZnS/Au heterojunction nanoparticle. Synthesis procedure for ZnS was adapted from previously reported methods, and the ZnS process was modified to yield growth over the entire spheroid. To synthesize ZnS on the p8 protein, 400 μL of deionized water was added to freshly made spherical phage in 100 μL of TBS (10^8 pfu/μL). To prepare a 100 μM solution of zinc chloride ($ZnCl_2$, Sigma Aldrich) with the spheroids, 1 μL of 50 mM $ZnCl_2$ was added and then gently vortexed. The solution was stored at 4°C for 3 h. An equal volume of 60 μM sodium sulfide (Na_2S, Sigma Aldrich) was prepared in deionized water. Both solutions were placed on ice, following which, the Na_2S solution was added dropwise in 10 μL increments to the $ZnCl_2$ and phage solution over the course of an hour. The entire solution was then incubated at room temperature for an additional 6 h to produce ZnS particles on the p8 protein.[85] In preparation for centrifugation and subsequent removal of synthesis precursors, ZnS products were mixed with Tween-20 to achieve a concentration of 0.1% weight byvolume, in order to prevent agglomeration of particles. The solution was centrifuged (200 rcf, 15 min), supernatant removed, then particles were resuspended in deionized water. Finally, they were vortexed, then sonicated for 15 min to fully resuspend in solution. Samples were immediately prepared for TEM or spectroscopic measurements.

4.2.4 Material characterization

Transmission electron microscopy (TEM, Tecnai T12) was used to study viral template geometry and size, as well as the morphology, size, site-specific growth, and overall viral template coverage of ZnS synthesis and Au binding products. To prepare TEM samples for imaging and diffraction, a 5 μL volume of solution was added to a formvar/carbon-coated copper grid (Ted Pella, Inc), incubated 5 minutes, and washed twice with deionized water. Viral template samples without ZnS or Au were stained with 2% uranyl acetate for 30 s, then wicked dry. ImageJ[126] was used to measure template and synthesis product size and aspect ratio. Images with minimum magnification of 11,000x was used. For all measurements, a sample size of at least 150 was used for each.

Absorption of spheroidal template and inorganic materials were measured from 220 to 950 nm using a UV-Vis spectrophotometer (Evolution 60, Thermo Scientific). All samples were measured in solution using a 1 cm pathlength quartz crystal cuvette (Starna), using deionized water as a baseline correction. To measure the concentration of free thiol bonds following $NaBH_4$ reduction of the p3, Ellmans reagent (ThermoFisher, Inc) was added to the solution. To measure the concentration, the characteristic absorption peak at 412 nm was measured and converted to a concentration using a previously made calibration curve. Tauc's method was used to estimate the ZnS bandgap.[160] Using the Tauc relation

$$(\alpha h\nu)^n = B(h\nu - E_G)$$

And setting n=2, since ZnS is direct bandgap, the energy of the transition can be extrapolated by fitting the linear region of the data to the x-axis.

To produce the calibration curve, solutions of Ellman's reagent (4 mg/mL) were interacted with solutions of varying concentrations (0, 0.5, 1, 2, 4, and 10 μM) of L-

Cysteine HCl (ThermoFisher, Inc), incubated for 20 minutes, then measured for absorption at 412 nm. To calculate the total number of cysteine residues available in solution, accurate phage concentrations were first calculated by subtracting Rayleigh scattering contributions.[161] This concentration was then multiplied by the total number of cysteine residues within each phage to give a concentration of cysteine in solution. The number of cysteine per phage was calculated by adding the single cysteine in each p6, p7, and p9 to the eight in the p3, and multiplying by five, the number of these proteins in each virus, to give a total of 55 cysteine per phage.

4.3 Results and Discussion

4.3.1 Cysteine Reduction and Phage to Au nanoparticle binding

E3 phage filaments were reduced to allow cysteine binding within the p3 protein to bind AuNP. By controlling the AuNP capping agent concentration, the number of bound phage per AuNP could be controlled. A schematic of the process is shown in Figure 4.1, in which phage were reduced, then bound to AuNP in varying ratios. The cysteine rich p3 was targeted for AuNP binding since it contains eight cysteines, many more of the amino acid for Au-S bonds than the other coat proteins. The p6, p7, and p9 each have one, while the p8 has none. The sequences for each of these coat proteins can be seen in Figure 4.2.

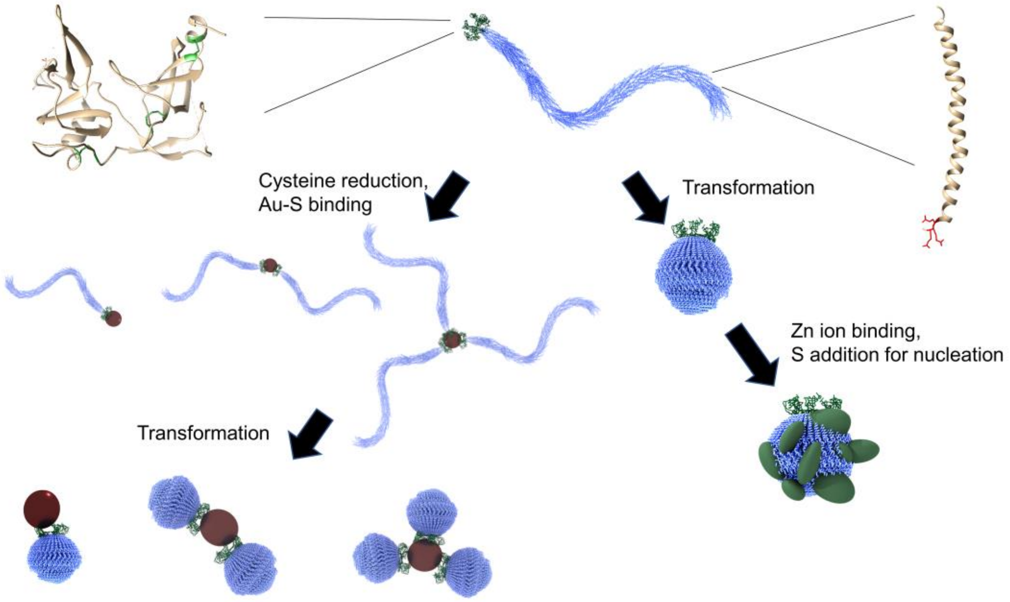

Figure 4.1 *Graphical representation of transformation and material assembly on M13 spheroid using the p3 to bind Au nanoparticles and the p8 to synthesize ZnS. In the filament, the two main capsid proteins are highlighted. The Chimera drawings for each are shown. The p3, which was not genetically modified, contains 8 total Cysteine residues, highlighted in green, which were the targets for reduction and subsequent Au binding. The p6, p7, and p9 (Figure 2) each contain a single Cysteine residue. Since there is a maximum of 5 minor capsid proteins per phage, there are a maximum of 55 Cysteine per phage. The p8 was modified to contain three negatively charged glutamate residues (highlighted in red), which allow the p8 to electrostatically bind Zn ions and nucleate ZnS.*

p6

MPVLLGIPLL LRFLGFLLVT LFGYLLTFLK KGFGKIAIAI SLFLALIIGL NSILVGYLSD ISAQLPSDFV
QGVQLILPSN ALPCFYVILS VKAAIFIFDV KQKIVSYLDW DK

p7

MEQVADFDTI YQAMIQISVV LCFALGIIAG GQR

p9

MSVLVYSFAS FVLGWCLRSG ITYFTRLMET SS

Figure 4.2 *The amino acid sequences of p6, p7, and p9 are shown, with the single Cysteine in each protein highlighted in green*

The disulfide bridges within the p3 of E3 filaments were first reduced to allow Au-S binding. Following reduction with, and removal of $NaBH_4$, via filtration, phage concentrations were measured via absorption spectroscopy, which is shown in Figure 4.3a. To make accurate calculations of phage concentrations in each sample, Rayleigh Scattering adjustments were made, which subtracts effects of nanoparticle scattering to isolate absorption spectra.[161] From this, it was found that there was a 5% loss of filaments and 12% loss of spheroids during the filtration process. Due the higher likelihood of aggregation in the spheroid form,[122] it is likely that aggregation, and subsequent lack of resuspension of aggregates, contributes to the higher loss.

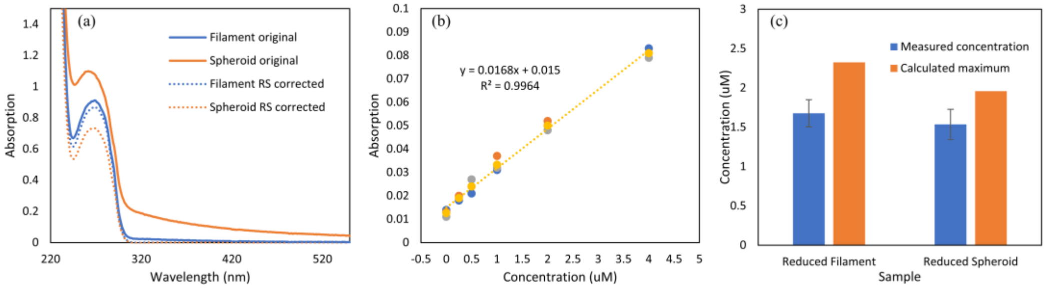

Figure 4.3 *a) Absorption of spheroids and filaments following reduction and filtration. To calculate accurate concentrations, Rayleigh scattering (RS) correction was done, and shown in dotted spectra. During filtration, higher loss of spheroids was observed than for filaments. b) Calibration curve of Ellmans Reagent mixed with increasing concentrations of L-Cysteine. c) Ellmans reagent was used to detect concentration of available cysteine residues following reduction, shown in blue in part (c). Maximum available cysteine are shown in orange. Unreduced phage did not show any reactivity with Ellmans reagent. Reduced cysteine yields were 72±10% for filaments and 78±12% for spheroids.*

The concentration of reduced sulfur bonds in the phage solutions were quantified with Ellman's reagent, a molecule that binds to cysteine groups and then displays a characteristic absorption at 412 nm. Prior to interaction with phage, a calibration curve of Ellman's reagent absorption was made by interaction with free L-Cysteine HCl, and is shown in Figure 4.3b. For filaments, an average concentration of 1.67±0.17 µM of free cysteine groups was measured, out of a total 2.32 μM, shown in Figure 4.3c. This gives a yield of 72 ± 10%, or an average of 40 free bonds of the total 55 per phage. Similarly for spheroids, an average concentration of 1.54±0.19 μM of free cysteine groups was measured, out of a total 1.95 μM, giving a slightly higher yield of 78±13%, or about 43 of the 55 cysteine bonds per spheroid. This slightly higher yield may indicate that the cysteine bonds are more accessible in the spheroid than the filament, a possibility since the protein packing is known to be less structured and rigid in the spheroid.[162] Of the 55 cysteine residues per phage, 73% of them are found in the p3, while the rest are in the p6, p7, and p9 proteins. It may be that all p3 in the filament form are reduced in this process, and those in the p6, p7, and p9 are not accessible, but due to the dramatic rearrangement of the coat proteins during transformation, some of the cysteines in these other coat proteins become accessible to $NaBH_4$.

Following the reduction process, the filaments and spheroids were then interacted with AuNP which had varying concentrations of BSA capping agent. Spheroids could not be directly bound to AuNP, as efficient binding requires 37°C, a temperature which spheroids cannot survive.[29] Experiments done with spheroids at these temperatures did not have any remaining spheroids that could be found in TEM analysis (data not shown). As such, filaments were first bound to AuNP, then transformed. TEM images of the range of filament-bound AuNP structures are shown in Figure 4.4, along with histograms of the numbers of bound filaments per AuNP. To both stabilize the AuNP in TBS, and control the exposed surface area of the nanoparticles, BSA was added as a capping agent in varying concentrations. With increasing concentrations of BSA, the average number of bound filaments to each AuNP decreased, and is shown in Figure 4.5. At 0 μg/mL, all AuNP were agglomerated, which prohibited quantification. At 50 μg/mL, minimal phage binding occurred. At 5 μg/mL, the number of phage per AuNP was highest, without large amounts of AuNP agglomeration. The different degrees of capping agent allowed control over the number of bound phage per AuNP by controlling the amount of exposed surface area available on each AuNP.

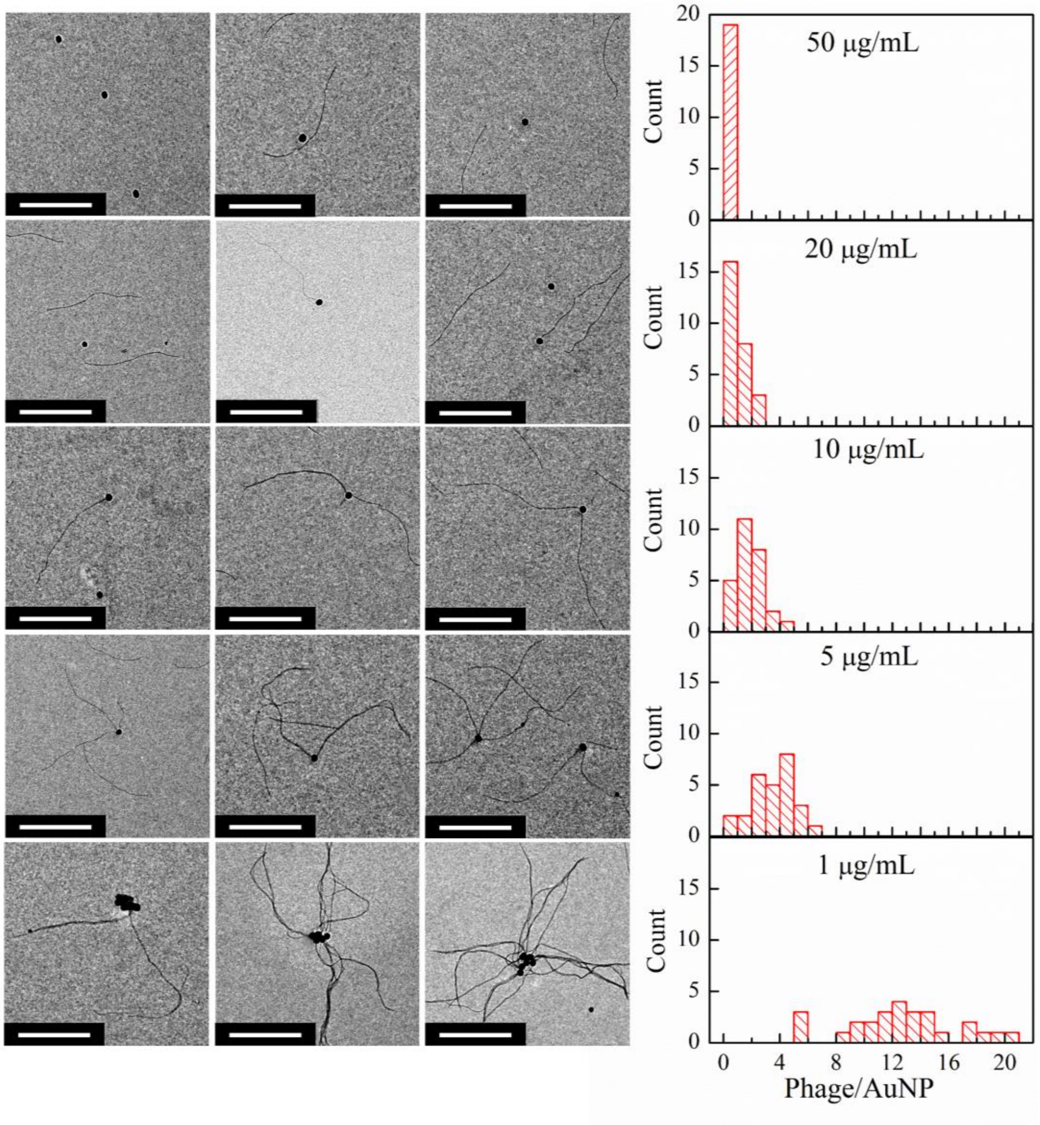

Figure 4.4 *TEM images of 1, 5, 10, 20, and 50 ug/mL BSA with AuNP that were mixed with reduced filaments. Histograms of the counted filaments bound per AuNP for each BSA concentration are shown in each respective row. Scale bar: 500 nm*

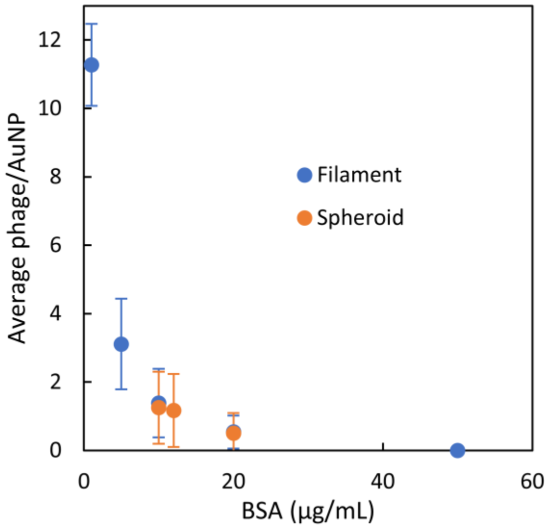

Figure 4.5 *Average number of bound phage per AuNP as a function of increasing BSA capping agent.*

Once filaments were bound to AuNP, some solutions were transformed via chloroform interaction, and it was found that transformation could proceed while bound. TEM results of the transformed phage-bound AuNP are shown in Figure 4.6, with histograms of the numbers of spheroids per AuNP shown with each condition. No filament or rod forms were observed after the transformation process. Comparison of the averages of spheroids and filaments per AuNP shown in Figure 4.5, show very close to the average numbers between the two forms. This indicates that phage are not detached during the transformation process, and that even while bound, the p3 is still accessible enough to trigger the transformation process. This also showed that the Au-S bonds between the p3 and AuNP are not affected by the transformation process. And finally, it showed that hierarchical structures with either filament or spheroid phage could be assembled, and could therefore be used in ZnS synthesis.

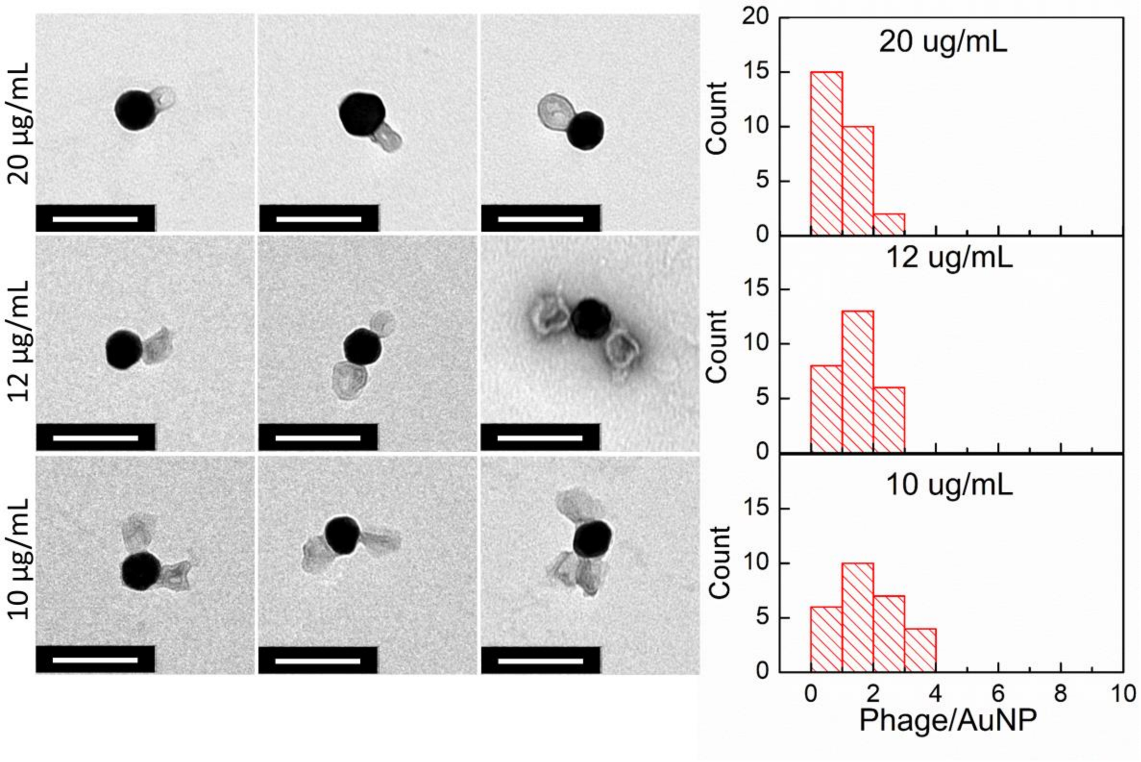

Figure 4.6 *TEM images of 10, 12, and 20 ug/mL BSA with AuNP that were mixed with reduced filaments and then converted to spheroids. Histograms of the transformed spheroids per AuNP for each BSA concentration are shown in each respective row. Scale bar: 100 nm*

4.3.2 Spheroid guided ZnS synthesis

Separately, the E3 spheroids were used in the synthesis of ZnS. Prior to synthesis, the E3 filaments were converted to spheroid form, and the particle size and morphology were first characterized via TEM, which can be seen in Figure 4.7a-4.7c. An average size of 75.6±17 nm was found, and a histogram of the measured sizes is shown in Figure 4.7d. These particles were 30 nm larger than the Au/ZnS-binding spheroids prepared in the same manner. It has no p3 insert, and a short p8 insert, so compared with wild-type, Au-binding, and Au/ZnS-binding phage, it would be expected to produce smaller spheroids.[122] It may be that high charge of the glutamic acid residues in the p8 affects the propensity of spheroid expansion, but this is speculation, and further research is required to understand the mechanism behind the large spheroid size, as it does not follow previous findings.

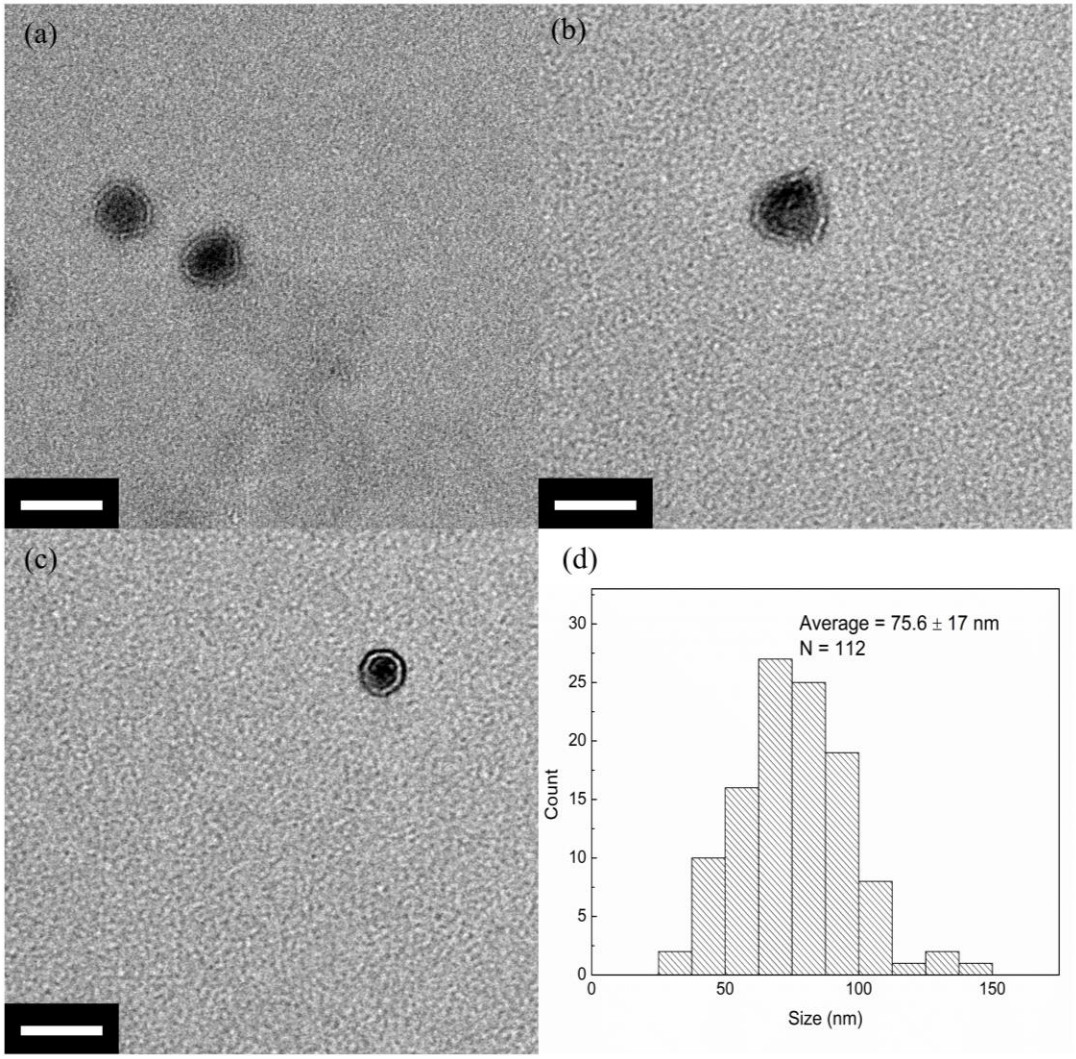

Figure 4.7 *a-c) high magnification TEM of representative spheroids (Uranyl acetate stained) d) histogram of spheroid sizes. Scale bar: 100 nm.*

Following transformation, the spheroids were used to synthesize ZnS, using a modified procedure from earlier results,[163] with only precursor concentration increased. TEM results of this process are shown in Figure 4.8a-4.8c. The synthesis produced irregular, asymmetric material, unlike the ZnS particles shown previously.[163] And unlike the spheroid template, which had an aspect ratio of 1.13, the templated ZnS material had an average aspect ratio of 1.49. Absorption of the ZnS material was measured, and shown in Figure 4.9a, which absorbed primarily in the UV. Taucs method was used to estimate the bandgap of the ZnS material, which showed a value of 3.81 eV. This is slightly larger than the bulk bandgap, indicating quantum confinement effects.

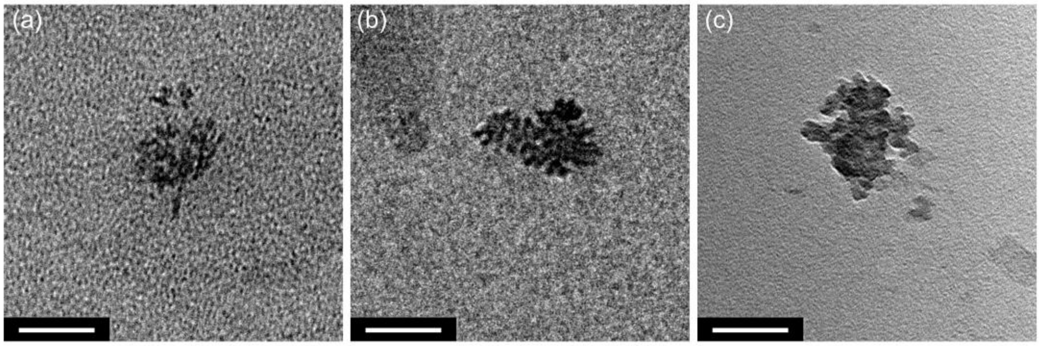

Figure 4.8 *a-c) TEM of spheroids following ZnS. Scale bar: 50 nm*

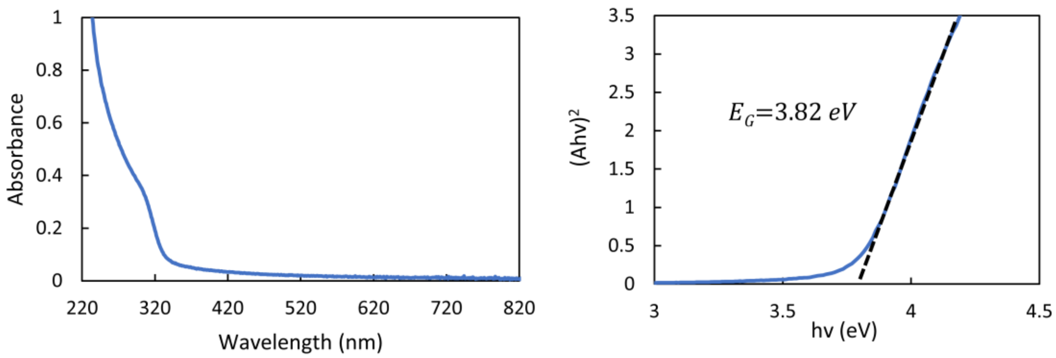

Figure 4.9 *(a) Absorption spectrum of spheroids/ZnS and spheroids/AuNP (b) Taucs method for bandgap estimation*

4.2 Conclusion

In this chapter we have shown that cysteine residues can be reduced with $NaBH_4$, and the open sulfur bonds within could be quantified with Ellmans reagent. While about 70% of the cysteine groups could be reduced in both the spheroid and filament forms, the yield was slightly higher in the spheroid, which could be a result of the less rigid protein coat.[26] The reduced filaments were then used to bind AuNP, and the number of bound phage per AuNP could be controlled by varying the amounts of BSA capping agent. While the spheroids could not survive the reduction process, we showed that the bound filaments could be transformed, and that the phage were not removed from the AuNP in the process. The conversion of unbound E3 spheroids was characterized, and we then showed that the spheroids could synthesize ZnS across most of the protein coat. This work shows that the assembly of hierarchical nanostructures is possible, by changing the number of phage per AuNP. If combined with ZnS, core-satellite structures could be assembled, which would strongly absorb across both UV and visible wavelengths. This work developed the process of making bifunctional spheroids from a phage with only one genetic modification, and by increasing the semiconductor satellite coverage around a metal nanoparticle core, these particles show potential as efficient UV or visible light driven photocatalysts.

Chapter 5. Conclusions and Future Work

5.1 Conclusion

In this work, we have developed the process of conversion from a spherical template capable of asymmetrically assembling ZnS and Au nanoparticles, from the filamentous M13 bacteriophage. First, the p3 of the Au-binding phage was genetically modified to display a ZnS-binding peptide, which was proven through DNA sequencing of the new phage's genome. We observed that this new Au/ZnS-binding phage was converted to spheroid form at a different rate than the Au-binding phage, so the changes in secondary structure and morphology were characterized on a vortexing cycle-by-cycle basis. By using circular dichroism and fluorescence spectroscopy, significant changes in p8 secondary structure and inter-p8 binding was seen, which were all at more dramatic rates than the phage without the p3 insert. Together, these observations indicated that fewer cycles were required to convert the Au/ZnS-binding phage, which were then corroborated with TEM cycle-by-cycle investigations. Following these findings, we proposed two possible mechanisms for the differences. First, that mutations may cause partial unfolding of the p3 protein, exposing the buried hydrophobic regions and thus promoting chloroform interaction. Alternatively, seeing as the p3 dictates the arrangement of the proximal tip proteins, mutations in the p3 may modify the proteins' interaction with the neighboring p8 and allow increased chloroform access, thereby modifying the spheroid conversion process.

Upon the discovery that the bi-functional spheroid's stability was not sufficient to survive the 10 hour ZnS synthesis process, a low-temperature conversion method was adapted from previous work[36] which allowed smaller, aggregation-resistant spheroid templates. The more compact structure was thought to limit the solvent exposure to the hydrophobic residues within the p3 and p8 proteins that terminate the phage body, and limit agglomeration. These spheroids were used in subsequent inorganic synthesis experiments.

Next, we then showed that after spheroid conversion, the p3 retained its ZnS-synthesis capability and was able to nucleate small nanoparticles, similar to the filament form. Differently from the filament however, and to our benefit, the spheroids did not aggregate around clusters of nanoparticles. Similar to previous research,[4] the spheroid was also capable to synthesizing Au on the p8, producing particles which were slightly larger than what were formed on the filament form. We found that these new hybrid Au/ZnS particles were photocatalytically active in the degradation of methylene blue dye, and even displayed some enhancement over ZnS or Au alone under UV illumination. Unfortunately, rates were low, likely due to the small size of ZnS particles. As such, the ZnS synthesis procedure was adapted to form larger particles, by increasing the ratio of Zn:S precursors, which increased the particle size substantially, and showed modest improvements in photocatalytic rates.

When combined with Au, the normally UV-absorbing semiconductor was able to degrade dye under visible light illumination. Since Au did not display much photocatalytic activity on its own, it was determined that the combination of ZnS and Au allowed hot electron injection under plasmon resonance conditions from the Au to ZnS, and that heating effects could be ruled out. When the semiconductor/metal interface was limited, by binding Au nanoparticles rather than synthesizing a coat of Au material over the spheroid surface, a small but significant reduction in photocatalysis rates were observed. With this we determined that efficient charge transfer required a good interface between the two materials. As another control, erioglaucine dye was used in place of methylene blue. This is a negatively charged dye, and therefore electrostatically repelled from the similarly charged ZnS and Au in water. It also has minimal absorption at the wavelengths emitted by the visible light excitation source. By eliminating direct contact, and minimizing dye excitation, direct dye photosensitization was ruled out. We concluded that photocatalytic degradation was therefore done by reactive oxygen species generated by the catalyst, and not directly on the surface of the particle. It was believed that the ZnS surface area was the limiting factor in further improvements to photocatalysis.

Therefore, to further increase the ZnS surface area, a new phage was used, which displayed 3 glutamate residues on its p8 that were capable of electrostatically binding to Zn ions and nucleating ZnS. Also, by chemically modifying the p3 protein, the buried Cysteine residues were reduced, which allowed binding of Au nanoparticles to the free Sulfur bonds. Ellmans reagent was used, which showed that the majority of the Cysteine residues were . Using this method and the E3 phage, role reversal of the proteins was achieved, which provided better platforms for interaction with inorganic material than the Au/ZnS-binding phage. Further, this allowed assembly of increasingly complex structures, by binding varying numbers of spheroids around single Au nanoparticle ‘cores’. The spheroid coverage around the AuNP were characterized primarily with TEM, which could be controlled through varying concentrations of BSA capping agent. The spheroids were also used as ZnS synthesis sites. UV-vis spectroscopy of the materials showed high UV and visible light absorption, so it was expected that these particles would display high photocatalytic activity at UV and visible wavelengths.

5.2 Future Work

Finally, it was shown in initial research that the p3 insert caused unexpected changes in the Au-binding phage (in p8 protein). It was not fully understood whether those changes were due to that particular peptide, or whether it was a compounding effect due to dual p8 and p3 modifications. To identify the cause, a phage with no p8 modification and the ZnS-binding peptide in the p3 should be prepared, then analyzed with cycle-by-cycle comparison with the other phage shown in this work using CD, PL, and TEM. It would be interesting to know how spheroid formation progresses with this phage type, as wild-type has already been characterized with these methods.

To further the development of spheroid applications as a material template, the transformation process must be expanded. Much of the work developed here relied on the transformation of M13 at a very specific volume and concentration, and any substantial changes to those conditions resulted in the agglomeration of much of the phage solution. Many potential applications and characterization methods require higher material concentrations than what used in this work. Therefore, work must be done in developing the transformation process at higher volumes and concentrations. Scale up of any part of the process will be limited until this can be done. This would be extremely beneficial to photocatalysis characterization, where literature comparisons rely on rate constants. Here, catalyst mass is not taken into account. For this reason, rates shown in this work, with 100's of nanograms, cannot be fairly compared to other work using 10's of milligrams of catalyst material.

Most potential extensions to the current research rely on the incorporation of a third material to the present dual material system. Indeed, it has been shown that ZnS may perform better as a charge separation layer between a metal and semiconductor than the standalone semiconductor material, due to its very large bandgap.[164] In terms of phage display, bi-functionality has typically been the limit for the filamentous bacteriophage. A possible workaround is incorporating two different peptides into the p8 coat, which would potentially allow a third functionality in the p3. Recently, however, work using p7 display has shown that the peptide is extremely receptive to particular inserts, even when inserted using the phagemid system, and avoids the complications seen in p9 display.[165] Even more interesting, is that this system has been shown to work with existing p3 and p8 display functionality,[166] meaning that three distinct peptides could be displayed on each of those three coat proteins (p7, p8, and p3) with the high expression seen in classic p3 and p8 display. With this added functionality, another semiconductor particle could be synthesized on the p7 site that would work cooperatively with the existing ZnS/Au particles, and enhance their properties. Examples of such materials would be CdS,[167] ZnO,[168] or Fe3O4.[169] Each of which has a smaller bandgap than ZnS, and all have been shown to create various heterojunctions with ZnS without additional doping. Additionally, multifunctional particles with dual junctions such as these have been shown to dramatically enhance catalytic performances.[95]

This dissertation has shown that the M13 spheroid can be used as a material template to assemble asymmetric inorganic nanoparticles. It can work as a bi-functional template through genetic modification, chemical modification, or a combination of the two, which grant affinity for a variety of different materials. This work showed the application of these hybrid materials with the photocatalytic degradation of aqueous contaminants, yet some small improvements could be made to the inorganic materials which would greatly enhance the performance of the hybrid structure. For instance, efficient charge transfer between metal and semiconductor relies heavily on similar energy levels between the materials.[19] Also, hot electron injection occurs only for electrons with energy high enough to overcome the Schottky barrier. For 5 nm Au nanoparticles, the smallest size of particle with detectable resonance, which occurs at 515 nm, a relatively small fraction of the resonant plasmonic electrons surpass the estimated 2.2 eV energy barrier into ZnS. Alternatively, Ag nanoparticles display significantly higher energy plasmon resonance, and absorb in the blue-violet wavelengths. If combined with ZnS, a significantly higher number of hot electrons could therefore inject into the conduction band of the ZnS, and even more since the formed Schottky barrier is smaller than the Au/ZnS barrier height.[57] Additionally, under UV illumination conditions, photoexcited electrons would more readily transfer from the conduction band of ZnS into Ag due to the closer similarity of energy levels than in ZnS/Au.[19] By using Au coated Ag nanoparticles, the same phage type as in this work can be used, oxidation issues can be avoided, while retaining Ag plasmon resonance properties.[170]

As previously mentioned, photocatalysis of these hybrid structures depends, to varying extents, on the light absorption of the semiconductor and the metal. Typically, electron/hole pairs are more efficiently produced in the semiconductor, and the metal then helps separate them with the function of the Schottky barrier at the interface. As such, it would be beneficial if the semiconductor could absorb more of the solar spectrum than just UV, for the purpose of photocatalytic applications. A well-studied method for this is doping of ZnS with metal ions such as Mn[171] or Cr,[172] or by controlling the number of S-vacancies,[49] to introduce mid-bandgap energy states, and thereby greatly increasing the absorption spectrum into near-UV and visible wavelengths. This would also have the combined effect of increasing the absorption overlap between the semiconductor and metal, increasing charge transfer efficiency. Interestingly, Cr-doped ZnS takes on ferromagnetic properties,[173] which would have the added benefit of making the particles magnetically recoverable after photocatalytic treatment of contaminated water. Recoverability is an ongoing issue with suspension-style nanoparticle photocatalysts.

The asymmetry can be useful in many other ways. For instance, by binding a ZnS-coated Fe_3O_4 particle to the p3, and coating the p8 with Au, significant improvements can be made to the photocatalysis while simultaneously adding recovery functionality via magnetism.[174] The lower bandgap of Fe_3O_4 will provide much more energy overlap between the Au plasmonic resonance, which increases charge transfer efficiency between the two materials. Also, the ZnS coating will allow existing phage mutants to be used, while thin ZnS films have been shown to decrease oxidation of Fe_3O_4[175,176] and also increase charge lifetimes.[164]

(1) Smith, G. P. Filamentous Phage Fusion: Novel Expression Vectors That Display Cloned Antigens on the Surface of the Virion. *Science (80-.).* **1985**, *228*, 1315–1317.

(2) Griffith, J.; Manning, M.; Dunn, K. Filamentous Bacteriophage Contract into Hollow Spherical Particles upon Exposure to a Chloroform-Water Interface. *Cell* **1981**, *23*, 747–753.

(3) Chen, P. Y.; Dang, X.; Klug, M. T.; Courchesne, N. M. D.; Qi, J.; Hyder, M. N.; Belcher, A. M.; Hammond, P. T. M13 Virus-Enabled Synthesis of Titanium Dioxide Nanowires for Tunable Mesoporous Semiconducting Networks. *Chem. Mater.* **2015**, *27*, 1531–1540.

(4) Ngo-Duc, T.-T.; Plank, J. M.; Chen, G.; Harrison, R. E. S.; Morikis, D.; Liu, H.; Haberer, E. D. M13 Bacteriophage Spheroids as Scaffolds for Directed Synthesis of Spiky Gold Nanostructures. *Nanoscale* **2018**, *10*, 13055–13063.

(5) Barnhart, E. L.; Amamath, K. R. The Efficacy Of Color Removal Techniques in Textile Wastewater. *Res. Proj. 332941* **1993**, No. June 1993, 160.

(6) Karthik, V.; Saravanan, K.; Bharathi, P.; Dharanya, V.; Meiaraj, C. An Overview of Treatments for the Removal of Textile Dyes. *J. Chem. Pharm. Sci.* **2014**, *7*, 301–307.

(7) Chung, K.-T. Azo Dyes and Human Health: A Review. *J. Environ. Sci. Heal. Part C* **2016**, *34*, 233–261.

(8) J., V. Toxicity Assessment of Treated Effluents from a Textile Industry in Lagos, Nigeria. *African J. Environ. Sci. Technol.* **2014**, *6*, 438–445.

(9) Boursi, B.; Mamtani, R.; Haynes, K.; Yang, Y. X. Recurrent Antibiotic Exposure May Promote Cancer Formation-Another Step in Understanding the Role of the Human Microbiota? *Eur. J. Cancer* **2015**, *51*, 2655–2664.

(10) Wallace, J. S.; Garner, E.; Pruden, A.; Aga, D. S. Occurrence and Transformation of Veterinary Antibiotics and Antibiotic Resistance Genes in Dairy Manure Treated by Advanced Anaerobic Digestion and Conventional Treatment Methods. *Environ. Pollut.* **2018**, *236*, 764–772.

(11) Ollis, D. F. Photocatalytic Purification and Remediation of Contaminated Air and Water. *Chim. / Chem.* **2000**, *3*, 405–411.

(12) Mills, A.; Le Hunte, S. An Overview of Semiconductor Photocatalysis. *J. Photochem. Photobiol. A Chem.* **1997**, *108*, 1–35.

(13) Herrmann, J. Heterogeneous Photocatalysis: Fundamentals and Applications to the Removal of Various Types of Aqueous Pollutants. *Catal. Today* **1999**, *53*, 115–129.

(14) Yu, C.; Wu, Z.; Liu, R.; Dionysiou, D. D.; Yang, K.; Wang, C.; Liu, H. Novel Fluorinated Bi2MoO6 Nanocrystals for Efficient Photocatalytic Removal of Water Organic Pollutants under Different Light Source Illumination. *Appl. Catal. B Environ.* **2017**, *209*, 1–11.

(15) Margan, P.; Haghighi, M. Sono-Coprecipitation Synthesis and Physicochemical Characterization of CdO-ZnO Nanophotocatalyst for Removal of Acid Orange 7 from Wastewater. *Ultrason. Sonochem.* **2018**, *40*, 323–332.

(16) Yi, Z.; Ye, J.; Kikugawa, N.; Kako, T.; Ouyang, S.; Stuart-Williams, H.; Yang, H.; Cao, J.; Luo, W.; Li, Z.; et al. An Orthophosphate Semiconductor with Photooxidation Properties under Visible-Light Irradiation. *Nat. Mater.* **2010**, *9*, 559–564.

(17) Wang, H.; Zhang, L.; Chen, Z.; Hu, J.; Li, S.; Wang, Z.; Liu, J.; Wang, X. Semiconductor Heterojunction Photocatalysts: Design, Construction, and Photocatalytic Performances. *Chem. Soc. Rev.* **2014**, *43*, 5234–5244.

(18) Rao, H.; Lu, Z.; Liu, X.; Ge, H.; Zhang, Z.; Zou, P.; He, H.; Wang, Y. Visible Light-Driven Photocatalytic Degradation Performance for Methylene Blue with Different Multi-Morphological Features of ZnS. *RSC Adv.* **2016**, *6*, 46299–46307.

(19) Jiang, R.; Li, B.; Fang, C.; Wang, J. Metal/Semiconductor Hybrid Nanostructures for Plasmon-Enhanced Applications. *Adv. Mater.* **2014**, *26*, 5274–5309.

(20) Seh, Z. W.; Liu, S.; Low, M.; Zhang, S.-Y.; Liu, Z.; Mlayah, A.; Han, M.-Y. Janus Au-TiO $_2$ Photocatalysts with Strong Localization of Plasmonic Near-Fields for Efficient Visible-Light Hydrogen Generation. *Adv. Mater.* **2012**, *24*, 2310–2314.

(21) Sze, S. M.; Kwok, K. N. *Physics of Semiconductor Devices*; 2007.

(22) Barbas, C. F.; Burton, D. R.; Silverman, G. J. *Phage Display: A Laboratory Manual*; G - Reference,Information and Interdisciplinary Subjects Series; Cold Spring Harbor Laboratory Press, 2004.

(23) Rakonjac, J.; Model, P. Roles of PIII in Filamentous Phage Assembly. *J. Mol. Biol.* **1998**, *282*, 25–41.

(24) Rossomando, E. F.; Milstien, J. B. Electro-Optic Evidence for the Control of the Structure of Bacteriophage F1 by a Minor Coat Protein. *J. Mol. Biol.* **1971**, *58*, 187–195.

(25) Marvin, D. Filamentous Phage Structure, Infection and Assembly. *Curr. Opin. Struct. Biol.* **1998**, *8*, 150–158.

(26) Roberts, L. M.; Dunker, A. K. Structural Changes Accompanying Chloroform-Induced Contraction of the Filamentous Phage Fd. *Biochemistry* **1993**, *32*, 10479–10488.

(27) Bruckman, M. A.; Vanmeter, A.; Steinmetz, N. F. High Throughput Transition of Tobacco Mosaic Virus Rods to Spheres Using a Mesofluidic Device. 1–19.

(28) Nikitin, N.; Ksenofontov, A.; Trifonova, E.; Arkhipenko, M.; Petrova, E.; Kondakova, O.; Kirpichnikov, M.; Atabekov, J.; Dobrov, E.; Karpova, O. Thermal Conversion of Filamentous Potato Virus X into Spherical Particles with Different Properties from Virions. *FEBS Lett.* **2016**, *590*, 1543–1551.

(29) Manning, M.; Chrysogelos, S.; Griffith, J. Mechanism of Coliphage M13 Contraction: Intermediate Structures Trapped at Low Temperatures. *J. Virol.* **1981**, *40*, 912–919.

(30) Lopez, J.; Webster, R. E. Minor Coat Protein Composition and Location of the A Protein in Bacteriophage F1 Spheroids and I-Forms. *J Virol* **1982**, *42*, 1099–1107.

(31) Marvin, D. A.; Symmons, M. F.; Straus, S. K. Structure and Assembly of Filamentous Bacteriophages. *Prog. Biophys. Mol. Biol.* **2014**, *114*, 80–122.

(32) Oh, J. S.; Davies, D. R.; Lawson, J. D.; Arnold, G. E.; Dunker, A. K. Isolation of Chloroform-Resistant Mutants of Filamentous Phage: Localization in Models of Phage Structure. *J. Mol. Biol.* **1999**, *287*, 449–457.

(33) Avery, K. N.; Schaak, J. E.; Schaak, R. E.; Pennsyl, T.; State, V.; Uni, V.; Park, U. V; Pennsyl, V. M13 Bacteriophage as a Biological Scaffold for Magnetically-Recoverable Metal Nanowire Catalysts : Combining Specific and Nonspecific Interactions To Design Multifunctional Nanocomposites Biological Molecules and Organisms Are Intriguing Scaf- Folds for T. **2009**, No. 33, 2176–2178.

(34) Huang, Y.; Chiang, C.; Lee, S. K.; Gao, Y.; Hu, E. L. Programmable Assembly of Nanoarchitectures Using Genetically Engineered Viruses. *Nano Lett.* **2005**, *5*, 1429–1434.

(35) Nam, K. T.; Kim, D.; Yoo, P. J.; Chiang, C.; Meethong, N.; Hammond, P. T.; Chiang, Y.; Belcher, A. M. Virus-Enabled Synthesis and Assembly Battery Electrodes. *Science (80-.).* **2006**, *312*, 885–889.

(36) Mao, C.; Flynn, C. E.; Hayhurst, A.; Sweeney, R.; Qi, J.; Georgiou, G.; Iverson, B.; Belcher, A. M. Viral Assembly of Oriented Quantum Dot Nanowires. *Proc. Natl. Acad. Sci. U. S. A.* **2003**, *100*, 6946–6951.

(37) Bruckman, M. A.; Hern, S.; Jiang, K.; Flask, C. A.; Yu, X.; Steinmetz, N. F. Tobacco Mosaic Virus Rods and Spheres as Supramolecular High-Relaxivity MRI Contrast Agents. *J. Mater. Chem. B. Mater. Biol. Med.* **2013**, *1*, 1482–1490.

(38) Zhou, Z.; Bedwell, G. J.; Li, R.; Bao, N.; Prevelige, P. E.; Gupta, A. P22 Virus-like Particles Constructed Au/CdS Plasmonic Photocatalytic Nanostructures for Enhanced Photoactivity. *Chem. Commun. (Camb).* **2015**, *51*, 1062–1065.

(39) Vogel, W.; Borse, P. H.; Deshmukh, N.; Kulkarni, S. K. Structure and Stability of

Monodisperse 1.4-Nm ZnS Particles Stabilized by Mercaptoethanol. *Langmuir* **2000**, *16*, 2032–2037.

(40) Huo, F.; Wang, Y.; You, C.; Deng, W.; Yang, F.; Pu, Y. Phase- and Size-Controllable Synthesis with Efficient Photocatalytic Activity of ZnS Nanoparticles. *J. Mater. Sci.* **2017**, *52*, 5626–5633.

(41) Hu, J.-S.; Ren, L.-L.; Guo, Y.-G.; Liang, H.-P.; Cao, A.-M.; Wan, L.-J.; Bai, C.-L. Mass Production and High Photocatalytic Activity of ZnS Nanoporous Nanoparticles. *Angew. Chem. Int. Ed. Engl.* **2005**, *44*, 1269–1273.

(42) Haruta, M.; Daté, M. Advances in the Catalysis of Au Nanoparticles. *Appl. Catal. A Gen.* **2001**, *222*, 427–437.

(43) Fang, X.; Zhai, T.; Gautam, U. K.; Li, L.; Wu, L.; Bando, Y.; Golberg, D. ZnS Nanostructures: From Synthesis to Applications. *Prog. Mater. Sci.* **2011**, *56*, 175–287.

(44) Zhang, J.; Wang, Y.; Zhang, J.; Lin, Z.; Huang, F.; Yu, J. Enhanced Photocatalytic Hydrogen Production Activities of Au-Loaded ZnS Flowers. *ACS Appl. Mater. Interfaces* **2013**, *5*, 1031–1037.

(45) Kozák, O.; Praus, P.; Kočí, K.; Klementová, M. Preparation and Characterization of ZnS Nanoparticles Deposited on Montmorillonite. *J. Colloid Interface Sci.* **2010**, *352*, 244–251.

(46) Zhu, H.; Song, N.; Lian, T. Controlling Charge Separation and Recombination Rates in CdSe/ZnS Type i Core-Shell Quantum Dots by Shell Thicknesses. *J. Am. Chem. Soc.* **2010**, *132*, 15038–15045.

(47) Lin, K. B.; Su, Y. H. Photoluminescence of Cu:ZnS, Ag:ZnS, and Au:ZnS Nanoparticles Applied in Bio-LED. *Appl. Phys. B Lasers Opt.* **2013**, *113*, 351–359.

(48) Li, Y.; Zhou, S.; Chen, Z.; Yang, Y.; Chen, N.; Du, G. Luminescence Properties of Br-Doped ZnS Nanoparticles Synthesized by a Low Temperature Solid-State Reaction Method. *Ceram. Int.* **2013**, *39*, 5521–5525.

(49) Wang, G.; Huang, B.; Li, Z.; Lou, Z.; Wang, Z.; Dai, Y.; Whangbo, M.-H. Synthesis and Characterization of ZnS with Controlled Amount of S Vacancies for Photocatalytic H2 Production under Visible Light. *Sci. Rep.* **2015**, *5*, 8544.

(50) Liang, Y.-C.; Lo, Y.-R.; Wang, C.-C.; Xu, N.-C. Shell Layer Thickness-Dependent Photocatalytic Activity of Sputtering Synthesized Hexagonally Structured ZnO-ZnS Composite Nanorods. *Materials (Basel).* **2018**, *11*, 87.

(51) Misra, M.; Gupta, R. K.; Paul, A. K.; Singla, M. Influence of Gold Core Concentration on Visible Photocatalytic Activity of Gold-Zinc Sulfide Core-Shell Nanoparticle. *J. Power Sources* **2015**, *294*, 580–587.

(52) Choi, Y. I.; Lee, S.; Kim, S. K.; Kim, Y. Il; Cho, D. W.; Khan, M. M.; Sohn, Y. Fabrication of ZnO, ZnS, Ag-ZnS, and Au-ZnS Microspheres for Photocatalytic Activities, CO Oxidation and 2-Hydroxyterephthalic Acid Synthesis. *J. Alloys Compd.* **2016**, *675*, 46–56.

(53) Zhang, X.; Chen, Y. L.; Liu, R.-S.; Tsai, D. P. Plasmonic Photocatalysis. *Rep. Prog. Phys.* **2013**, *76*, 046401.

(54) Chen, W. T.; Hsu, Y. J. L -Cysteine-Assisted Growth of Core-Satellite ZnS-Au Nanoassemblies with High Photocatalytic Efficiency. *Langmuir* **2010**, *26*, 5918–5925.

(55) Adkour, M. E. M.; Agheer, F. A. A. L. S. Au / ZnS and Ag / ZnS Nanoheterostructures as Regenerated Nanophotocatalysts for Photocatalytic Degradation of Organic Dyes. **2017**, *7*, 19156–19166.

(56) Chen, W.; Wang, Z.; Lin, Z.; Lin, L. Absorption and Luminescence of the Surface States in ZnS Nanoparticles. *J. Appl. Phys.* **1997**, *82*, 3111–3115.

(57) Wolfframm, D.; Evans, D. A.; Neuhold, G.; Horn, K. Gold and Silver Schottky Barriers on ZnS(110). *J. Appl. Phys.* **2000**, *87*, 3905–3911.

(58) Lin, Z.; Wang, X.; Liu, J.; Tian, Z.; Dai, L.; He, B.; Han, C.; Wu, Y.; Zeng, Z.; Hu, Z. On the Role of Localized Surface Plasmon Resonance in UV-Vis Light Irradiated Au/TiO\n 2\n Photocatalysis Systems: Pros and Cons. *Nanoscale* **2015**, *7*, 4114–4123.

(59) Schick, I.; Lorenz, S.; Gehrig, D.; Tenzer, S.; Storck, W.; Fischer, K.; Strand, D.; Laquai, F.; Tremel, W. Inorganic Janus Particles for Biomedical Applications. *Beilstein J. Nanotechnol.* **2014**, *5*, 2346–2362.

(60) Qiao, Y.; Du, Y.; Zhang, X.; Li, Y. Preparation at the Water–Oil Interface of Janus Composite Nanoparticles and Their Photoelectric Properties. *J. Appl. Polym. Sci.* **2017**, *134*, 1–7.

(61) Hu, J.; Zhou, S.; Sun, Y.; Fang, X.; Wu, L. Fabrication, Properties and Applications of Janus Particles. *Chem. Soc. Rev.* **2012**, *41*, 4356–4378.

(62) Yi, Y.; Sanchez, L.; Gao, Y.; Yu, Y. Janus Particles for Biological Imaging and Sensing. *Analyst* **2017**, *141*, 3526–3539.

(63) Gao, H. M.; Lu, Z. Y.; Liu, H.; Sun, Z. Y.; An, L. J. Orientation and Surface Activity of Janus Particles at Fluid-Fluid Interfaces. *J. Chem. Phys.* **2014**, *141*, 1–9.

(64) Casagrande, C.; Fabre, P.; Raphaël, E.; Veyssié, M. Janus Beads: Realization and Behaviour at Water/Oil Interfaces. *Epl* **1989**, *9*, 251–255.

(65) Gu, H.; Yang, Z.; Gao, J.; Chang, C. K.; Xu, B. Heterodimers of Nanoparticles:

Formation at a Liquid-Liquid Interface and Particle-Specific Surface Modification by Functional Molecules. *J. Am. Chem. Soc.* **2005**, *127*, 34–35.

(66) Tiewcharoen, S.; Warakulwit, C.; Lapeyre, V.; Garrigue, P.; Fourier, L.; Elissalde, C.; Buffière, S.; Legros, P.; Gayot, M.; Limtrakul, J.; et al. Anisotropic Metal Deposition on TiO2 Particles by Electric-Field-Induced Charge Separation. *Angew. Chemie - Int. Ed.* **2017**, *56*, 11431–11435.

(67) Xue, Z. H.; Su, H.; Yu, Q. Y.; Zhang, B.; Wang, H. H.; Li, X. H.; Chen, J. S. Janus Co/CoP Nanoparticles as Efficient Mott–Schottky Electrocatalysts for Overall Water Splitting in Wide PH Range. *Adv. Energy Mater.* **2017**, *7*, 1–7.

(68) Becker, A.; Schierning, G.; Theissmann, R.; Meseth, M.; Benson, N.; Schmechel, R.; Schwesig, D.; Petermann, N.; Wiggers, H.; Ziolkowski, P. A Sintered Nanoparticle P-n Junction Observed by a Seebeck Microscan. *J. Appl. Phys.* **2012**, *111*, 1–7.

(69) Mohanta, K.; Batabyal, S. K.; Pal, A. J. Pn-Junction Rectifiers Based on p-ZnO and n-ZnO Nanoparticles. *Chem. Mater.* **2007**, *19*, 3662–3666.

(70) Zhang, Z.; Wang, L.; Wang, J.; Jiang, X.; Li, X.; Hu, Z.; Ji, Y.; Wu, X.; Chen, C. Janus Au-TiO 2 Photocatalysts with Strong Localization of Plasmonic near-Fields for Efficient Visible-Light Hydrogen Generation SI. *Adv. Mater.* **2012**, *24*, 1418–1423.

(71) Wu, K.; Chen, J.; McBride, J. R.; Lian, T. Efficient Hot-Electron Transfer by a Plasmon-Induced Interfacial Charge-Transfer Transition. *Science (80-.).* **2015**, *349*, 632–635.

(72) Wu, L. Y.; Ross, B. M.; Hong, S. G.; Lee, L. P. Bioinspired Nanocorals with Decoupled Cellular Targeting and Sensing Functionality. *Small* **2010**, *6*, 503–507.

(73) Fu, X.; Liu, J.; Yang, H.; Sun, J.; Li, X.; Zhang, X.; Jia, Y. Arrays of Au-TiO2 Janus-like Nanoparticles Fabricated by Block Copolymer Templates and Their Photocatalytic Activity in the Degradation of Methylene Blue. *Mater. Chem. Phys.* **2011**, *130*, 334–339.

(74) Pacheco, M.; Jurado-Sanchez, B.; Escarpa, A. Lab-on-a-Micromotor: Catalytic Janus Particles as Mobile Microreactors for Tailored Synthesis of Nanoparticles. *Chem. Sci* **2018**, *9*, 8056–8064.

(75) Park, J.; Park, J.; Lee, J.; Oh, A.; Baik, H.; Lee, K. Janus Nanoparticle Structural Motif Control via Asymmetric Cation Exchange in Edge-Protected Cu1.81S@IrxSyHexagonal Nanoplates. *ACS Nano* **2018**, *12*, 7996–8005.

(76) Zhu, M. J.; Pan, J. Bin; Wu, Z. Q.; Gao, X. Y.; Zhao, W.; Xia, X. H.; Xu, J. J.; Chen, H. Y. Electrogenerated Chemiluminescence Imaging of Electrocatalysis at a Single Au-Pt Janus Nanoparticle. *Angew. Chemie - Int. Ed.* **2018**, *57*, 4010–4014.

(77) He, J.; Perez, M. T.; Zhang, P.; Babu, T.; Gong, J.; Nie, Z. A General Approach to Synthesize Asymmetric Hybrid Nanoparticles by Interfacial Reactions. *J. Am. Chem. Soc* **2012**, *134*, 3639–3642.

(78) Pradhan, S.; Ghosh, D.; Chen, S. Janus Nanostructures Based on Au-TiO2 Heterodimers and Their Photocatalytic Activity in the Oxidation of Methanol. *ACS Appl. Mater. Interfaces* **2009**, *1*, 2060–2065.

(79) Li, F.; Chen, Y.; Chen, H.; He, W.; Zhang, Z. P.; Zhang, X. E.; Wang, Q. Monofunctionalization of Protein Nanocages. *J. Am. Chem. Soc.* **2011**, *133*, 20040–20043.

(80) Royston, E.; Ghosh, A.; Kofinas, P.; Harris, M. T.; Culver, J. N. Self-Assembly of Virus-Structured High Surface Area Nanomaterials and Their Application as Battery Electrodes. *Langmuir* **2008**, *24*, 906–912.

(81) Merzlyak, A.; Lee, S. W. Engineering Phage Materials with Desired Peptide Display: Rational Design Sustained through Natural Selection. *Bioconjug. Chem.* **2009**, *20*, 2300–2310.

(82) Petrenko, V. A.; Smith, G. P.; Gong, X.; Quinn, T. A Library of Organic Landscapes on Filamentous Phage. *Protein Eng.* **1996**, *9*, 797–801.

(83) Seker, U. O. S.; Demir, H. V. Material Binding Peptides for Nanotechnology. *Molecules* **2011**, *16*, 1426–1451.

(84) Moon, J.-S.; Kim, W.-G.; Kim, C.; Park, G.-T.; Heo, J.; Yoo, S. Y.; Oh, J.-W. M13 Bacteriophage-Based Self-Assembly Structures and Their Functional Capabilities. *Mini. Rev. Org. Chem.* **2015**, *12*, 271–281.

(85) Lee, S.; Mao, C.; Flynn, C. E.; Belcher, A. M. Ordering of Quantum Dots Using Genetically Engineered Viruses. *Science* **2002**, *296*, 892–895.

(86) Chung, S.; Chung, W.-J.; Wang, D.; Lee, S.-W.; De Yoreo, J. Growth of Au and ZnS Nanostructures via Engineered Peptide and M13 Bacteriophage Templates. *Soft Matter* **2018**, *16*, 2996–3002.

(87) Flynn, C. E.; Mao, C.; Hayhurst, A.; Williams, J. L.; Georgiou, G.; Iverson, B.; Belcher, A. M. Synthesis and Organization of Nanoscale II–VI Semiconductor Materials Using Evolved Peptide Specificity and Viral Capsid Assembly. *J. Mater. Chem.* **2003**, *13*, 2414–2421.

(88) Warner, C. M.; Barker, N.; Lee, S. W.; Perkins, E. J. M13 Bacteriophage Production for Large-Scale Applications. *Bioprocess Biosyst. Eng.* **2014**, *37*, 2067–2072.

(89) Zhou, K.; Eiben, S.; Wang, Q. Coassembly of Tobacco Mosaic Virus Coat Proteins into Nanotubes with Uniform Length and Improved Physical Stability. *ACS Appl. Mater. Interfaces* **2016**, *8*, 13192–13196.

(90) Altintoprak, K.; Seidenstücker, A.; Welle, A.; Eiben, S.; Atanasova, P.; Stitz, N.; Plettl, A.; Bill, J.; Gliemann, H.; Jeske, H.; et al. Peptide-Equipped Tobacco Mosaic Virus Templates for Selective and Controllable Biomineral Deposition. *Beilstein J. Nanotechnol.* **2015**, *6*, 1399–1412.

(91) Aljabali, A. A. A.; Lomonossoff, G. P.; Evans, D. J. CPMV-Polyelectrolyte-Templated Gold Nanoparticles. *Biomacromolecules* **2011**, *12*, 2723–2728.

(92) Shen, L.; Bao, N.; Prevelige, P. E.; Gupta, A. Fabrication of Ordered Nanostructures of Sulfide Nanocrystal Assemblies over Self-Assembled Genetically Engineered P22 Coat Protein. *J. Am. Chem. Soc.* **2010**, *132*, 17354–17357.

(93) Zandi, R.; Reguera, D.; Bruinsma, R. F.; Gelbart, W. M.; Rudnick, J. Origin of Icosahedral Symmetry in Viruses. *Proc. Natl. Acad. Sci.* **2004**, *101*, 15556–15560.

(94) Lim, T. S. *Recombinant Antibodies for Infectious Diseases*; 2017; Vol. 1053.

(95) Weng, L.; Zhang, H.; Govorov, A. O.; Ouyang, M. Hierarchical Synthesis of Non-Centrosymmetric Hybrid Nanostructures and Enabled Plasmon-Driven Photocatalysis. *Nat. Commun.* **2014**, *5*, 1–10.

(96) Manning, M.; Griffith, J. Association of M13 I-Forms and Spheroids with Lipid Vesicles. *Arch. Biochem. Biophys.* **1985**, *236*, 297–303.

(97) Manning, M.; Moore, M.; Spremulli, L.; Griffith, J. Coat Protein Conformation in M13 Filaments, I-Forms and Spheroids. *Biochem. Biophys. Res. Commun.* **1983**, *112*, 349–355.

(98) Arnold, G. E.; Day, L. a; Dunker, a K. Tryptophan Contributions to the Unusual Circular Dichroism of Fd Bacteriophage. *Biochemistry* **1992**, *31*, 7948–7956.

(99) Berman, H. M.; Westbrook, J.; Feng, Z.; Gilliland, G.; Bhat, T. N.; Weissig, H.; Shindyalov, I. N.; Bourne, P. E. The Protein Data Bank. *Nucleic Acids Res.* **2000**, *28*, 235–242.

(100) Marvin, D. A.; Welsh, L. C.; Symmons, M. F.; Scott, W. R. P.; Straus, S. K. Molecular Structure of Fd (F1, M13) Filamentous Bacteriophage Refined with Respect to X-Ray Fibre Diffraction and Solid-State NMR Data Supports Specific Models of Phage Assembly at the Bacterial Membrane. *J. Mol. Biol.* **2006**, *355*, 294–309.

(101) Pettersen, E. F.; Goddard, T. D.; Huang, C. C.; Couch, G. S.; Greenblatt, D. M.; Meng, E. C.; Ferrin, T. E. UCSF Chimera - A Visualization System for Exploratory Research and Analysis. *J. Comput. Chem.* **2004**, *25*, 1605–1612.

(102) Marassi, F. M.; Opella, S. J. Simultaneous Assignment and Structure Determination of a Membrane Protein from NMR Orientational Restraints. *Protein Sci.* **2003**, *12*, 403–411.

(103) Hoffmann-Thoms, S.; Jakob, R. P.; Schmid, F. X. Energetic Communication between Functional Sites of the Gene-3-Protein during Infection by Phage Fd. *J. Mol. Biol.* **2014**, *426*, 1711–1722.

(104) Bennett, N. J.; Rakonjac, J. Unlocking of the Filamentous Bacteriophage Virion during Infection Is Mediated by the C Domain of PIII. *J. Mol. Biol.* **2006**, *356*, 266–273.

(105) Deng, L. W.; Perham, R. N. Delineating the Site of Interaction on the PIII Protein of Filamentous Bacteriophage Fd with the F-Pilus of Escherichia Coli. *J. Mol. Biol.* **2002**, *319*, 603–614.

(106) Nelson, F. K.; Friedman, S. M.; Smith, G. P. Filamentous Phage DNA Cloning Vectors: A Noninfective Mutant Nonh a Nonpolar Deletion in Gene III. *Virology* **1981**, *108*, 338–350.

(107) Lopez, J.; Webster, R. E. Morphogenesis of Filamentous Bacteriophage F1: Orientation of Extrusion and Production of Polyphage. *Virology* **1983**, *127*, 177–193.

(108) Marvin, D. A. Dynamics of Telescoping Inovirus: A Mechanism for Assembly at Membrane Adhesions. *Int. J. Biol. Macromol.* **1989**, *11*, 159–164.

(109) Stopar, D.; Spruijt, R. B.; Wolfs, C. J. A. M.; Hemminga, M. A. Mimicking Initial Interactions of Bacteriophage M13 Coat Protein Disassembly in Model Membrane Systems. *Biochemistry* **1998**, *37*, 10181–10187.

(110) Slater, K. *Environmental Impact of Textiles*, 4th ed.; Woodhead Publishing, 2003.

(111) Concerns, E. The Environmental, Health and Economic Impacts of Textile Azo Dyes. *House Parliam. Sci. Technol.* **2013**, 1–5.

(112) Harpreet Kaur, G. S. Removal of Dyes from Textile Industry Effluent: A Review. *J. Text. Assoc.* **2015**, No. April, 59–63.

(113) Flatabø, R.; Holm, V. R. A.; Eidsvåg, H.; Holst, B.; Greve, M. M. Light Absorption and Scattering of 40–170 Nm Gold Nanoparticles on Glass Substrates. *J. Vac. Sci. Technol. B, Nanotechnol. Microelectron. Mater. Process. Meas. Phenom.* **2017**, *35*, 06G403.

(114) Linic, S.; Christopher, P.; Ingram, D. B. Plasmonic-Metal Nanostructures for Efficient Conversion of Solar to Chemical Energy. *Nat. Mater.* **2011**, *10*, 911–921.

(115) Ma, X.-C.; Dai, Y.; Yu, L.; Huang, B.-B. Energy Transfer in Plasmonic Photocatalytic Composites. *Light Sci. Appl.* **2016**, *5*, e16017.

(116) Cushing, S. K.; Li, J.; Bright, J.; Yost, B. T.; Zheng, P.; Bristow, A. D.; Wu, N. Controlling Plasmon-Induced Resonance Energy Transfer and Hot Electron Injection Processes in Metal@TiO 2 Core–Shell Nanoparticles. *J. Phys. Chem. C*

2015, *119*, 16239–16244.

(117) Seh, Z. W.; Liu, S.; Low, M.; Zhang, S. Y.; Liu, Z.; Mlayah, A.; Han, M. Y. Janus Au-TiO 2 Photocatalysts with Strong Localization of Plasmonic near-Fields for Efficient Visible-Light Hydrogen Generation. *Adv. Mater.* **2012**, *24*, 2310–2314.

(118) De La Cotte, A.; Wu, C.; Trévisan, M.; Repula, A.; Grelet, E. Rod-Like Virus-Based Multiarm Colloidal Molecules. *ACS Nano* **2017**, *11*, 10616–10622.

(119) Liu, A.; Yang, L.; Verwegen, M.; Reardon, D.; Cornelissen, J. J. L. M. Construction of Core-Shell Hybrid Nanoparticles Templated by Virus-like Particles. *RSC Adv.* **2017**, *7*, 56328–56334.

(120) Balci, S.; Noda, K.; Bittner, A. M.; Kadri, A.; Wege, C.; Jeske, H.; Kern, K. Self-Assembly of Metal-Virus Nanodumbbells. *Angew. Chemie - Int. Ed.* **2007**, *46*, 3149–3151.

(121) Klem, M. T.; Willits, D.; Young, M.; Douglas, T. 2-D Array Formation of Genetically Engineered Viral Cages on Au Surfaces and Imaging by Atomic Force Microscopy. *J. Am. Chem. Soc.* **2003**, *125*, 10806–10807.

(122) Plank, J. M.; Alibay, Z.; Ngo-Duc, T.-T.; Lai, M.; Mayes, E. A. S.; Haberer, E. D. Examination of Bi-Functional M13 Spheroid Formation for Assembly of Asymmetric Au/ZnS Hetero-Nanoparticles. *Submiss.* **2019**.

(123) Bochev, B.; Yordanov, G. Room Temperature Synthesis of Thioglycolate-Coated Zinc Sulfide (ZnS) Nanoparticles in Aqueous Medium and Their Physicochemical Characterization. *Colloids Surfaces A Physicochem. Eng. Asp.* **2014**, *441*, 84–90.

(124) Baishya, U.; Sarkar, D. ZnS Nanocomposite Formation: Effect of ZnS Source Concentration Ratio. *Indian J. Pure Appl. Phys.* **2011**, *49*, 186–189.

(125) Zhou, Z.; Bedwell, G. J.; Li, R.; Palchoudhury, S.; Prevelige, P. E.; Gupta, A. Pathways for Gold Nucleation and Growth over Protein Cages. *Langmuir* **2017**, *33*, 1–25.

(126) Schneider, C. A.; Rasband, W. S.; Eliceiri, K. W. NIH Image to ImageJ: 25 Years of Image Analysis. *Nat. Methods* **2012**, *9*, 671–675.

(127) Mills, A.; Hill, C.; Robertson, P. K. J. Overview of the Current ISO Tests for Photocatalytic Materials. *J. Photochem. Photobiol. A Chem.* **2012**, *237*, 7–23.

(128) Saeed, N. M. Structural and Optical Properties of ZnS Thin Films Prepared by Spray Pyrolysis Technique. *J. Al-Nahrain Univ.* **2011**, *14*, 86–92.

(129) Tian, Y.; Wang, L.; Yu, S.; Zhou, W. Heterostructure of Au Nanocluster Tipping on a ZnS Quantum Rod: Controlled Synthesis and Novel Luminescence. *Nanotechnology* **2015**, *26*, 325702.

(130) Brus, L. Electronic Wave Functions in Semiconductor Clusters: Experiment and

Theory. *J. Phys. Chem.* **1986**, *90*, 2555–2560.

(131) Prevo, B. G.; Esakoff, S. A.; Mikhailovsky, A.; Zasadzinski, J. A. Scalable Routes to Gold Nanoshells with Tunable Sizes and Response to Near-Infrared Pulsed-Laser Irradiation. *Small* **2008**, *4*, 1183–1195.

(132) Abdollahi, S. N.; Naderi, M.; Amoabediny, G. Synthesis and Characterization of Hollow Gold Nanoparticles Using Silica Spheres as Templates. *Colloids Surfaces A Physicochem. Eng. Asp.* **2013**, *436*, 1069–1075.

(133) Abdelhalim, M. A. K.; M. Mady, M. Physical Properties of Different Gold Nanoparticles: Ultraviolet-Visible and Fluorescence Measurements. *J. Nanomed. Nanotechnol.* **2012**, *03*.

(134) Xu, J. X.; Siriwardana, K.; Zhou, Y.; Zou, S.; Zhang, D. Quantification of Gold Nanoparticle Ultraviolet-Visible Extinction, Absorption, and Scattering Cross-Section Spectra and Scattering Depolarization Spectra: The Effects of Nanoparticle Geometry, Solvent Composition, Ligand Functionalization, and Nanopartic. *Anal. Chem.* **2018**, *90*, 785–793.

(135) Das, K.; Uppal, A.; Saini, R. K.; Varshney, G. K.; Mondal, P.; Gupta, P. K. Hyper-Rayleigh Scattering from Gold Nanoparticles: Effect of Size and Shape. *Spectrochim. Acta - Part A Mol. Biomol. Spectrosc.* **2014**, *128*, 398–402.

(136) Vieaud, J.; Gao, J.; Cane, J.; Stchakovsky, M.; En Naciri, A.; Ariga, K.; Oda, R.; Pouget, E.; Battie, Y. Gold Nanoparticle Chains: Synthesis, Characterization, and Modeling Using Spectroscopic Ellipsometry. *J. Phys. Chem. C* **2018**, *122*, 11973–11984.

(137) Denzler, D.; Olschewski, M.; Sattler, K. Luminescence Studies of Localized Gap States in Colloidal ZnS Nanocrystals. *J. Appl. Phys.* **1998**, *84*, 2841–2845.

(138) Liang, Y.-C.; Liu, S.-L. Synthesis and Enhanced Humidity Detection Response of Nanoscale Au-Particle-Decorated ZnS Spheres. *Nanoscale Res. Lett.* **2014**, *9*, 647.

(139) Geng, J.; Song, G. One-Pot Fast Synthesis of Spherical ZnS/Au Nanocomposites and Their Optical Properties. *J. Mater. Sci.* **2013**, *48*, 636–643.

(140) Chen, Y. C.; Pu, Y. C.; Hsu, Y. J. Interfacial Charge Carrier Dynamics of the Three-Component In 2O 3-TiO 2-Pt Heterojunction System. *J. Phys. Chem. C* **2012**, *116*, 2967–2975.

(141) Xu, Z.; Zhuang, C.; Zou, Z.; Wang, J.; Xu, X.; Peng, T. Enhanced Photocatalytic Activity by the Construction of a TiO2/Carbon Nitride Nanosheets Heterostructure with High Surface Area via Direct Interfacial Assembly. *Nano Res.* **2017**, *10*, 2193–2209.

(142) Zhou, Z.; Bedwell, G. J.; Li, R.; Bao, N.; Prevelige, P. E.; Gupta, A. P22 Virus-like Particles Constructed Au/CdS Plasmonic Photocatalytic Nanostructures for

Enhanced Photoactivity. *Chem. Commun. (Camb).* **2015**, *51*, 1062–1065.

(143) Tian, B.; Lei, Q.; Zhang, W.; Cui, Y.; Tian, Y.; Tian, B. UV-Driven Overall Water Splitting Using Unsupported Gold Nanoparticles as Photocatalysts. *Chem. Commun.* **2018**, *54*, 1845–1848.

(144) Clavero, C. Plasmon-Induced Hot-Electron Generation at Nanoparticle/Metal-Oxide Interfaces for Photovoltaic and Photocatalytic Devices. *Nat. Photonics* **2014**, *8*, 95–103.

(145) Chiarello, G. L.; Aguirre, M. H.; Selli, E. Hydrogen Production by Photocatalytic Steam Reforming of Methanol on Noble Metal-Modified TiO2. *J. Catal.* **2010**, *273*, 182–190.

(146) Ruiz Peralta, M. D. L.; Pal, U.; Zeferino, R. S. Photoluminescence (PL) Quenching and Enhanced Photocatalytic Activity of Au-Decorated ZnO Nanorods Fabricated through Microwave-Assisted Chemical Synthesis. *ACS Appl. Mater. Interfaces* **2012**, *4*, 4807–4816.

(147) Wu, K.; Zhu, H.; Liu, Z.; Rodríguez-Córdoba, W.; Lian, T. Ultrafast Charge Separation and Long-Lived Charge Separated State in Photocatalytic CdS–Pt Nanorod Heterostructures. *J. Am. Chem. Soc.* **2012**, *134*, 10337–10340.

(148) Dey, A.; Middya, S.; Jana, R.; Das, M.; Datta, J.; Layek, A.; Ray, P. P. Light Induced Charge Transport Property Analysis of Nanostructured ZnS Based Schottky Diode. *J. Mater. Sci. Mater. Electron.* **2016**, *27*, 6325–6335.

(149) Yu, Y.; Jie, J.; Jiang, P.; Wang, L.; Wu, C.; Peng, Q.; Zhang, X.; Wang, Z.; Xie, C.; Wu, D.; et al. High-Gain Visible-Blind UV Photodetectors Based on Chlorine-Doped n-Type ZnS Nanoribbons with Tunable Optoelectronic Properties. *J. Mater. Chem.* **2011**, *21*, 12632–12638.

(150) Sze, S. M. *Physics of Semiconductor Devices*; John Wiley & Sons Inc.: Hoboken, NJ, 1981.

(151) Sundararaman, R.; Narang, P.; Jermyn, A. S.; Goddard III, W. a.; Atwater, H. a. Theoretical Predictions for Hot-Carrier Generation from Surface Plasmon Decay. *Nat. Commun.* **2014**, *5*, 5788.

(152) Jain, R.; Sikarwar, S. Photodestruction and COD Removal of Toxic Dye Erioglaucine by TiO(2)-UV Process: Influence of Operational Parameters. *Int. J. Phys. Sci.* **2008**, *3*, 299–305.

(153) Madkour, M.; Al Sagheer, F. Au/ZnS and Ag/ZnS Nanoheterostructures as Regenerated Nanophotocatalysts for Photocatalytic Degradation of Organic Dyes. *Opt. Mater. Express* **2017**, *7*, 158.

(154) Hong, L.; Jiang, S.; Granick, S. Simple Method to Produce Janus Colloidal Particles in Large Quantity. *Langmuir* **2006**, *22*, 9495–9499.

(155) Wang, C.; Xu, C.; Zeng, H.; Sun, S. Recent Progress in Syntheses and Applications of Dumbbell-like Nanoparticles. *Adv. Mater.* **2009**, *21*, 3045–3052.

(156) Chiu, C. Y.; Li, Y.; Huang, Y. Size-Controlled Synthesis of Pd Nanocrystals Using a Specific Multifunctional Peptide. *Nanoscale* **2010**, *2*, 927–930.

(157) Zaman, M. S.; Moon, C. H.; Bozhilov, K. N.; Haberer, E. D. Phage-Directed Synthesis of Copper Sulfide: Structural and Optical Characterization. *Nanotechnology* **2013**, *24*.

(158) Zhang, G.; Wei, S.; Belcher, A. M. Biotemplated Zinc Sulfide Nanofibers as Anode Materials for Sodium-Ion Batteries. *ACS Appl. Nano Mater.* **2018**, *1*, 5631–5639.

(159) Montalvan-Sorrosa, D.; González-Solis, J. L.; Mas-Oliva, J.; Castillo, R. Filamentous Virus Decoration with Gold Nanoparticles: Global Fingerprints of Bionanocomposites Acquired with SERS. *RSC Adv.* **2014**, *4*, 57329–57336.

(160) Tauc, J. *Amorphous and Liquid Semiconductors*; University, B., Ed.; Springer, 1974.

(161) Porterfield, J. Z.; Zlotnick, A. A Simple and General Method for Determining the Protein and Nucleic Acid Content of Viruses by UV Absorbance. *Virology* **2010**, *407*, 281–288.

(162) Dunker, A. K.; Ensign, L. D.; Arnold, G. E.; Roberts, L. M. Proposed Molten Globule Intermediates in Fd Phage Penetration and Assembly. **1991**, *292*, 275–278.

(163) Plank, J. M.; Ngo-Duc, T.-T.; Alibay, Z.; Haberer, E. D. Photocatalytic Nanostructures of Au/ZnS Assembled on M13 Spheroids. *Prep.* **2019**.

(164) Liu, Y.; Gu, Y.; Yan, X.; Kang, Z.; Lu, S.; Sun, Y.; Zhang, Y. Design of Sandwich-Structured ZnO/ZnS/Au Photoanode for Enhanced Efficiency of Photoelectrochemical Water Splitting. *Nano Res.* **2015**, *8*, 2891–2900.

(165) Løset, G. Å.; Sandlie, I. Next Generation Phage Display by Use of PVII and PIX as Display Scaffolds. *Methods* **2012**, *58*, 40–46.

(166) Løset, G. Å.; Bogen, B.; Sandlie, I. Expanding the Versatility of Phage Display I: Efficient Display of Peptide-Tags on Protein VII of the Filamentous Phage. *PLoS One* **2011**, *6*, 1–7.

(167) Xu, X.; Hu, L.; Gao, N.; Liu, S.; Wageh, S.; Al-Ghamdi, A. A.; Alshahrie, A.; Fang, X. Controlled Growth from ZnS Nanoparticles to ZnS-CdS Nanoparticle Hybrids with Enhanced Photoactivity. *Adv. Funct. Mater.* **2015**, *25*, 445–454.

(168) Wang, Z.; Cao, S. W.; Loo, S. C. J.; Xue, C. Nanoparticle Heterojunctions in ZnS-ZnO Hybrid Nanowires for Visible-Light-Driven Photocatalytic Hydrogen

Generation. *CrystEngComm* **2013**, *15*, 5688–5693.

(169) Kwon, K. W.; Shim, M. γ-Fe2O3/II-VI Sulfide Nanocrystal Heterojunctions. *J. Am. Chem. Soc.* **2005**, *127*, 10269–10275.

(170) Dong, P.; Lin, Y.; Deng, J.; Di, J. Ultrathin Gold-Shell Coated Silver Nanoparticles onto a Glass Platform for Improvement of Plasmonic Sensors. *ACS Appl. Mater. Interfaces* **2013**, *5*, 2392–2399.

(171) Pouretedal, H. R.; Norozi, A.; Keshavarz, M. H.; Semnani, A. Nanoparticles of Zinc Sulfide Doped with Manganese, Nickel and Copper as Nanophotocatalyst in the Degradation of Organic Dyes. *J. Hazard. Mater.* **2009**, *162*, 674–681.

(172) Eyasu, A.; Yadav, O. P.; Bachheti, R. K. Photocatalytic Degradation of Methyl Orange Dye Using Cr-Doped ZnS Nanoparticles under Visible Radiation. *Int. J. ChemTech Res.* **2013**, *5*, 1452–1461.

(173) Rabbani, S. F.; Banu, I. B. S. Half Metallic Ferromagnetism in (Mn,Cr) Codoped ZnS Dilute Magnetic Semiconductor: First Principles Calculations. *Comput. Mater. Sci.* **2015**, *101*, 281–286.

(174) Ai, M.; Lang, L.; Li, B.; Xu, Z. Mesoporous AlPO4: A Highly Efficient Heterogeneous Catalyst for Synthesis of 5-Substituted 1H-Tetrazoles from Nitriles and Sodium Azide via [3 + 2] Cycloaddition. *Chem. Lett.* **2012**, *41*, 814–816.

(175) Karunakaran, C.; Vinayagamoorthy, P.; Jayabharathi, J. Nonquenching of Charge Carriers by Fe3O4 Core in Fe3O4/ZnO Nanosheet Photocatalyst. *Langmuir* **2014**, *30*, 15031–15039.

(176) Chang, C. J.; Lee, Z.; Wei, M. D.; Chang, C. C.; Chu, K. W. Photocatalytic Hydrogen Production by Magnetically Separable Fe3O4@ZnS and NiCo2O4@ZnS Core-Shell Nanoparticles. *Int. J. Hydrogen Energy* **2015**, *40*, 11436–11443.